THE IMPROVEMENT OF THE WEAR PERFORMANCE OF THE TI-64 ALLOY USING THE OXYGEN BOOST DIFFUSION TREATMENT

Centre for Materials Engineering

MASTERS DISSERTATION

STUDENT: RYAN WILLIAMS
SUPERVISOR: PROF. R. KNUTSEN
22 November 2010

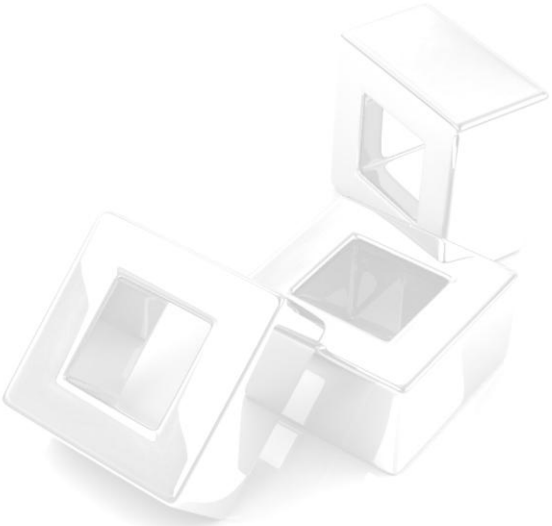

ACKNOWLEDGEMENTS

On behalf of the Centre for Materials Engineering we would like to express our utmost gratitude for the financial support provided by the Department of Science and Technology through the Advanced Manufacturing Technology Strategy (AMTS).

I would like to thank the following people for their continued assistance and support throughout the process of compiling this work:

- Prof. Robert Knutsen for his continued mentoring and invaluable insight throughout the duration of the project. Without his leadership the work would not have reached this standard,
- Prof. Candice Lang for always having a friendly smile and open door, always happy to share her years of experience in the field of materials engineering,
- To my close friends here at the Centre for Materials Engineering for making the long hours seem short and for the constant laughter,
- Beverly Glass for always being the first to provide a friendly welcome and for ensuring the administration was always in check,
- To Penny Park Ross for ensuring that laboratory chemicals and equipment were always available,
- To Glen Newins and the workshop staff for always having time to machine my samples,
- Miranda Waldron for making the SEM visits enjoyable,
- To the cleaning staff who were always happy to ensure that the work space was clean and tidy.

I would like to thank my family for always guiding me through those hard situations and for providing life lessons which helped me reach this point. Without them the opportunity for completing my MSc would not have been possible. A special thank you goes to a very close friend of mine, Lauren Lewis, who went beyond what was expected of her to assist me and always provided encouragement and support whenever was necessary.

Finally I would like to give thanks to God, for giving me the strength, mindset and drive which moulded me into the individual I am today.

ABSTRACT

Oxygen Boost Diffusion Hardening (OBDH) is a cost effective surface modification process which can greatly improve the tribological properties of titanium components. This report deals with the oxygen diffusion treatment of Ti-6Al-4V (Ti-64), the most commonly used titanium alloy, to rank various treatment conditions based on their ability to increase the surface hardness and wear resistance. Modes of wear were evaluated using SEM micrographs and elemental analysis of worn surfaces and wear debris.

The linear reciprocating ball-on-flat arrangement was used, with the Ti-64 samples as the counter-face and the ball composed of AISI52100 steel. A load of 5.0N and a sliding speed of 0.05m.s^{-1} was used for the various distances tested. Distances from 100m to 2400m were used to plot the progressive volume loss for the treated and untreated samples. Frictional analysis was performed on the 2400m tests.

The work has shown that this specific OBDH method is successful in forming a hardened case of stabilised α-phase Ti up to a depth of 450μm with a decreasing hardness profile to this depth. When compared to the untreated samples, the OBDH samples showed improved wear resistance in the form of lower volume losses. The current work has also shown that this improvement in the wear resistance is directly affected by the distance into the hardness profile where the tests were performed. OBDH samples tested at two separate depths into the profile showed varied wear mechanisms and volume losses.

Separate treatments involved oxidation of Ti-64 samples in an air environment at 850℃ and 600℃ for 30 minutes and 20 hours respectively. When compared to the untreated and OBDH samples, all oxide samples showed a much lower degree of volume loss with the samples oxidised at 850℃ showing an increase in surface hardness from the untreated state of 347Hv to 1004Hv.

Frictional analysis was ineffective in providing a means of distinguishing between treatment methods which produced varied improvements in the wear resistance.

The greatest improvement in the wear resistance from the untreated state was noted for the samples which were oxidised at 600℃ and subsequently polished to a metallic finish. These samples showed no measurable volume loss coupled with a low degree of volume loss for the steel balls.

TABLE OF CONTENTS

4 LITERATURE REVIEW:

List of Figures

List of Tables

1 INTRODUCTION

1.1 The tribological problem

Titanium and its alloys exhibit excellent properties including corrosion resistance, high temperature strength, high specific strength and excellent biocompatibility. The element itself is not in short supply and is the 9th most abundant element worldwide constituting approximately 0.4% of the earth's crust (Donachie ed. 1988). However two main problems exist with the usage of titanium. Firstly, it is an expensive process to extract the element from its mineral forms and it is currently three times more expensive to produce titanium than steel in equivalent quantities. Secondly titanium and its alloys perform poorly in tribological environments. This has been a serious limiting factor in the usage of titanium in certain applications (Moiseyev 2006). This property has been attributed to three main reasons, namely its electron configuration, crystal structure and the ineffective usage of lubrication in these environments. The first reason pertains to the d-bond character of titanium being the lowest possible value for an element and thus rendering it highly chemically reactive leading to large degrees of adhesive wear and material transfer occurring in tribological environments. Secondly the c/a ratio of the hexagonally closed packed alpha phase of titanium does not allow for close packing and this increases the number of slip planes. Finally, it has been experimentally shown that the standard oils and greases used during steel lubrication are ineffective for titanium wear systems. This is largely due to the fact that the heat conductive ability of titanium is lower than that of steels, causing high temperatures to exist at the contact areas during sliding, leading to a drop in the material strength and increasing the degree of material transfer. Many surface modification techniques have been employed to improve titanium's wear performance (Donachie ed. 1988). A fairly new, novel and inexpensive method being investigated is that of oxygen boost diffusion.

1.2 Oxygen boost diffusion

The method of oxygen boost diffusion hardening (OBDH) is effectively a two step process. The first step involves the formation of a thick adherent oxide layer on the surface of the titanium specimen which will serve as an oxygen reservoir for the second step. The oxidation step is carried out in an oxygen rich environment at elevated temperatures in the range of 550-900ºC (Dong and Li 2000b).

The second step involves diffusion of oxygen into the underlying titanium substrate to cause solid solution strengthening of the material. This forms a hardened case of the alpha phase of titanium just below the surface as oxygen is an alpha phase stabiliser. The diffusion layer greatly improves the surface hardness of the specimen and has been shown to increase its wear resistance (Dong and Li 2000b).

The scope of the research is to investigate the improvement of the wear performance of the alloy Ti-6Al-4V subjected to various oxygen boost hardening treatments and to categorise the wear mechanisms that occur. The research will assist in verifying the effectiveness of this treatment process for increasing the usage of titanium in tribological systems.

More specifically the following questions are addressed in this research:

1. Will the OBDH method produce a hardened case below the surface of the Ti-64 sample and will this layer improve the wear resistance of the sample?
2. If the OBDH method is successful in improving the wear resistance of the Ti-64 samples, will the wear performance be directly related to the hardness profile?
3. Can friction coefficient and profilometry analysis be used to characterize the wear performance of the different treatments?

2 LITERATURE REVIEW: TITANIUM STRUCTURE AND PROPERTIES

2.1.1 Titanium history

Titanium was first found in its raw state as ilmenite, $FeTiO_3$, in 1791 and was named after the mythological Titans because of its great strength and "stubbornness". The latter trait attributed to the fact that titanium is highly reactive. It forms stable carbides and when heated readily reacts with oxygen and nitrogen. For early metallurgists this posed a great problem and it wasn't until 1825 that the first highly impure form of titanium was produced. A century later the metallurgist Dr. William Justin Kroll had finally perfected his process of the reduction of rutile, TiO_2, into the highly porous solid known as titanium sponge. The extraction method was named the Kroll's process and it has been used to date as the primary means with which to produce titanium (Housley 2007).
Although early uses of titanium peaked at being an additive to white paint in its oxide form, its uses in many sectors today can be solely attributed to its excellent properties. Its low density and high strength give it one of the highest strength to weight ratios of the structural materials and for this main reason it has become a benchmark in the aerospace industry. Its tendency to produce a natural corrosion resistant oxide layer in the presence of oxygen and the fact that it is non-magnetic and biocompatible make it an excellent material for medical implants. The oxide layer is highly erosion resistant and titanium itself has a high thermal conductivity which surpasses that of stainless steel, thereby making it invaluable in the engineering of piping and heat exchangers. With its low modulus of elasticity it possesses excellent spring back characteristics and consequently the production of springs from titanium are half the size and weight of a steel spring but with the same strength. Titanium's low coefficient of thermal expansion allows it to be incorporated in a wide variety of composite materials where heating is a key factor in the application, which is especially important for metal/ceramic composites. It provides aesthetic applications because of the way the oxide manipulates light and by varying its surface texture titanium has seen applications in architecture and jewellery products. Finally, because titanium itself is the ninth most abundant element on earth and its production generates no harmful by-products with 95% of the scrap produced being able to be recycled, titanium is extremely environmentally friendly (International Titanium Association 2007a).

One alloy has become the workhorse of the titanium industry and is responsible for as much as 45% of titanium applications. This alloy is Ti-6Al-4V and it has become the standard against which other titanium alloys are compared to when a selection for an application must be made (Boyer ed. 1998). Although there is a large diversity for which titanium and its alloys are used, the largest demand comes from aerospace applications. It is estimated that approximately 42% of the titanium demand in the US is for aircraft engine components alone excluding airframe usage; the figure is 37% in Europe (International Titanium Association 2007b). A pinnacle of titanium performance is the SR-71 Blackbird (Figure 1) of which more than 90% of the aircraft was made from titanium. With this much titanium in the structure of the craft, it broke altitude and speed records which have not been surpassed to date.

Figure 1: SR-71 Blackbird
(http://www.nasa.gov/centers/dryden/multimedia/imagegallery/SR-71/index.html).

2.1.2 Metallurgy of Titanium

Titanium can occur in two crystal structures, namely a hexagonally close packed (h.c.p.) α-phase and a body centred cubic (b.c.c.) β-phase, illustrated in Figure 2. The β-phase is not stable at room temperature unless alloying elements have been added to stabilise it. Commercially pure titanium (CP-Ti) consists of an α-phase microstructure and strength between CP-Ti grades greatly depends on the amount of interstitial elements present i.e. oxygen and nitrogen. A distortion of the h.c.p. lattice results from the solid solution elements and this distortion obstructs dislocation motion and thus increases the strength (Donachie ed. 1988). At about 882℃ the α-phase undergoes a phase transformation to the β-phase and this temperature is known as the “beta transus temperature” (Leyens & Peters 2003). The three main classes that exist for the classification of the alloys based on the phases present in the microstructure are alpha, alpha/beta and beta alloys. The various classes depend on the amount of phase stabilises used to obtain the microstructures required and each class has its benefits and disadvantages (Donachie ed. 1988). Table 1 shows the effect that various elements have on the phases formed (Moiseyev 2006).

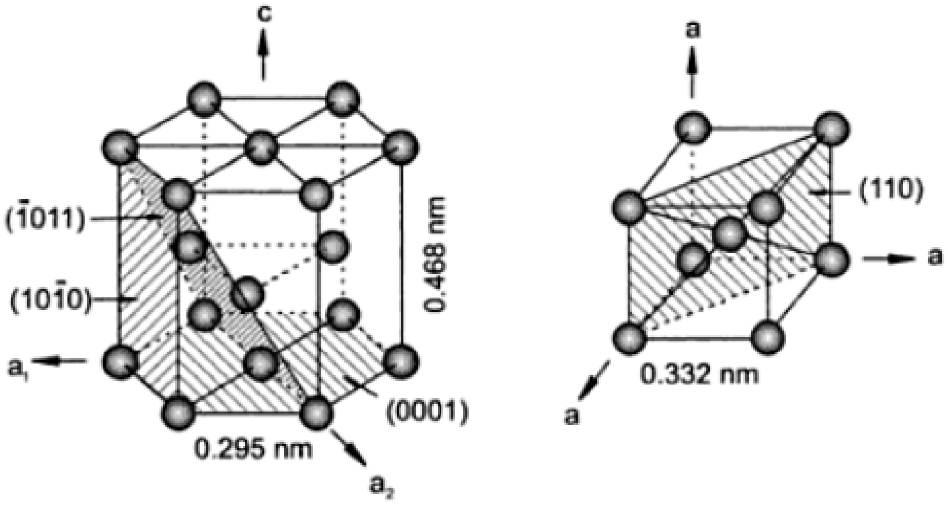

Figure 2: Crystal structures of h.c.p. α-phase (Left) and b.c.c. β-phase (right) (Leyens & Peters 2003).

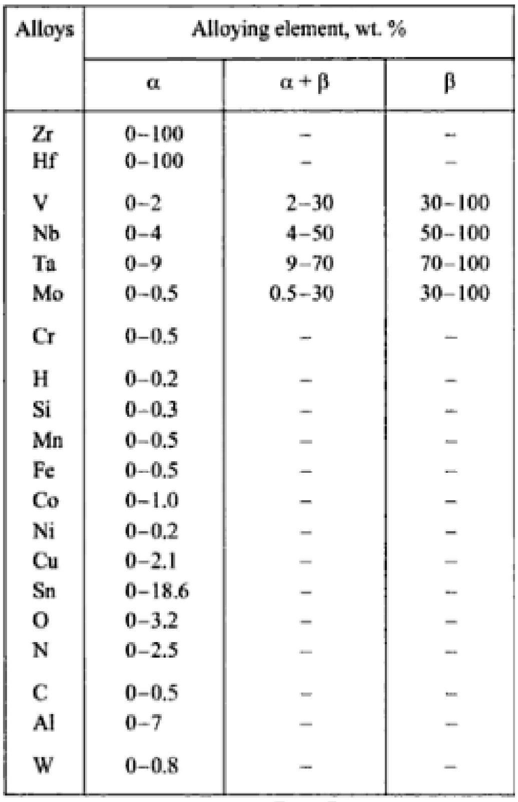

Alloys	Alloying element, wt. %		
	α	α + β	β
Zr	0–100	–	–
Hf	0–100	–	–
V	0–2	2–30	30–100
Nb	0–4	4–50	50–100
Ta	0–9	9–70	70–100
Mo	0–0.5	0.5–30	30–100
Cr	0–0.5	–	–
H	0–0.2	–	–
Si	0–0.3	–	–
Mn	0–0.5	–	–
Fe	0–0.5	–	–
Co	0–1.0	–	–
Ni	0–0.2	–	–
Cu	0–2.1	–	–
Sn	0–18.6	–	–
O	0–3.2	–	–
N	0–2.5	–	–
C	0–0.5	–	–
Al	0–7	–	–
W	0–0.8	–	–

Table 1: Regions of existence of solid-solution phases in various titanium alloys (Moiseyev 2006).

When compared to the beta phase, the alpha phase is more densely packed and as a result exhibits a range of properties which differ from the b.c.c. β-phase. These include a higher resistance to plastic deformation and creep; the diffusion rate is two orders of magnitude lower than that of the β-phase and it exhibits lower ductility. The resistance to creep is due to the lower diffusivity of elements in the h.c.p. lattice as well as the resistance of this crystal arrangement to dislocation movement. As the number of slip planes within the crystal lattice is an indication of the ease with which dislocations can pass through it, an increase in slip planes would consequently mean an increase in the ease of deformation of the lattice. Inspecting slip planes of the h.c.p. lattice it is observed that only 3 slip planes exist, four times less than the 12 possible slip planes in the b.c.c. configuration. This crystal characteristic is the basis for which limited plastic formability exists in the α-alloys. Phase stabilising elements are classified into their respective groups due to the effect that they cause on the β–transus temperature (Leyens & Peters 2003). Three groups exist namely neutral, alpha-stabilisers and beta stabilisers. Beta stabilising elements can be further divided into isomorphous and eutectoid groups, depending on the elements miscibility within the β-phase. The first group are the miscible elements while the latter form eutectoid systems with titanium (Donachie ed. 1988); this is illustrated in Figure 3 (Leyens & Peters 2003).

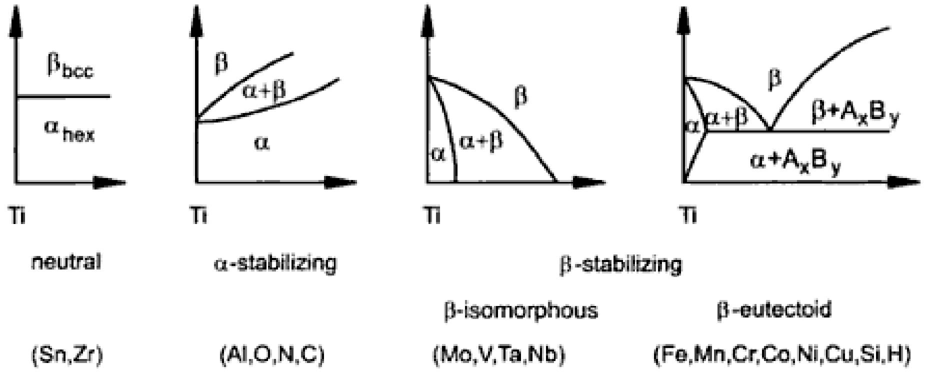

Figure 3: Influence of alloying elements on the phase diagrams of Ti-alloys (Leyens & Peters 2003).

The effect of Al composition within a titanium alloy has been of great importance when producing titanium alloys for specific applications because of the drastic effect that Al has on the microstructure and characteristics of the alloy. Of particular interest is the titanium-aluminium phase diagram Figure 4. Various inter-metallic phases exist that are of increasing importance in industry and these include α_2-Ti_3Al and γ-TiAl. $TiAl_2$ and $TiAl_3$ are extremely brittle and have limited industrial usage (Leyens & Peters 2003).
The inter-metallic γ-TiAl has a high Al content and accordingly has a low density ($3.8 g.cm^{-3}$) however both γ-TiAl and α_2-Ti_3Al have limited ductility and as a result usage of single phase alloys of α_2-Ti_3Al and γ-TiAl have been restricted to non-structural applications. Investigation into two phase α_2 / γ alloys has shown great promise with improved properties (Winkler 2000).

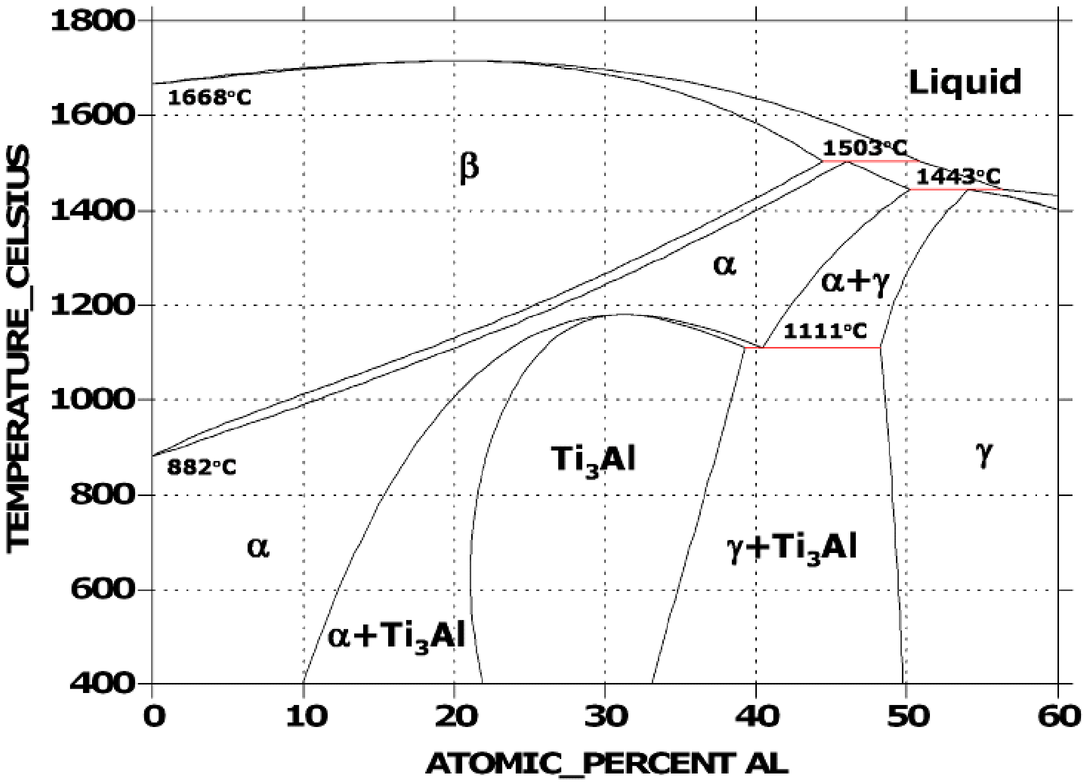

Figure 4: Titanium-Aluminium Binary Phase Diagram (http://www.calphad.com/titanium-aluminum.html).

2.1.3 Classes of Titanium

2.1.3.1 Pure Ti

As discussed earlier, unalloyed Ti grades vary according to the level of impurity interstitial elements of oxygen and nitrogen. The higher the purity of the alloy the lower the strength because of the solid solution strengthening effect of oxygen and nitrogen. At elevated temperatures titanium not only reacts with oxygen to form the protective rutile layer but there is also an inward diffusion of oxygen into the titanium specimen to form a hardened zone of stabilised α-phase. This layer is removed before the specimen is put into service as the hardened surface layer lowers fatigue resistance and ductility. Unalloyed Ti is used for applications that require excellent corrosion resistance where strength is not a critical factor during operation (Donachie ed. 1988).

2.1.3.2 Alpha and Near Alpha Alloys

As a lower diffusion rate exists for the h.c.p. alpha phase, excellent creep and corrosion resistance is observed for these alloys. Generally alpha alloys are lower in density than beta alloys because of the fact that aluminium is the most important alpha stabiliser and has a density half that of titanium (Leyens & Peters 2003). Alpha alloys tend to exhibit better performance related to creep resistance than the other classes but these alloys cannot be strengthened with heat treatments. A benefit of this latter characteristic is that alpha alloys have excellent weldability (Donachie ed. 1988). Another important characteristic of alpha alloys is that they generally have very poor forgeability which arises as stress induced surface cracks and porosity and as a result frequent reheating must be performed during forging of the material (Boyer ed. 1998). When small quantities of beta stabilisers are added and β-phase is retained within the microstructure these alloys are known as near alpha alloys because the microstructure is predominately alpha in nature and their characteristics resemble that of the alpha alloys (Donachie ed. 1988).

2.1.3.3 Alpha-Beta Alloys

These alloys consist of alpha and beta stabilisers and retain more beta phase than the near alpha alloys. Alpha-beta alloys have the ability to be strengthened by heat treatments e.g. solution treatment and aging, and increases in strength of 30 to 50% can be achieved. The most popular titanium alloy used is in fact an alpha-beta alloy, designated Ti-6Al-4V because of its composition i.e. 6wt%Al and 4wt%V where Al and V are strong alpha and beta stabilisers respectively (Donachie ed. 1988).

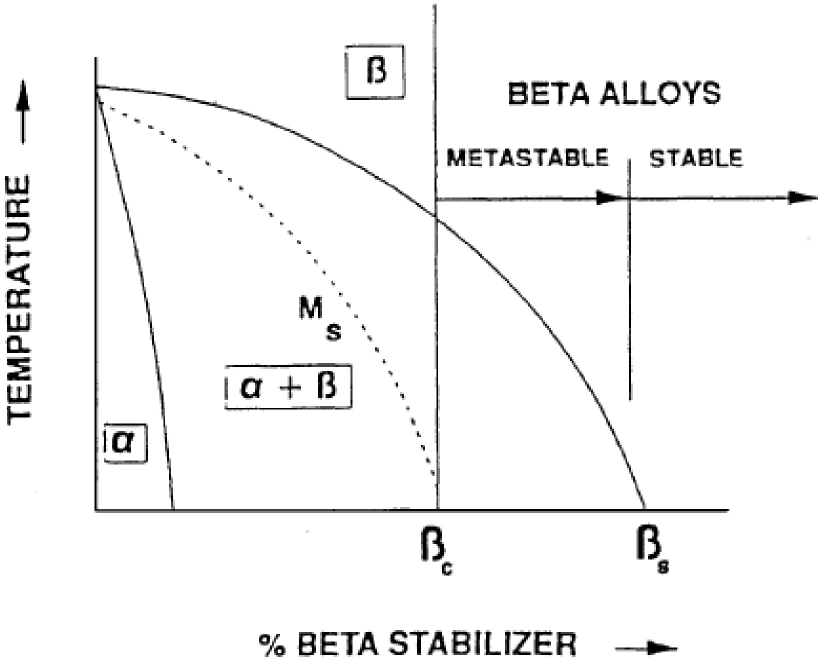

Figure 5: Pseudo-binary phase diagram of Ti-β stabiliser (Long & Rack 1998).

2.1.3.4 Stable and Metastable Beta Alloys

Beta alloys are classified as such when the composition of the alloy contains considerable amount of beta stabilisers such that the room temperature microstructure contains 100% β-phase. This amount of stabiliser can be classified as a critical minimum required to produce this microstructure and is designated as β_c in Figure 5. Stabiliser composition in the range of β_c and β_s will produce alloys that contain metastable β-phase which can precipitate a second phase during aging. Composition of beta stabilisers above a specific β_s value provides stable β-phase even during thermal exposure (Long & Rack 1998). Aging of the beta alloys are typically performed in the range of 450 to 650℃ (Donachie ed. 1988). Beta alloys exhibit much higher specific weights than alpha alloys as well as inferior corrosion resistance and the maintenance of complex microstructures to maintain specific properties. However, due to the manipulation of these microstructures, beta alloys can be hardened to high strengths exceeding 1400Mpa and careful control of the microstructures allows a combination of both high strength and high toughness to be obtained (Leyens & Peters 2003). Although cold work and thermal exposure can cause a partial transformation from β to α, in the solution treated condition β-alloys show excellent properties such as high hardenability and superior forgability (Donachie ed. 1988). A comparison of the various properties of the different classes is shown in Table 2 (Leyens & Peters 2003).

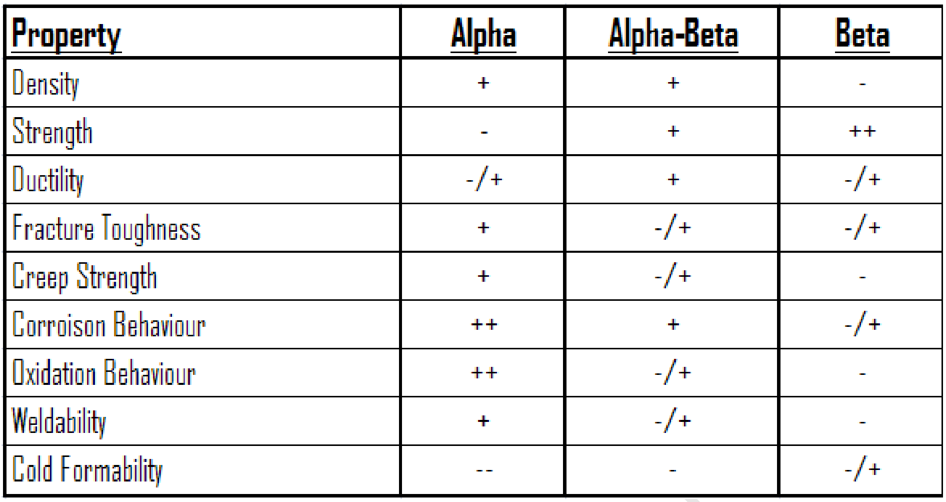

Property	Alpha	Alpha-Beta	Beta
Density	+	+	-
Strength	-	+	++
Ductility	-/+	+	-/+
Fracture Toughness	+	-/+	-/+
Creep Strength	+	-/+	-
Corroison Behaviour	++	+	-/+
Oxidation Behaviour	++	-/+	-
Weldability	+	-/+	-
Cold Formability	--	-	-/+

Table 2: Properties of the various classes of titanium (Leyens & Peters 2003)[1].

2.1.4 *Ti-6Al-4V "The Workhorse" Alloy*

This is the most widely used titanium alloy and contributes to about 45% of the entire titanium industry (Boyer ed. 1998). It exhibits a good combination of strength, corrosion resistance, biocompatibility, high specific strength and good toughness (Brooks 1984), however it performs relatively poorly in tribological systems showing high degrees of wear and unstable friction coefficients (Siva Rama Krishna et al 2007). Some investigations imply that the poor wear resistance is due to the low integrity of the passivating layer formed during high flash temperatures (Molinari et al 1997) as well as high levels of plastic deformation of the surface (Long & Rack 2001), due to the materials low resistance to plastic shearing and low work hardenability (Molinari et al 1997). Mechanical properties of this alloy are controlled by various heat treatments to produce the desired properties, and plastic deformation performed at the various temperatures also plays a role in the evolution of the microstructure (Ding, Guo & Wilson 2001). The evolution of Ti-6Al-4V microstructures from different heat treatments is shown in Figure 6 (Pinke, Caplovic & Kovaks n.d.).

---

[1] Whereby "--" indicates very low, "-" is low, "-+" is average, "+" is high and "++" is very high with regards to the respective titanium classes for a particular property.

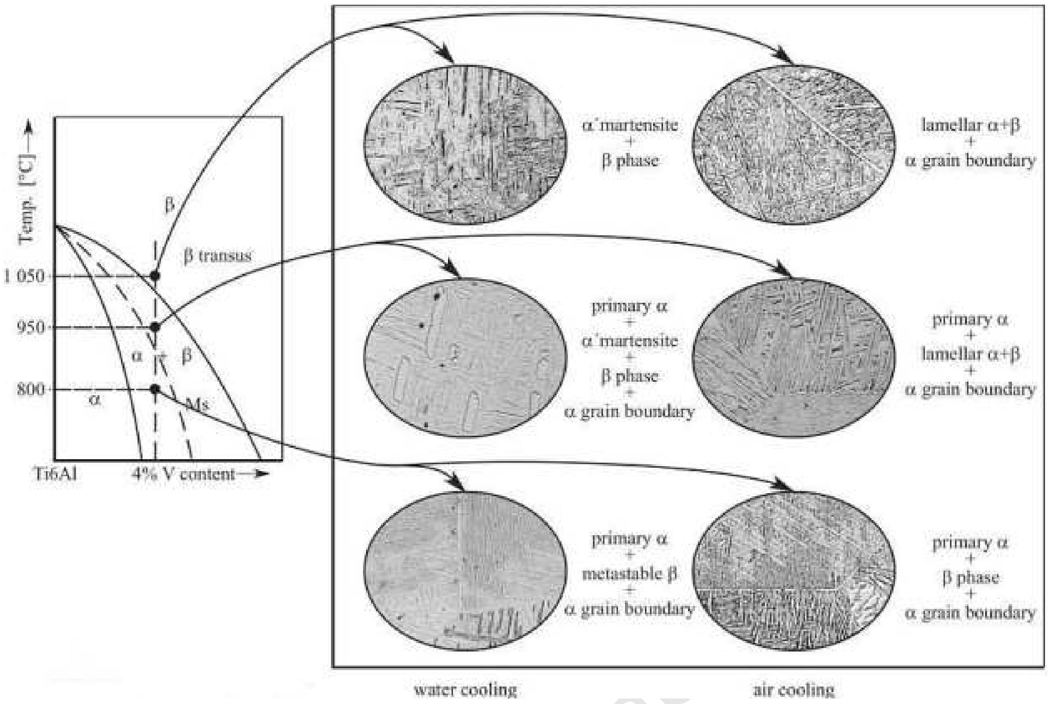

Figure 6: Microstructures developed after solution treatment of Ti-6Al-4 (http://www.kfki.hu/~anyag/Pinke_2.pdf).

In Figure 6, the symbol α' represents the martensitic phase formed from the diffusionless process that occurs upon rapid cooling of the β-phase. The reason that a small percentage of β-exists after the water quench from above the β-transus (seen in Figure 6) is due to the 4%V present in the alloy. This percentage is sufficient to lower the "martensite finish temperature", M_f, below room temperature and thus when the specimen is quenched not all the β-phase transforms (Donachie ed. 1988).

Various heat treatments are performed to obtain certain characteristics; to produce a microstructure that will provide good machinability, a mill anneal is performed; to increase strength of the product, a solution and aging treatment is executed.
Ti-64 is used in a wide range of applications and there is an ever increasing need to replace previously used metals with this alloy. One of the largest areas for use of this material is the aerospace industry (Leyens & Peters 2003). Table 3 shows the comparison between properties of Ti-64 and an austenitic stainless steel used for the same application, namely components of aircraft engines. It is easily seen by this comparison why titanium is such a sought after material. A more recent application for titanium alloys in the aerospace industry is the manufacturing of springs (Figure 7). As certain titanium alloys couple low density with high strength, low modulus and excellent

corrosion resistance springs previously constructed using steel alloys can now be reduced in weight by 70%.

PROPERTIES	**Ti-6Al-4V (Grade 5) Annealed**	**321 Austenitic Stainless steel**
PHYSICAL		
Density (g/cc)	4.43	9.01
MECHANICAL		
Hardness, Vickers (Hv)	349	155
Tensile Strength, Ultimate (MPa)	950	621
Tensile Strength, Yield (MPa)	880	276
Modulus of Elasticity (GPa)	113.8	193
Poissons Ratio	0.342	0.24
THERMAL		
Melting Point (°C)	1604 - 1660	1371 - 1399
Beta Transus (°C)	980	N/A

Table 3: Comparison of properties for Ti-64 and the 321 Stainless steel both of which are used for the construction of engine components in aircraft (http://www.matweb.com/index.aspx).

Figure 7: Illustration of a titanium spring (left) and steel spring (right). The titanium spring is able to carry the same load; although the wire gauge is the same the mass of the titanium spring is 1.45kg while the steel spring weighs 4.35kg (Boyer and Briggs 20005).

3 LITERATURE REVIEW: FRICTION AND WEAR

3.1 Surface topography

When regular machining techniques are used on a specimen to produce a smooth flat appearance the surface itself is never free of irregularities. The irregularities are known as asperities and are essentially areas on the surface that are formed by hills and valleys in the material, with the height from the peak to its valley being its amplitude (Sarkar 1976). Figure 8 below shows a surface which has a degree of micro-roughness with a specific wavelength (Rank Taylor Hobson Limited n.d.).

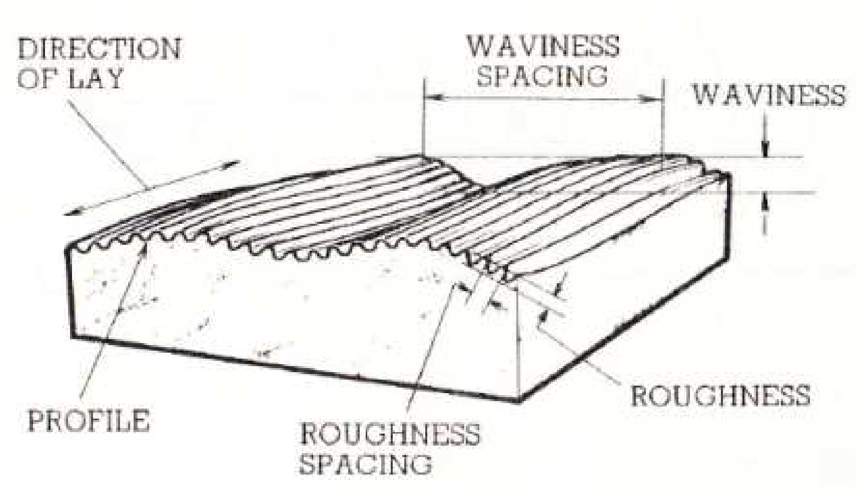

Figure 8: Roughness characteristics of a surface (Rank Taylor Hobson Limited n.d.).

The asperities are large when compared to molecular arrangements of the material; however, the amplitude of these irregularities are considered as micro-roughness. The larger wavelength within the surface composed of many asperities is called waviness or otherwise is known as macro-roughness. The two degrees of roughness combined contribute to the overall roughness of the surface (ed. Halling 1983). This overall roughness being a combination of micro- and macro-roughness is clearly shown in Figure 8 below taken from Williams (1994).

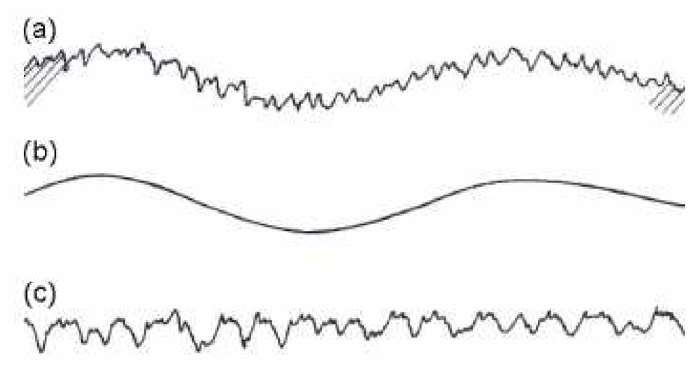

Figure 9: Two degrees of roughness (b) macro-roughness or waviness and (c) micro-roughness, combine to form the overall roughness (a) (Williams 1994).

Various methods of assessing the surface roughness can be employed including optical microscopy, scanning electron microscopy (SEM), optical surface and surface profilometry (Williams 1994). The final process is the least time consuming and most well-known of the methods (ed. Halling 1983). Quantification of roughness is associated with the equation for R_a. R_a, also called C.L.A. (Centre Line Average), is defined as the average deviation of the surface heights from the centre line; the centre line being the line drawn such that the area of the surface above and below the line is constant (Hutchings 1992). This is illustrated in Figure 10 (a) where the centre line is shown as "m" and the actual surface profile has been plotted on a Cartesian plane. Formulas for R_a are given below the curve. A second roughness measurement of importance is the R_y value; this is the distance from the highest peak to the lowest valley within a given sampling length. A representation of this is shown in Figure 10 (b).

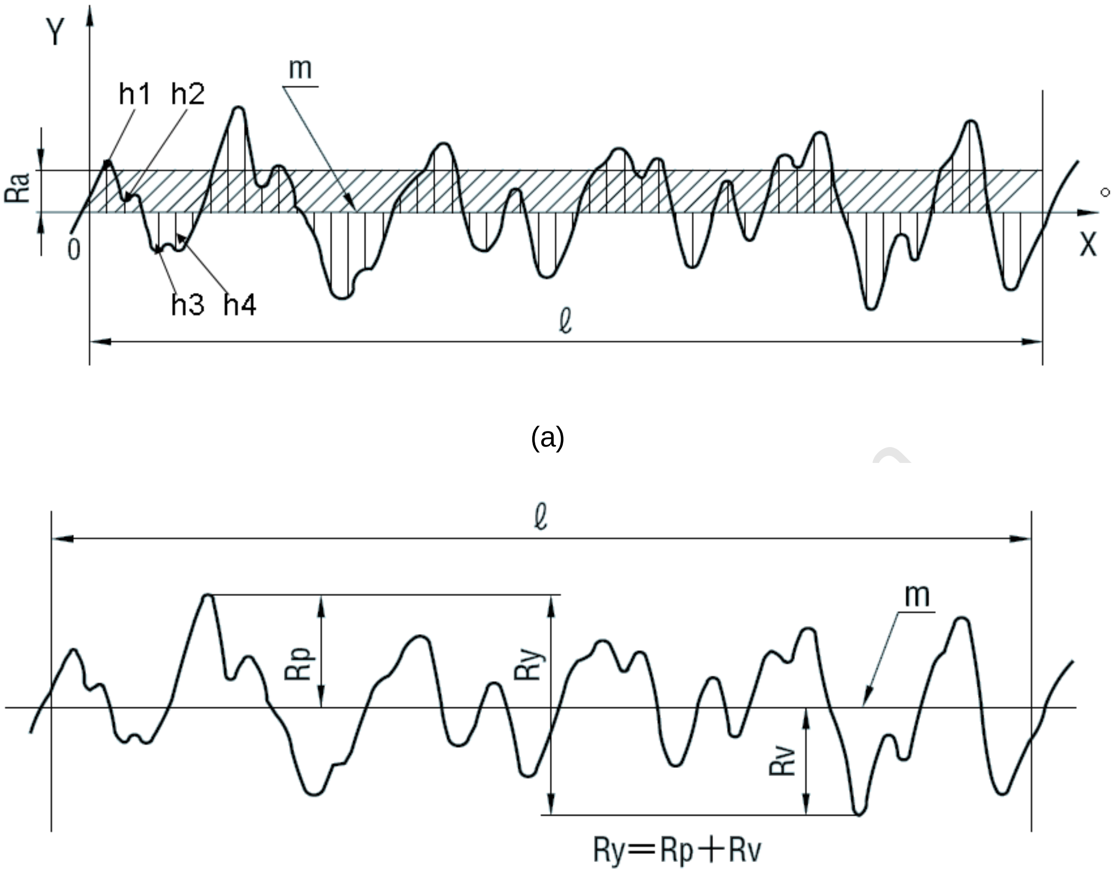

(a)

(b)

Figure 10: Diagrammatic representations for the determination of (a) R_a and (b) R_y (http://www.misumiamerica.com/CategoryImages/Metric_2009_pdf/p2839.pdf).

$$R_a = \frac{h1 + h2 + h3 \ldots hn}{L}$$ (Rank Taylor Hobson Limited n.d.)

$$R_a = \frac{1}{L}\int_0^L | y(x) | \, d(x)$$ (Hutchings 1992)

Where:

h = heights of asperities above or below the mean line,

L = Sample length,

y = height of the surface above the mean line at a distance *x* from the origin, When two surfaces interact the contact occurs between that of the asperities of the two bodies. As the load is increased these asperities deform allowing a greater area of contact and an increase in the number of asperity contact points (Lansdown and Price 1986). The true area of contact between the asperities thus increases, tending toward the apparent area of contact. This occurs more readily for metals of low yield strength as the load required to plastically deform the asperities is much lower. In the case of a static load moving into a tangential force the area of contact is further increased (Gahr 1987).

3.2 Friction

Friction is classified as the generated resistance to motion that occurs when tangential movement is attempted or induced between two surfaces. When a small tangential force is applied to a resting object and no movement occurs it can be said that the frictional force is equal in magnitude but opposite in direction to that tangential force. This is considered as the first qualitative law of friction. However if the tangential force is large enough to initiate motion then the frictional force between the surfaces is parallel and equal in magnitude to the tangential force but acts in the opposite direction. This property is classified as the second qualitative law of friction (Rabinowicz 1995). The force that needs to be exceeded to initiate motion between two surfaces is known as the static frictional force. The tangential force required to maintain motion is called the kinetic frictional force and in most cases it is lower in magnitude than the static frictional force (ed. Halling 1983).

Quantitative representation of the friction laws was first postulated by Guillaume Amonton in 1699 and hence the friction laws have adopted his name. An illustration of the two Amonton friction laws is shown in Figure 11 from Williams (1994). The friction laws are as follows:

1. The frictional force is directly proportional to the normal load applied between the two surfaces, illustrated in Figure 11 (a) and (b). From this law the following relationship can be drawn:

   $$F = \mu W$$

   Where F is the frictional force, μ is the proportionality constant known as the frictional coefficient and W is the normal load acting on the system (Hutchings 1992). The friction coefficient, μ, is dependent on both surfaces in the mated pair as well as conditions such as temperature and humidity (Williams 1994).

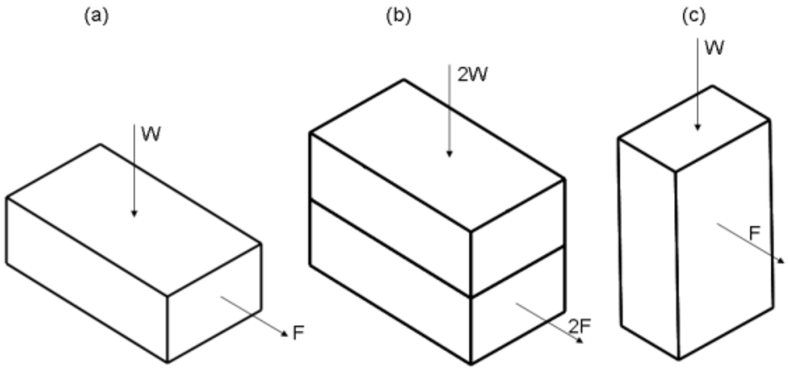

Figure 11: Amontons' laws of friction (a) A tangential force F is required to move the block of weight W (b) Doubling the weight doubles the tangential force required (c) the tangential force required remains the same even if the apparent area of contact is changed (Williams 1994).

2. The frictional force is independent of the apparent area of contact. This is illustrated in Figure 11 (c).

3. A third law, named the Coulomb friction law after Charles Coulomb, a French scientist, relates sliding velocity to kinetic coefficient of friction (μ_k). It states that the kinetic coefficient of friction is independent of sliding velocity (Williams 1994). This, however, does not hold true for low sliding speeds and high sliding speeds (tens or hundreds of metres per second). The former situation shows an increase in the μ_k while at the higher speeds there is a negative slope for the μ_k versus distance curve (Hutchings 1992).

When considering the actual mechanism of friction many factors play a role in generating the specific frictional force of the system. About 90% of the frictional force is caused by the shearing of atoms past each other during the sliding motion; other contributions include the roughness of the surfaces, the degree of ploughing into the softer material as well as electrostatic effects (Guichelaar 2008). In the case of high degrees of roughness, one surface has to move over the asperities of the other. This lift requires work to be done which increases the energy required for motion subsequently increasing the frictional force. During ploughing the asperities of the harder material tunnels through the softer material, this deformation in the surface of the softer substance requires additional energy which in turn causes an increase in the frictional force (Rabinowicz 1995).

3.3 Friction in metals

Properties of metals with respect to tribological applications in situations of little or no lubrication are highly affected by the layers that are generated on the surface of the metal. Figure 12 gives a diagrammatic representation of these layers (Rabinowicz 1995).

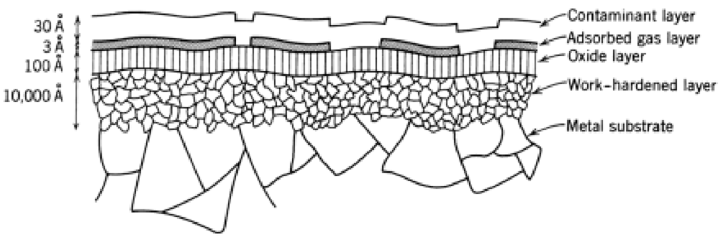

Figure 12: Layers found on an unlubricated metal surface (Rabinowicz 1995)

The contaminant layer consists of oily films. The oily films are derived from various sources namely natural greases of fingerprints or drops of lubrication solutions initially applied to the industrial system. The second layer is an adsorbed gas layer which mainly constitutes water vapour and oxygen. The two layers mentioned decrease the surface interaction between the sliding materials in the tribosystem, thus lowering the friction. The next layer is the oxide layer that forms as a result of the metal reacting oxygen. This holds for all metals besides that of the noble metals which include the pure and various alloyed forms of gold and platinum (Rabinowicz 1995). Due to the fact that friction between oxide surfaces or oxide and metal surfaces is much less than metal to metal friction the presence of this oxide film greatly affects the friction experienced by the metal component (Hutchings 1992).

During the process of the forming of the metallic component a section underneath the surface becomes work hardened, this layer generally remains unless heat treatments are performed which relieve the residual stress. The plastic deformation causes an increase in strength related to greater surface hardness of the material (Edwards & Endean 1990). Dong and Li (2000) diffused oxygen into a titanium matrix to subsequently increase the surface hardness of the article by forming a case hardened layer of α-phase titanium. It was shown that by increasing the hardness of the surface a decrease in friction occurred and an increase in the wear resistance was achieved.

3.3.1 *The effect of temperature on friction in metals*

Temperature plays an important role in the friction of a tribosystem. For metals which have crystal structures of the types Cubic Close Packed (c.c.p.) and Body Centred Cubic (b.c.c.) an increase in the temperature causes a decrease in the shear strength of the material. However this property does not occur with Hexagonal Close Packed (h.c.p.) structures as an increase in the temperature does not affect the frictional behaviour of the materials (Hutchings 1992).

The heat generated at the contact surfaces causes the formation of oxides. When a sufficiently thick layer of oxide is formed the µ will decrease as the contacting materials are no longer metal to metal but ceramic to metal, which has a lower range of µ values (Rabinowicz 1995).

3.3.2 *Stick slip*

When the motion of metal on metal or metal on non-metal surfaces are closely observed it can be seen that the motion involves periods of sliding as well as periods of rest; this is known as stick slip (Perring et al 1994). A simplified model to explain the mechanics of stick slip is shown in Figure 13 from Van De Velda, De Baets & Degrieck (1998).

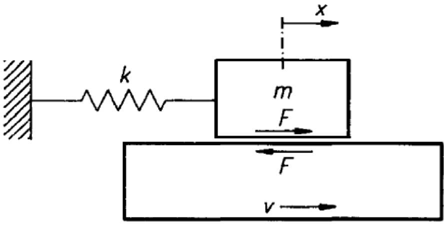

Figure 13: Stick slip model
(Van De Velda, De Baets & Degrieck 1998).

During the stick phase between the two contacting surfaces no motion occurs and the velocity is zero, however when slip is initiated the relative velocity between the materials increases from zero to a maximum velocity. This phenomenon is usually observed at slow sliding speeds and the accepted notion for the occurrence is that the static friction coefficient is greater than the kinetic frictional coefficient (Zang & Li 2002) (Popp & Stelter 1990).

The diagram above (Figure 13) shows a mass “m” connected to a wall by a spring of stiffness “k”, and resting on a plate which moves at a constant velocity “v”. Initially the mass moves with the plate (to the right) due to the static friction between the contacting surfaces, this can be considered the “stick” phase of stick-slip. As the pair move together the spring tension increases due to “k” and the increasing tangential force (to the left) is applied to the mass. This continues until the tangential force is great enough to overcome the static friction between the two bodies and sliding occurs; known as the slip-phase. The mass will accelerate to the left until the spring force equals the frictional force but will remain moving due to its kinetic energy. It finally decelerates because the frictional force is greater than the spring force (Van de Velde et al 1997).

Stick-slip plays a major role in the wear of materials due to fretting; where the latter phenomenon is the loss of the material due to a low amplitude oscillatory motion between the two surfaces of a tribosystem. For fretting wear stick-slip can be classified into three categories namely, gross slip, mixed slip and partial slip, gross slip being the most severe (Jeong et al 2006).

Smith et al (2005) investigated the mechanisms of stick-slip and wear that occurred during nano-scratching of a pyramidal diamond tip through a Ag substrate. It was shown that the stick-slip that originated was related to the phenomenon of dislocation emission in the material just below the indenter providing a stress relief zone, as well as a pileup that occurred around the hole leading to an increase in the frictional force and a reduction in the motion of the diamond tip; referred to as a stick occurring event (Figure 14). A point was reached where the force of motion increased beyond the resistance caused by the pileup around the hole and motion resumed; this is slip occurring.

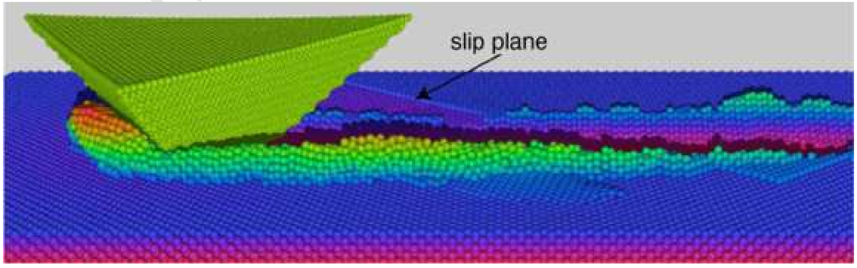

Figure 14: Diamond tip ploughing through surface showing the slip plane as well as material pileup along the wear track (Smith et al 2005).

3.3.3 Frictional behaviour

Severe or mild cases of friction can occur in a tribosystem and these are categorised on the range and fluctuation of the µ values, wear particle size as well as the wear rates of the materials. For severe frictional behaviour the µ ranges between 0.6 and 1.2 (Rabinowicz 1995) with wear particle sizes ranging from 1 to 100µm in diameter (Marumoto & Hirattsuka 2005); wear rates during severe conditions tend to be between 10^{-7} and 10^{-5} mm^2/N (Rabinowicz 1995). Another characteristic of the severe frictional behaviour is that instantaneous µ values show a high degree of fluctuation. For the case of mild frictional behaviour the µ values are typically in the range of 0.3 to 0.6 with a low degree of fluctuation. Much smaller particles are observed with diameters in the range of 10 to 100nm and the wear rates normally are less than 10^{-8} mm^2/N (Marumoto & Hirattsuka 2005).

3.4 Wear

3.4.1 Classification of Wear

Table 4 provides a brief description of the various wear mechanisms encountered. This section will focus on three main modes of wear including abrasive, corrosive and adhesive wear mechanisms.

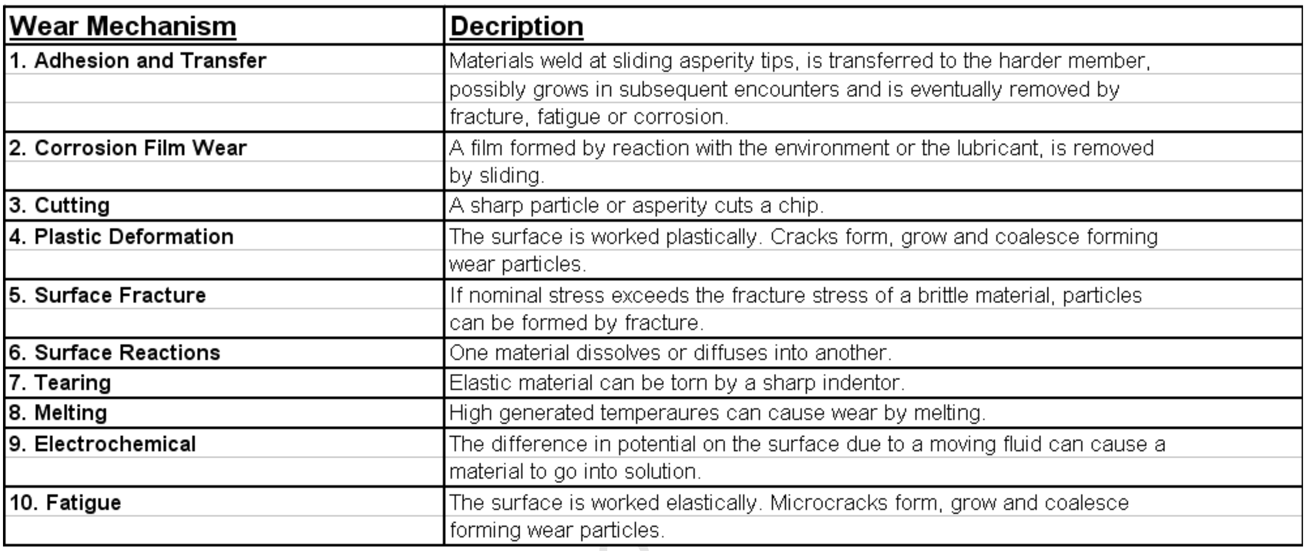

Wear Mechanism	Decription
1. Adhesion and Transfer	Materials weld at sliding asperity tips, is transferred to the harder member, possibly grows in subsequent encounters and is eventually removed by fracture, fatigue or corrosion.
2. Corrosion Film Wear	A film formed by reaction with the environment or the lubricant, is removed by sliding.
3. Cutting	A sharp particle or asperity cuts a chip.
4. Plastic Deformation	The surface is worked plastically. Cracks form, grow and coalesce forming wear particles.
5. Surface Fracture	If nominal stress exceeds the fracture stress of a brittle material, particles can be formed by fracture.
6. Surface Reactions	One material dissolves or diffuses into another.
7. Tearing	Elastic material can be torn by a sharp indentor.
8. Melting	High generated temperaures can cause wear by melting.
9. Electrochemical	The difference in potential on the surface due to a moving fluid can cause a material to go into solution.
10. Fatigue	The surface is worked elastically. Microcracks form, grow and coalesce forming wear particles.

Table 4: Classification of wear mechanisms (Peterson & Winer 1980).

3.4.2 Abrasive Wear

This mechanism of wear occurs when an asperity of the harder materials ploughs through the surface of the softer material leaving deep scratches. The material that is removed from the softer surface is deposited either on the harder surface, softer surface or remains as wear particles between the sliding surfaces (Rabinowicz 1995). The latter case of the generation of loose wear particles is the most common and the method then results in three body abrasive wear. Many experiments have shown that dirt plays a major role in the three body abrasion and thus proper cleaning standards of mating surfaces must always be employed (Peterson & Winer 1980). In certain cases very fine abrasive wear and a gentle type of adhesive “abrasive” wear between the harder and softer material results in the difficulty of distinguishing between the two modes. The latter of the two modes occurs when small particles of the harder material are transferred to the softer material resulting in the wear of the harder material via scratching. Generally, to distinguish between the two modes a profilometer can be used to measure the depth of the scratches produced (Rabinowicz 1995).

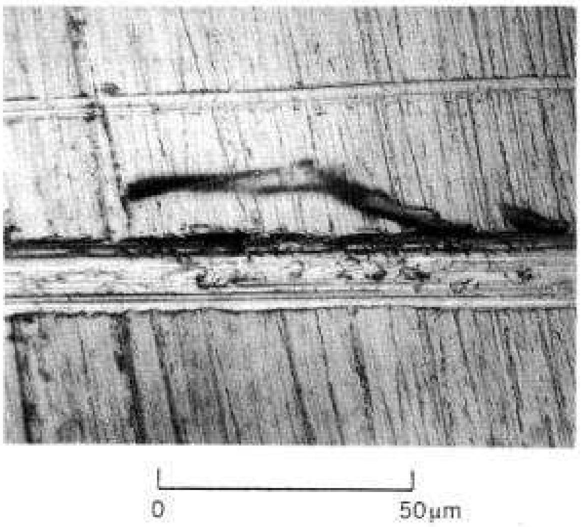

Figure 15: Abrasive track caused by the sliding of emery paper against steel (Rabinowicz 1995).

Figure 15 shows the abrasive wear that occurred during sliding between a steel surface and emery paper. The large chip seen above the abrasive track was also produced by abrasive particles (Rabinowicz 1995).

3.4.3 Corrosive Wear

Corrosive wear occurs when sliding takes place in a corrosive environment leading to a combined wear occurring. In some cases when sliding is halted the wear particles form a protective film which restricts or inhibits further corrosion from occurring. The problem then arises when sliding resumes and this protective layer is removed causing further corrosion and added loss of material through sliding wear (Rabinowicz 1995). During dry sliding, high flash temperatures can be reached on the asperity tips leading to the formation of an oxide layer. If this layer is removed by subsequent contact between asperities another oxide layer will result. In this way oxide debris is generated in a process called “oxidative wear”.

Another mode of generating oxidative wear is by the oxidation of wear debris due to the high temperatures generated during sliding. The oxide debris then acts as abrasive particles resulting in ploughing of the surfaces (Hutchings 1992). Although oxidative wear is considered a mild form of wear in metals it can greatly retard the performance of a purposefully generated surface layer on a metallic surface as the oxide particles plough in and remove material (Peterson & Winer 1980).

3.4.4 Adhesive Wear

Earlier in this document the actual mechanism of friction was broken down into various sources, the main source being the shearing of the relative materials that occur at the asperity tips. Following is an overview of that adhesion theory of friction. For this theory the total area of contact between the two surfaces is a function of the normal load, W, as well as the hardness of the softer material. Equation (a) shows this relationship:

Equation (a) $$A = \frac{W}{H}$$

Where:

A = True area of contact
W = Normal Load of the system
H = Hardness of the softer material

To initiate motion the junctions formed at the asperity tips must be sheared thus the friction force is proportional to the shear stress of the softer material as well as “A”. Equation (b) shows this relationship:

Equation (b) $$F = s \times A$$

However, from the quantitative representation of Amonton’s first law i.e. $F = \mu W$, and Equation (b) the following relationship can be formulated:

Equation (c) $$\mu = \frac{s}{H}$$ (Guichelaar, Dr. P. Et al 2008)

Although equation (c) represents a simple expression for the adhesion theory of friction is doesn’t take into account elastic deformation at the asperity tips. However, it does provide a logical explanation of Amonton’s laws of friction (Peterson & Winer 1980).

Adhesive wear involves the transfer of material from one smooth surface to the other due to the strong adhesive forces between the two surfaces. The transferred fragments may be deposited back on the original material or fall off the surface to become small wear particles causing the system to exhibit a change of wear modes i.e. from two body to a three body wear system. The process of material transfer occurs when two similar sections of either surface comes into contact and when the contact is broken the break may occur through one of the material surfaces and not at the actual area of contact. Figure 16 is a diagrammatic representation of the two paths that are possible when two surfaces come into contact during sliding wear. If the shearing stress at the junction of the two surfaces is greater than the shear strength of the bulk of the top material then path 2 is favoured. This would then lead to the transfer of material from top to bottom. However, this does not readily occur as the shear strength of the material at the junction is generally weaker than the bulk; due to a higher degree of vacancies within the bulk (Rabinowicz 1995).

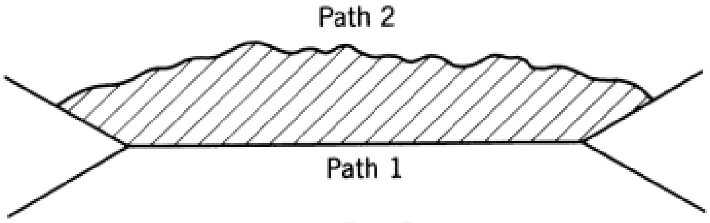

Figure 16: Representation of the two possible paths when two surfaces come into contact during sliding
(Rabinowicz 1995).

Plastic deformation wear can be produced in many ways. One of the earlier theories was that the fragments were produced from the asperity tips via adhesive wear. However the creation of a wear fragment formed as a result of plastic deformation can occur without adhesion. For example when the shearing of the layers beneath the asperity tip is combined with the propagation of a crack close to this surface, a wear particle can be produced. In this case the wear particle is produced by mechanical interaction between the two surfaces (Hutchings 1992).

In a similar situation the wear fragment is generated by shearing at the surface of the asperity tip and subsequently transferred to the other surface via adhesion. This leads to a new asperity on the other surface, which is plastically deformed and thus harder resulting in ploughing occurring into the original surface. This type of wear would be represented by straight grooves in the wear track (Chen et al 2007).
The delamination theory proposes that cracks originate below the surface in the plastically deformed layer and these cracks propagate until a fragment of the material is

removed. This fragment has a plate like shape. A study conducted by Molinari et al (1996) showed that at lower sliding speeds the typical wear regime for Ti-64 was oxidative. However, as the speed was increased the mode of wear changed to delamination.

In situations when the sliding speed is increased this causes higher surface temperatures and results in a higher degree of plastic shearing of the material surface, due to a drop in the shear strength of the material. As a consequence there is more material build-up in front of the sliding surface (e.g. wear pin) which forces the change in direction of motion; either over this higher density plastically deformed layer or around it. As a result the grooves formed from ploughing change from being straight to wavy. At some stage the sliding velocity will be such that it will result in a decrease in the deformation of the surface due to material softening and/or melting and will be smeared by the other surface. This type of wear is characteristic of smear wear. It is to be noted that at low sliding speeds the time of contact of asperity tips is higher thus leading to stronger adhesive forces resulting in a larger shearing action required to break the junction. For this reason low sliding speeds for the same material pair yield higher frictional coefficients (Chen et al 2007).

3.4.5 Wear of metals

During the wear in metallic systems many factors govern the type of wear experienced and consequently the frictional behaviour of the mated system. Factors such as material hardness, the wear environment, compositional make-up of the material, sliding speed and the applied load all act within a system to generate a specific wear regime characteristic for the parameters of that system. It is because of these many variables and the dramatic changes they cause on the dominating wear mechanism that make predicting wear scenarios a difficult practice.

3.4.5.1 The Archard wear equation

The first models to evaluate adhesive and abrasive wear considered the interaction between asperities and the resulting plastic flow at these junctions. It modelled the volume loss of a wear system under these wear scenarios as being directly proportional to the applied load in the system and inversely proportional to the hardness of the softer material in that system. The relationship is as follows:

$V = K\frac{W}{H}S$ (ed. Hutchings 1997)

Where:
V = Wear volume
K = Wear coefficient (dimensionless)
W = Normal load applied to the system
H = Hardness of the softer material of the mated surfaces
S = Sliding distance

The equation was named after John Archard, who refined the above equation by making the following assumptions (Podra and Anderson 1997):

1. Contacting surfaces between two bodies of a tribosystem will occur at the asperities of those bodies
2. The actual contacting area is directly proportional to the applied normal load in that system
3. The interaction areas of the asperities are circular in nature
4. For metals, the deformation experienced at these contacting asperities are always plastic
5. The system is isothermal

Archard attributed “K” as being the probability of a wear particle being generated at a point of contact between the two surfaces. Similarly it was shown that a single abrasive interaction between two surfaces can also be quantified in the Archard equation, where “K” is now a geometric factor associated to the average strain.

3.4.5.2 Mild wear in metals

Mild wear is generally classified when wear coefficients range between 10^{-6} and 10^{-4}. The mild wear regime is characterised by localised wear which interprets to material loss along asperities junctions. This is usually the case for relatively hard metals. If flash temperatures at the asperity contacts are sufficiently high the metal will oxidise, provided the atmosphere is oxygen reach. This produces very fine particles of wear debris. If the underlying metal is exposed, due to spalling of the oxidised areas, it will oxidise again, repeating the process. Work performed by Rosenberg and Jordaan (1934) prompted them to make the following assumption regarding oxidation of steel. They postulated that in an oxygen containing environment that the oxide formed would prevent the severe wear regime from arising in steel of any hardness, however, that if the rubbing occurred in a nominally oxygen free environment that only sufficiently hardened steels would be protected by this layer.

A second type of mild wear arises from the transfer and subsequent back transfer of material between the two surfaces. Metal from either surface can combine in a type of alloy mix (of both the counter-face and pin metal) which serves as a protective layer to the underlying material. Wear proceeds against this surface thus lowering the overall wear rate of the base material. The ability of the layer to provide protection is directly related to its hardness and the attachment to the substrate (ed. Hutchings 1997).

3.4.5.3 Severe wear in metals

Severe wear is characterised by the mechanism of adhesion and plastic deformation. It results in large areas of material being removed and is not localised to asperity junctions as that observed for the mild wear regime. The removal of larger segments of material results in the surface becoming increasingly irregular in shape which greatly increases the wear rate of the system (Gahr 1987). Wear coefficients for the severe wear regime are typically in the range of 10^{-4} to 10^{-2} (Hutchings 1997).

As discussed before the mild wear regime is characterised by oxidation type wear. However, when this oxide film is degraded and subsequently breaks down a sharp increase in the wear rate is observed as the underlying material is exposed and the oxide particles cause micro-ploughing into the surface of the exposed metal. The wear rate of such a system will then steadily drop as the exposed metal then becomes oxidised, mild wear will then persist until a critical thickness of the oxide is reached and the load-bearing capability is exceeded (Gahr 1987)

Severe wear is visible as large amounts of transferred material, a rough, torn surface showing large amounts of plastic deformation and the presence of large metallic wear fragments (Peterson & Winer 1980).

3.4.5.4 Wear transitions

As previously discussed the type of wear experienced by a system is largely dependent on the load – speed combination as well as the material properties (Hutchings 1997). Work performed by Welsh (1964) was successful in showing that the wear regime for steel is affected by load, sliding speed, composition and hardness of the steel. Clear distinctions could be made of the transitions between the two wear states i.e. mild and severe. In this regard critical loads, speeds, compositions and hardness values governed these transitions, provided that the remaining variables were kept constant. During his work Welsh noticed three transitions in the wear rate of the steel: (1) a change from the mild wear regime to the severe state [T_1], (2) a change from the severe state back to a mild mode of wear [T_2] and (3) a non-linear zone of mild wear after T_2. Figure 17 (a) is an example of a wear rate vs. load curve used to identify the transition loads at a particular speed. Curves such as these are varied for the speed parameter over the same load range to identify how this affects these key points of transition. From numerous plots of this kind Figure 17 (b) can be constructed, which shows how the transition load is affected by the sliding speed. The shaded area denotes the parameters which will produce severe wear.

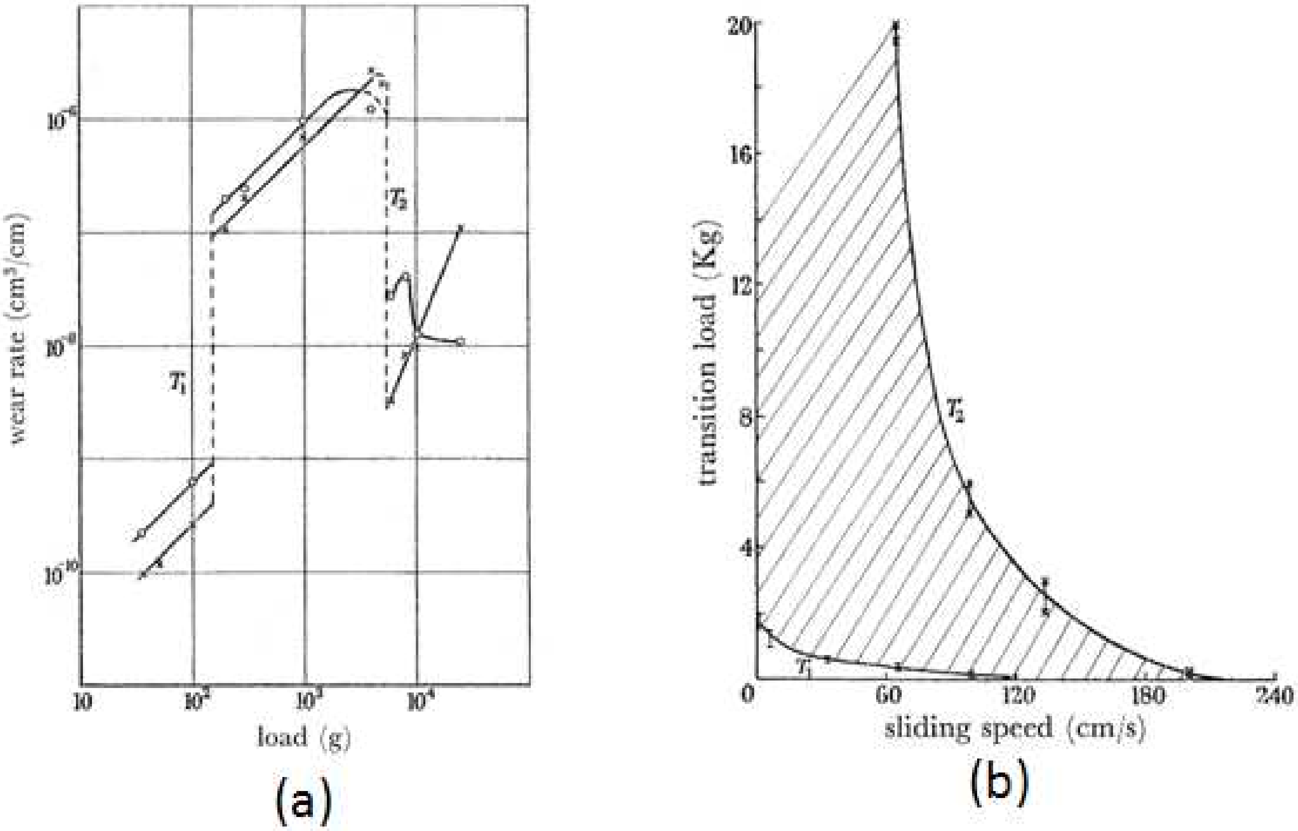

Figure 17: (a) Wear rate as a function of load plot for a 0.52%C steel. Plot shows the two points of transition, T_1 and T_2. The plot assigned by "-o-" is for the counter-face ring while "-x-" denotes the pin wear rate. Speed was set at 100cm/s. (b) Illustrates the change in transition load with sliding speed for the 0.52%C steel

Using the types of curves shown above Welsh (1964) was able to show that an increase in hardness would elevate T_1 and depress T_2 such that at a particular hardness the severe regime of wear would not occur for the mated pair.

3.5 Linear Reciprocating Ball-on-Flat Sliding Wear (ASTM G133)

The ASTM standard discussed in this section provides procedures for the characterisation of wear performance for a ball-on-flat arrangement during linear reciprocating sliding wear motion under lubricated and unlubricated conditions. Motion between the two surfaces occurs in a straight line with a periodic change in the direction. During analysis the relevant quantities include volume loss caused by wear and the coefficient of friction. For the scope of this thesis only unlubricated conditions will be considered relevant.

3.5.1 Apparatus

3.5.1.1 General

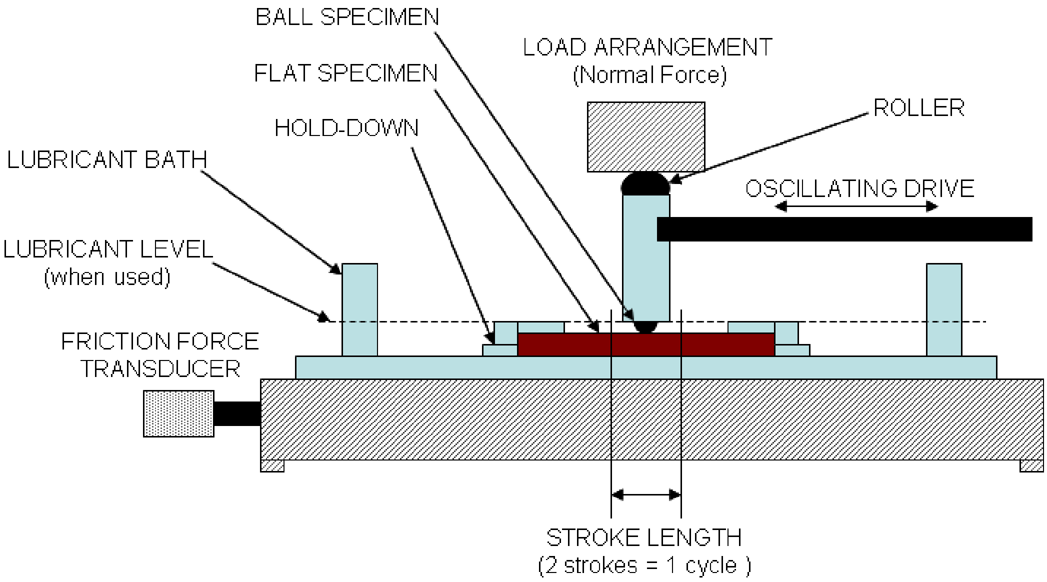

Figure 18: Linear Reciprocating Test Rig Setup (ASTM G133).

Figure 18 is an illustration of the setup of the linear reciprocating apparatus. A uniform normal load is applied to provide the desired normal force between the ball and flat specimen. A spherical specimen is used to avoid complications of alignment caused when flat-ended balls are used to wear against flat specimens. ASTM G133 discusses motion of the ball against a stationary flat specimen; however, a configuration whereby the flat specimen moves and the ball is stationary may also be used. Tangential forces are measured continuously using a friction force transducer and these measurements are used to produce frictional coefficient data. Ambient temperature conditions as well as sample temperature is measured.

3.5.1.2 Spherically tipped specimen and its sample holder

The ball specimen may either be a bearing ball or any spherically ended specimen; in the former case the bearing ball should be securely clamped in place to prevent slipping during contact with the flat specimen while in the oscillating motion of the test. The holder should also be rigidly placed such that no tilting occurs during the test.

3.5.1.3 Flat specimen holder

The flat specimen must be clamped in such a way as to present the ball specimen with a smooth, horizontal flat surface.

3.5.1.4 Friction force transducer

A friction force transducer or load cell is used to continuously measure the tangential force during the test. This load cell must be calibrated in both directions of motion. The method of calibration for the load cell for this particular report is discussed in the experimental procedure section.

3.5.1.5 Loading system

A deviation of 2.0% is allowed for the constant statically applied normal loads e.g. for a 25N load ±0.5N.

3.5.1.6 Test duration

To compute the total sliding distance of the wear tests the following relationship between variables is used:

$$X = 0.002 * t * f * L$$

$$N = t * f$$

Where:
X = total sliding distance (m),
N = number of cycles in the test,
t = test time (s),
f = oscillating frequency (Hz),
L = length of stroke (mm).

A single cycle is classified as a back and forth motion of the ball i.e. two stroke lengths.

3.5.1.7 Temperature and humidity

During room temperature tests the ambient temperature must be measured. As in the case with some materials humidity affects the wear characteristics and for this reason humidity must be measured.

3.5.2 Procedure

3.5.2.1 Sample preparation

Both samples are either tested in polished conditions or by some predetermined conditions relevant to the testing procedure. Typical polished conditions are between 0.02 and 0.05µm R_a. Sample cleaning consists of the following:

1. Wash with a mild liquid glassware cleaner,
2. Hot air dry,
3. Ultrasonically clean in acetone for 2 min,
4. Hot air dry,
5. Ultrasonically clean in methanol for 2 min,
6. Hot air dry,
7. Fix the samples in the respective arrangements, clean with cotton swabs soaked in acetone followed by cotton swabs soaked in methanol.

3.5.2.2 Testing procedure

ASTM G133 consists of two testing procedures, one for lubricated and the other for unlubricated conditions. For relevance only the latter will be discussed.

Once the samples are fixed in place and the final cleaning complete, gently lower the ball specimen onto the flat specimen, locking fixtures in place. The predetermined load is applied and the duration and speed of the test is set. The following testing conditions are those set by the ASTM G133 standard for unlubricated wear testing at ambient temperature:

1. Pin tip radius, 4.76mm,
2. Normal force, 25N,
3. Stroke length, 10mm,
4. Oscillating frequency, 5.0Hz,
5. Test duration, 16 min 40s (sliding distance 100m),
6. Ambient temperature, 22 ±3ºC,
7. Relative humidity, 40 to 60%;
8. Lubrication, none applied.

After the test is completed the load is removed before the friction capture is ended to recheck the zero point of the friction data capturing system. Samples are cleaned by a

jet of air to remove wear debris. The ball is checked for any slippage or rolling; if either is noticed the test must be discarded (this also applies to that of the flat specimen).
Any deviations from this procedure must be specifically reported.

3.5.3 Measurement and calculation of wear

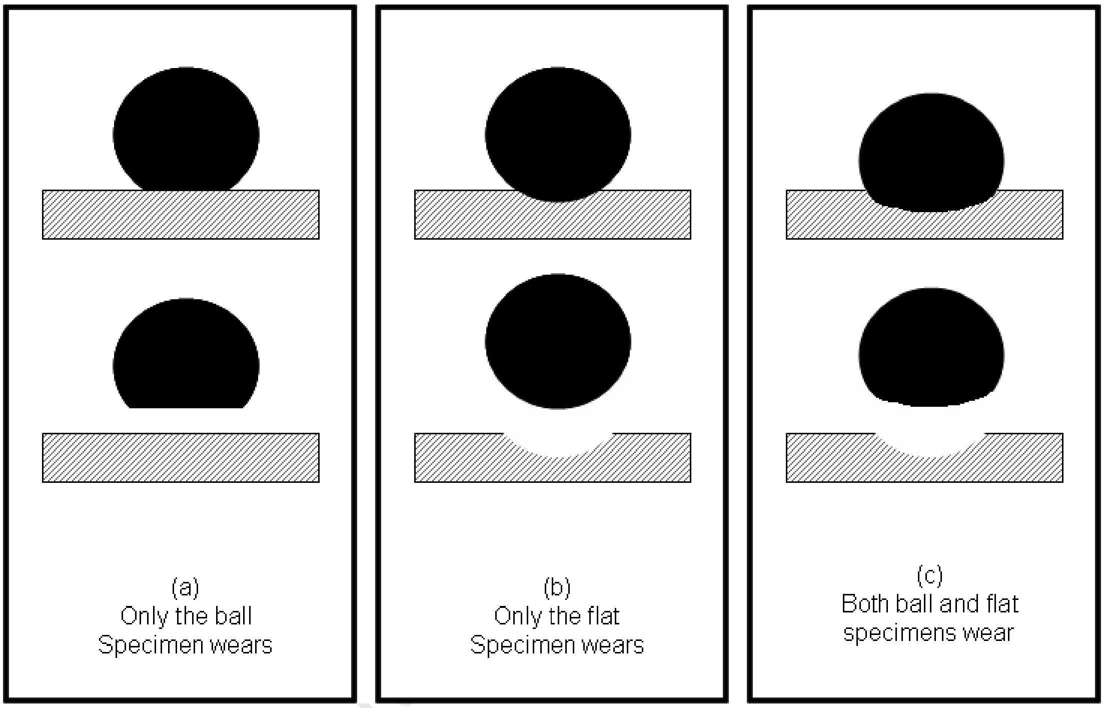

Figure 19: Possible Situations for Differing Wear Resistance of Ball and Flat Specimens (ASTM G133).

Figure 19 shows the various scenarios of wear that can occur between the ball and flat specimen. The calculations for wear volume loss for the various scenarios are covered in the following sections.

3.5.3.1 Wear of the ball specimen (Figure 19 (a))

The volume loss of the ball can be calculated from the following relationships:

$$V_p = (\pi h/6)[3D^2/4 + h^2]$$

$$h = R - [R^2 - (D^2/4)]^{1/2}$$

Where:
V_p = Wear volume of a flat ball wear scar,
D = Diameter of the circular wear scar,
R = Original ball radius,
H = Height of material removed.

If the wear scar on the ball specimen is flat but not circular a maximum and minimum measurement is taken and the average of the two will be used as the diameter of the wear scar (*D*).

3.5.3.2 Wear of the flat specimen (Figure 19 (b))

Calculation of the volume loss of the flat specimen can be obtained from the following relationship:

$$V_f = A \text{ x } L$$

Where:
V_f = Volume loss of the flat specimen,
A = Cross-sectional area of the wear track,
L = Length of the wear stroke.

A cross-section of the wear track is in the plane which is normal to both the sliding motion as well as the length of the track. Three cross-sectional strokes (spaced equally apart) of the wear track are taken to obtain an average cross-sectional area, however if the area of the three strokes differ by more than 25%, six strokes are necessary.

3.5.3.3 Wear of the ball and flat specimen (Figure 19 (c))

ASTM G133 (1995) does not provide any calculations pertaining to the situation found in Figure 19 (c). Analysis of this scenario was completed by Jun Qu et al (2006) whereby the study conducted involved four separate modes of analysis for the volume loss. These four methods were mass loss, 2D wear scar analysis, 3D analysis and a new method referred to as the single trace analysis. The first two and last methods were compared to the time consuming but highly accurate 3D analysis method. Single trace analysis requires only the wear scar diameter and a single profile trace through the plane of the centre of the wear scar and the ball. Volume loss of the spherical slider can be calculated as follows:

$$V = \frac{1}{3}\prod[h^2{}_o(3R_o - h_o) - h^2{}_w(3R_w - h_w)]$$

$$h = h_o - h_w$$

where

$$h_o = R_o - \sqrt{R^2{}_o - \frac{d^2{}_{scar}}{4}}$$

$$h_w = R_w - \sqrt{R^2{}_w - \frac{d^2{}_{scar}}{4}}$$

Figure 20 is an illustration of the variables of the above equations.

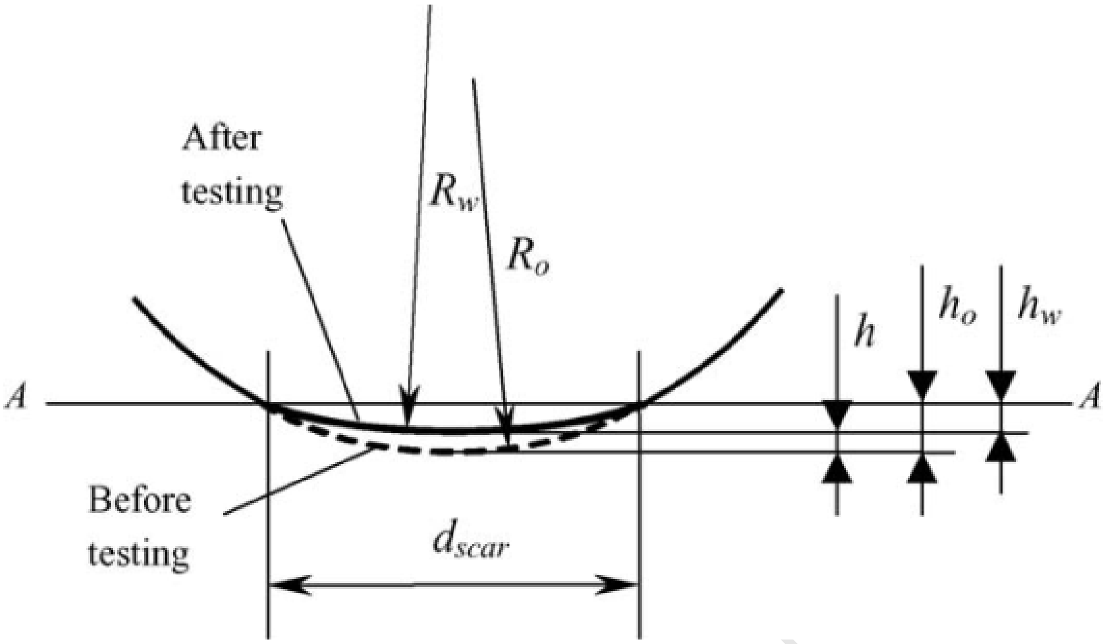

Figure 20: View of a worn tip of a spherically tipped slider (Qu & Truhan 2006).

Where:
R_o and h_o are the radius and height, respectively, for the slider condition before wear testing (below plane A-A),
R_w and h_w are the radius and height, respectively, for the slider condition after wear testing (below plane A-A),
d_{scar} is the diameter of the wear scar.

Wear volume of the flat specimen is calculated as follows:

$$V_f = L_s \left[R^2{}_f \ \arcsin\left(\frac{W}{2R_f} \right) - \frac{W}{2} \left(R_f - h_f \right) \right] + \frac{\Pi}{3} h^2{}_f \left(3R_f - h_f \right)$$

The formula itself incorporates three segments of the wear scar, namely the two spherical ends and the cylindrical surface in the centre as can be seen in the following figure, Figure 21.

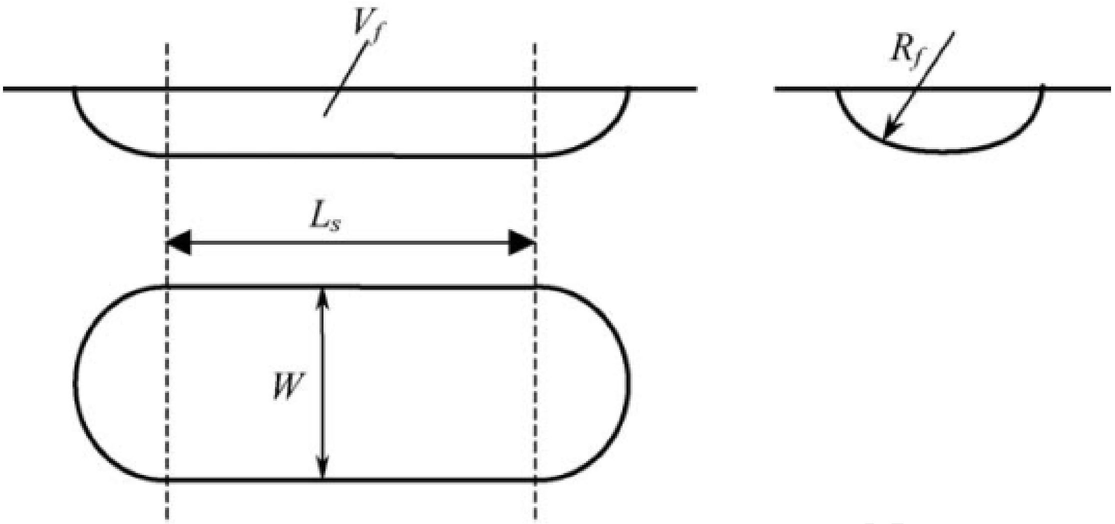

Figure 21: Wear scar on the flat specimen against a spherically tipped slider (Truhan 2006).

Where:
V_f = Volume loss of flat specimen
L_s = Length of stroke,
W = Width of wear track,
R_f = Spherical end radius.

A test conducted by Ju Qu et al (2006) in which a spherical slider of 440C stainless steel was unidirectionally slid against a Ti-alloy disc, Ti-6Al-2Sn-4Zr-2Mo, showed the comparison between the four methods of wear analysis of the spherical slider in terms of volume loss. The results of the tests are shown in Table 5.

Method	Wear volume ($\times 10^{-3}$ mm^3)	Error compared to 3D analysis (%)	Time consumed (min)
Mass loss	25.6 ± 12.8	−21.7	~2
2D	39.9 ± 1.9	22.0	~3
3D	32.7	N/A	~45
Single-trace	33.1 ± 1.6	1.2	~5

Table 5: Comparative results of the various analytical methods to calculate the wear volumes of ball and flat specimens (Ju Qu et al 2006).

4 LITERATURE REVIEW: SURFACE MODIFICATION

4.1 Thermal Oxidation

This process produces a thick adherent oxide layer on the surface of the titanium substrate to increase its wear resistance, surface hardness and corrosion resistance (ASM international 1994). Oxidation of titanium produces various oxides depending on the composition of the titanium specimen i.e. alloying elements present. These elements can either be one of three types that affect the oxidation of the titanium sample; neutral, detrimental or beneficial. Looking at Ti-64, V is detrimental to the formation of the oxide layers while Al is beneficial, provided the content of the Al is high enough it will result in the formation of the stable α-Al_2O_3 (Gulyeryuz & Cimenoglu 2009). The thickness and adherence of the oxide layer greatly depends on the temperature of oxidation as well as the oxidation time as shown by Dong and Li (2000). Table 6 shows the type of metal oxides formed on the titanium surface when oxidation is performed for CP-Ti and Ti-6Al-4V (Long &Rack 1998).

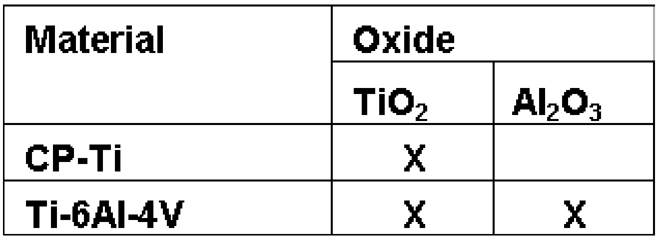

Material	**Oxide**	
	TiO_2	**Al_2O_3**
CP-Ti	X	
Ti-6Al-4V	X	X

Table 6: Oxides formed during oxidation of Cp-Ti and Ti-6Al-4V (Long & Rack 1998).

Above 800℃ the oxide layer formed generally undergoes spalling if oxidation times are too long and lowering the temperature requires longer exposure times which are more costly and do not produce thick layers. To produce a sufficiently thick and adherent oxide layer that is able to perform effectively for the desired application the correct temperature, oxidation time as well as the cooling rate needs to be precisely controlled (Siva Rama Krishana et al 2007). It should be noted that although the thermal oxidation treatments occur at elevated temperatures, in the range of 500-900℃, oxidation of titanium also occurs at low temperatures including ambient conditions provided there is an oxygen environment (Gulyeryuz & Cimenoglu 2009). As human body fluid is oxygen rich it provides an excellent environment for the formation of oxides on the titanium specimen, even if the prosthesis is damaged the speed of the “healing” effect that the oxide layer exhibits is in the degrees of milliseconds. This formation of the passive oxide layer on titanium as well as the excellent biocompatibility of rutile (TiO_2) within the human body makes titanium an excellent candidate for prosthetic implants (Velten 2000).

A study conducted by Vaquila et al (1999) investigated the stoichiometrical ratios of Ti and O present as various titanium oxides when the specimen was thermally oxidised. At low temperatures (<200℃), TiO_2 is present, for higher temperatures (200℃< T<350℃), however Ti_2O_3 is also observed, but as the temperature is increased the amount of TiO_2 increases and that of Ti_2O_3 decreases (Vaquila, Passeggi & Ferron 1996).

4.1.1 Formation of the oxide layer on Ti-6Al-4V

Work completed by Burnell-Gray et al (1994) showed that during the oxidation of Ti-64 in the temperature range of 650° to 850℃ under atmospheric conditions, Al_2O_3 and TiO_2 grew in alternate layers above the substrate. The number of these alternating layers increased as the temperature or time of exposure was increased. Figure 22 is an illustration of this process occurring. The presence of vanadium in the Ti-64 specimen was shown to decrease the aluminium activity and suppresses the formation of the alumina layer. The work performed by Burnell-Gray et al (1994) produces the following insight into the layers formed during oxidation of the surface of the Ti-64 specimen.

During early stages of oxidation the formation of the TiO_2 layer is favoured as the minimum titanium activity is approximately four orders of magnitude smaller than that of the minimum aluminium activity when the partial pressure of oxygen (pO_2) is 0.21 atm (atmospheric conditions). Once the thin TiO_2 film forms the pO_2 at the oxide/substrate interface decreases and thus the minimum aluminium activity at this pressure increases preventing the formation of the Al_2O_3 layer. The most important diffusing species for the investigation are Al, Ti and O. The first two species diffuse outward from the substrate while O diffuses into the substrate through the oxides. The pO_2 at the oxide/gas interface still favours the formation of TiO_2; however experimentally it is noticed that Al_2O_3 nucleates and grows laterally to form the Al_2O_3 layer. This occurs because at the oxide/substrate interface the outward diffusing Ti and the inward diffusing O combine to form TiO_2, as the formation of this layer is greatly favoured due to the drop of pO_2 at this region. Thus the Ti species is “trapped” at this region allowing for the Al_2O_3 to be more kinetically favoured at the oxide/gas interface. Through this method the TiO_2 and Al_2O_3 layer grows. However, several alternating layers of Al_2O_3 and TiO_2 are observed at the end of the oxidation process.

In the early stages of growth there would be good oxide/substrate contact due to the plastic flow of the oxide layer, but the plasticity of the oxides is very limited leading to cracking. The latter is due to the difference in expansion coefficients between the

substrate and the oxide. Cracking initiates at the edges and moves throughout the surface of the substrate. The cracks decrease the diffusion of Ti and Al dramatically; however, O diffusion still occurs through the oxides into the cracked region thereby increasing the pO_2. At the oxide side of the oxide/substrate interface no definitive reactions occur; however at the substrate side the conditions for the formation of the TiO_2 layer is favoured again. Once a thin film of TiO_2 layer is formed the Al diffuses to the oxide/gas surface of the second TiO_2 layer and the process repeats again.
The number of the alternating layers produced depends on the exposure time (Burnell-Gray et al 1994).

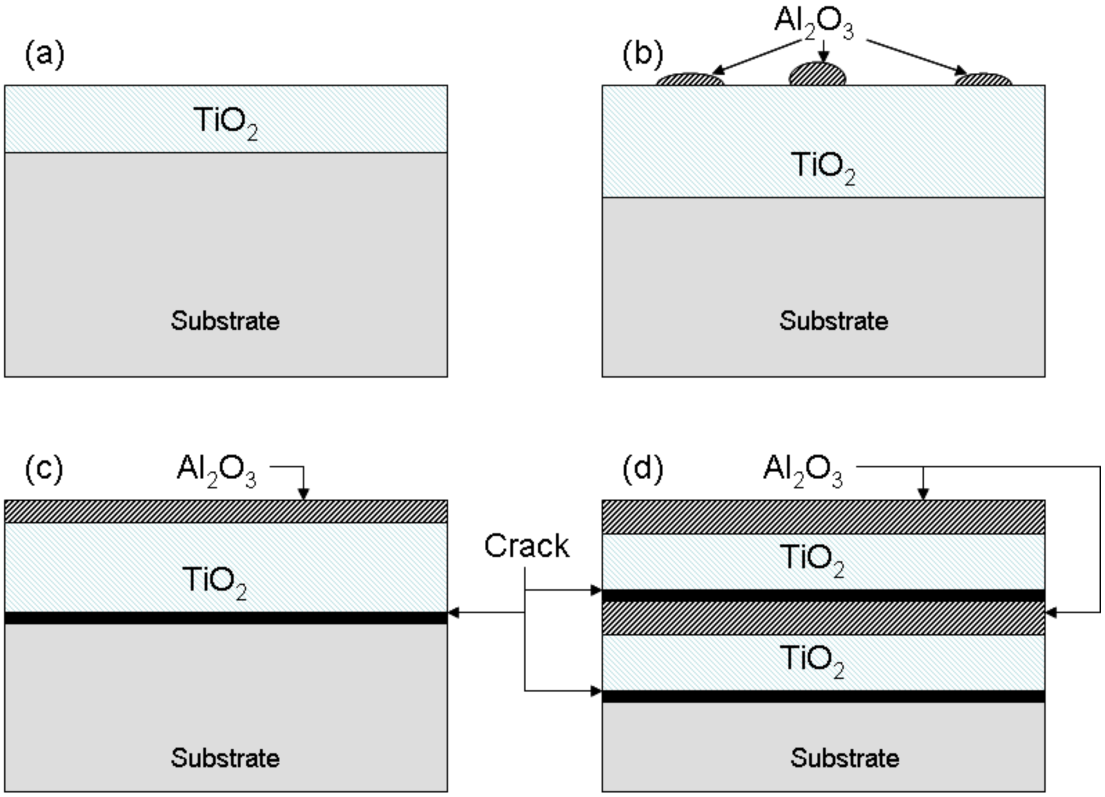

Figure 22: Diagrammatic representation of the mechanism of air oxidation of Ti-6Al-4V (a) formation of the rutile layer (b) nucleation of Al_2O_3 and the thickening of the rutile layer (c) formation of the Al_2O_3 layer and a crack (d) subsequent Al_2O_3 and Rutile layer formation (Burnell-Gray et al 1994).

As discussed earlier, as the oxide layer grows in thickness, there is an increase in the chance for delamination to occur at the oxide/substrate interface. This is due to the high value of the Pilling-Bedworth Ratio (*R*) for titanium (Johns et al 1996). The ratio can be defined by the following equation:

$$R = \frac{Md}{amD} \equiv \frac{V_{mo}}{V_{mc}} \text{ (Zang 2000)}$$

Where:

R = Pilling-Bedworth Ratio,
D = Density of metal Oxide,
M = Molecular weight of metal oxide,
a = Composition ratios for metal oxide i.e. $(\text{metal})_a(\text{oxygen})_b$,
m = Atomic weight of the metal,
d = density of the metal,
V_{mo} = Volume of the metal oxide formed,
V_{mc} = Volume of the metal consumed during oxidation.

A low *R* value, below 1, would imply that the oxide would not sufficiently cover the surface of the metal as the film would be porous (Figure 23 (a)). Metal-oxides with a value of 1<*R*<2, provides better coverage and protection to the underlying material (Figure 23 (b)). *R* values greater than 2 for the metal oxide films would suggest that the oxide contains high compressive stresses, which lead to delamination of the oxide layer from the metal surface shown in Figure 23 (c) (Zang 2000).

The Pilling-Bedworth ratio was first established for use in the oxidation of metals, but it is the alloys of these metals which are the most extensively used in industry. It has become frequent practice to evaluate the R value of the metal to provide insight into the growth stress experienced during the oxidation of the corresponding metal alloy. This can lead to discrepancies in the prediction for the type of stress experienced when oxides form on the alloy. Work by Xu and Gao (2000) showed this when assessing the R values for 3 different alloys of aluminium, namely Ni_3Al, NiAl and $NiAl_3$, and comparing the R values obtained for these Al_2O_3 producing alloys to the R value for Al. Using the standard equation for the Pilling-Bedworth ratio they determined that Al had a R value of 1.29 which differed considerably to the range calculated for the 3 different alloys. Their results are tabulated in Table 7.

Metal	R Value
Al	1.29
Ni3Al	1.71 - 1.88
NiAl	1.64 - 1.78
NiAl3	1.48 - 1.67

Table 7: Calculated R values for Al and three other Al_2O_3 forming alloys (Xu and Gao 2000).

Their results were correct in showing that the R values calculated for these three alloys were significantly different to that for Al. Their work was also successful in showing that the oxidation of the alloys was affected by the lattice parameters of the crystal. Although this might not be the outcome for the other metals and the corresponding alloys, care should be taken when using the R value of the metal to investigate oxidation in the alloy.

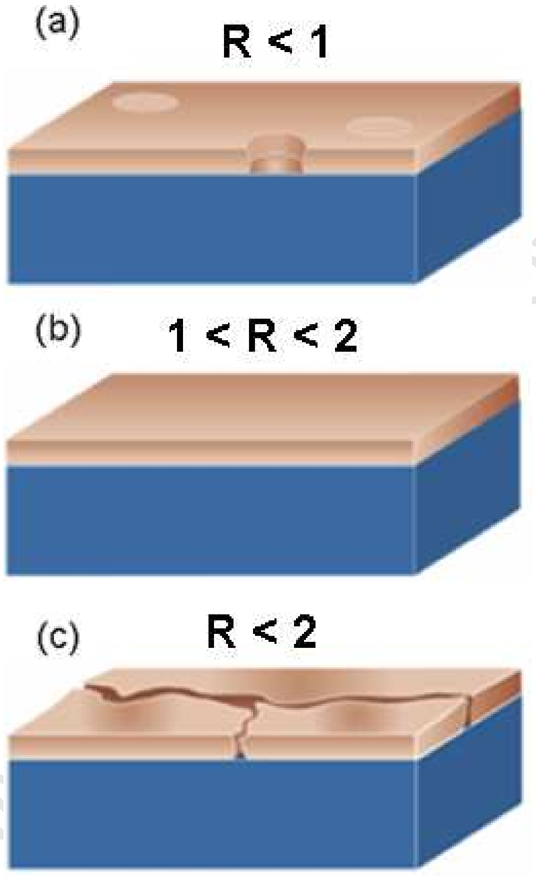

Figure 23: A diagrammatic representation for the various values of R and the significance to the potential of the oxide to cover the surface of the metal

When oxides are formed that are thick and adherent they can readily be used to improve the tribological performance of the underlying material. Much work has been performed in this regard, and the process of thermal oxidation has readily been employed for titanium articles.

4.1.2 *Tribological applications of oxidised titanium*

Wear mechanisms changed from plastically dominated wear to oxidation wear when untreated and thermally oxidised titanium samples were tested under different environments i.e. vacuum and room air respectively. This was shown by work performed by Yazdanian et al (2007). The purpose of the investigation was to assess the improvement in tribological performance of the Ti-64 material via the process of thermal oxidation. Surface hardness increased from approximately 382 HV to 1631HV after the thermal treatment process. The process included heating the Ti-64 samples to a temperature of 873K for 60 hours. A pin on disk wear rig was used at a speed of 0.05m.s^{-1} under a normal load of 2N for 250m. The samples were sectioned into 25mm (diameter) circular discs with 5mm thickness; counter-face specimens were in the form of 6mm SAE 52100 type steel balls. The test results show that no mass loss was detected for the thermally oxidised specimens in vacuum while the untreated samples had a wear rate of 2.67 x 10-4 mm^3/m. Wear mechanisms were dominated by stick-slip type plastic deformation. In the room air environment oxidation wear occurred and the treated samples showed a 90% improvement in wear resistance. The small debris examined showed that the oxides were that of both titanium and iron, and the material removal that occurred via abrasive tracks was in a direction parallel to the wear track of the untreated sample. The oxidised samples showed wear only in the oxide region of the specimen with material transfer occurring from the counter-face to the test sample (Yazdanian et al 2007). Another important factor in producing a thick adherent oxide layer is the cooling rate that is employed. Faster cooling rates results in spallation of the oxide layer; due to the difference in thermal expansion coefficients of the oxide and the metal (Siva Rama Krishana et al 2007).

Experiments were conducted by Siva Rama Krishna et al (2007) to determine the optimum conditions to produce a thick adherent oxide layer greater than 100µm on grade 2 titanium (CP-Ti). Their worked showed that samples oxidised in air at 850℃ for 5 hours showed the greatest capability of producing a thick oxide layer, typically greater than 150µm. This was achieved by furnace cooling which effectively increases the oxidation time as opposed to air cooling. Work by Dong et al (2001) showed a similar outcome for the oxidation of Ti-64 specimens at 850℃ carried out for 30 minutes. Figure 24 is a plot of thickness (µm) as a function temperature determined by Siva Rama Krishna et al (2007).

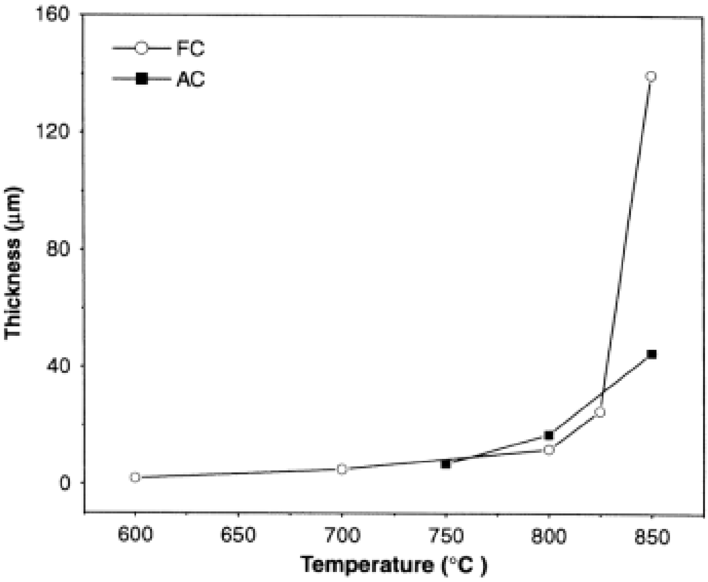

Figure 24: Plot of the oxide thickness achieved against temperature for furnace cooling (FC) and air cooling (AC) at a soak time of 5 hours (Siva Rama Krishna et al 2007).

It can be seen that both furnace cooling and air cooling show considerable increases in growth rate after 800℃; however, furnace cooling provides an oxide film three times thicker than air cooling. Figure 25 shows the SEM micrographs for the oxide layers formed by air and furnace cooling. The figure shows considerable adherence of the oxide layer to the substrate for furnace cooling (Siva Rama Krishna et al 2007).

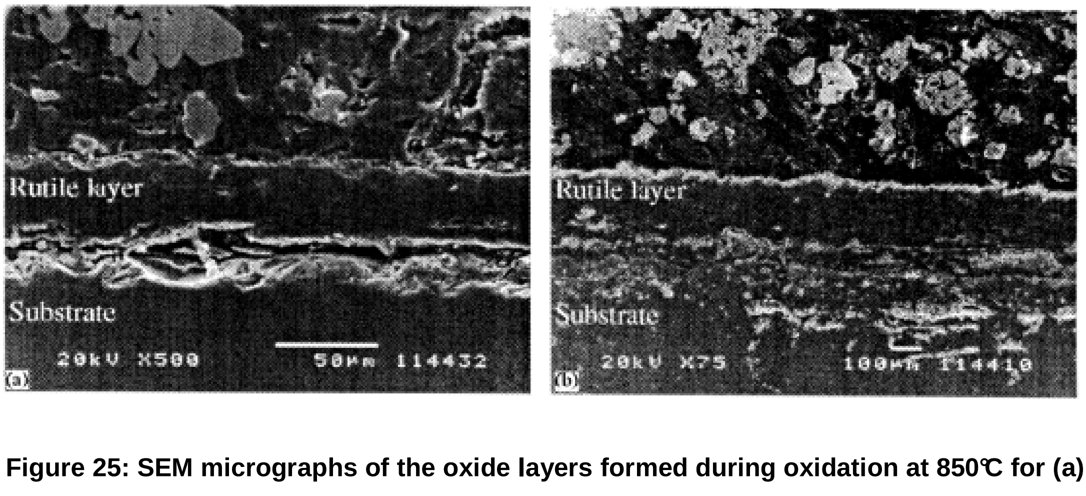

Figure 25: SEM micrographs of the oxide layers formed during oxidation at 850℃ for (a) air cooling and (b) furnace cooling (Siva Rama Krishna et al 2007).

Microhardness and wear tests were performed on the oxidised samples. Microhardness tests at 25gf showed that the furnace cooled specimens produced the greatest increase in surface hardness.

Wear tests were conducted on CSEM type ball on disc tribometer using an alumina ball under the load of 2N and at a speed of 10cm/s for 200m. The plot of the frictional coefficient against sliding distance is shown in Figure 26 (Siva Rama Krishna et al 2007).

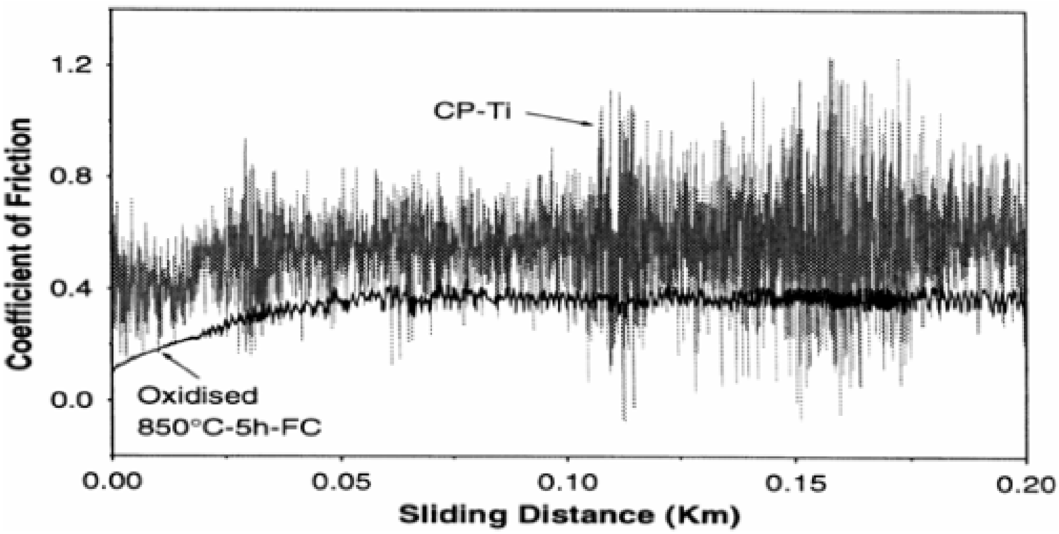

Figure 26: Plot of frictional coefficient against sliding distance of the untreated CP-Ti sample and the oxidised sample. To be noted is the large decrease in fluctuation in the latter sample.
(Siva Rama Krishna et al 2007).

The high fluctuations of the curve for the CP-Ti are characteristic of poor tribological performance where stick-slip occurs during dry sliding. However, the curve for the oxidised sample shows a lowering of the overall friction coefficient curve as well as less fluctuations. This is characteristic of a ceramic-metal interaction (Siva Rama Krishna et al 2007).

Ti-64 samples exposed to various temperatures in the range 600°to 800℃ for different times, 0.5 to 72hrs, were performed by Guleryuz and Cimenoglu (2009). Part of their investigation showed that there was a dramatic increase in the surface hardness of the samples after oxidation at the different temperatures. The results of the tests are shown in Figure 27.

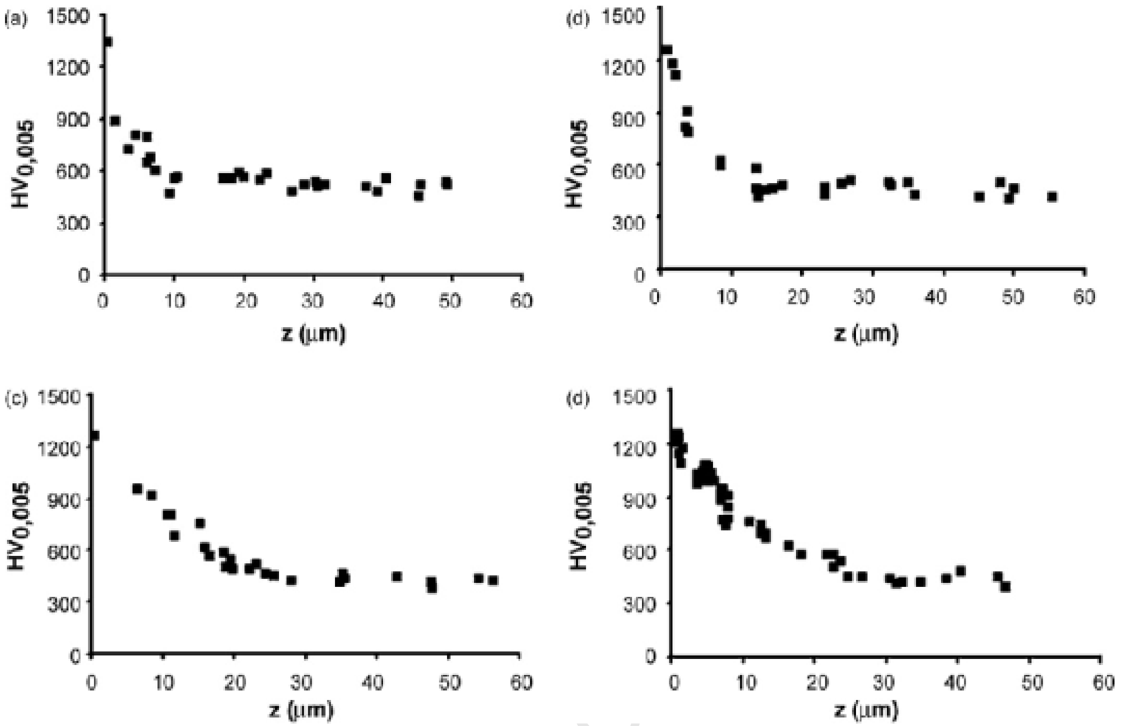

Figure 27: Hardness(Hv) vs Depth(μm) for the samples oxidised at (a) 600℃ for 60hr, (b) 600℃ for 72hr, (c) 650℃ for 60hr and (d) 650℃ for 72hr (Guleryuz and Cimenoglu 2009).

As can be seen from the above graphs there is a gradual decrease in hardness from the surface until approximately 30μm below the surface where the hardness reaches the bulk hardness value. The gradual decrease in hardness can be attributed to the diffusion of oxygen into the crystal structure of the metal causing a hardened case of α-Ti to be formed beneath the surface; the α-Ti is stabilised by the oxygen. The decreasing oxygen concentration across the diffusion zone causes the slow change to bulk hardness (Guleryuz and Cimenoglu 2009).

4.2 Oxygen boost diffusion

This method produces a hardened α-Ti case below the surface by diffusing oxygen into the titanium sample (Dong and Li 2000). As discussed earlier, oxygen is an α-phase stabiliser and the increased concentration of oxygen in the surface favours the formation of the α-phase. Depending on the quantity of the oxygen present it can dramatically lower the amount of β-Ti within the given area (Brooks 1982).

Work conducted by Krol et al (2004) showed that the initial stages of oxygen diffusion takes place within β-Ti and as the oxygen concentration increases a phase change occurs from the β-Ti (O) solid solution to α-Ti (O) solid solution. The solid-state diffusion of the oxygen into the α-Ti causes an irregularity in the structure of the lattice; this irregularity increases the hardness by impeding dislocation motion. However a drawback of this hardening process is a loss in ductility in this region. For high concentrations of oxygen in this region the oxygen diffusion zone (ODZ) can become very brittle and thus a lowering of fatigue resistance occurs (Guleryuz and Cimenoglu 2009). Although the process of thermal oxidation is employed to produce a thick adherent oxide layer it also produces an ODZ beneath the oxide/substrate interface shown by Guleryuz and Cimenoglu (2009). The depth of the affected area is shown by Figure 28.

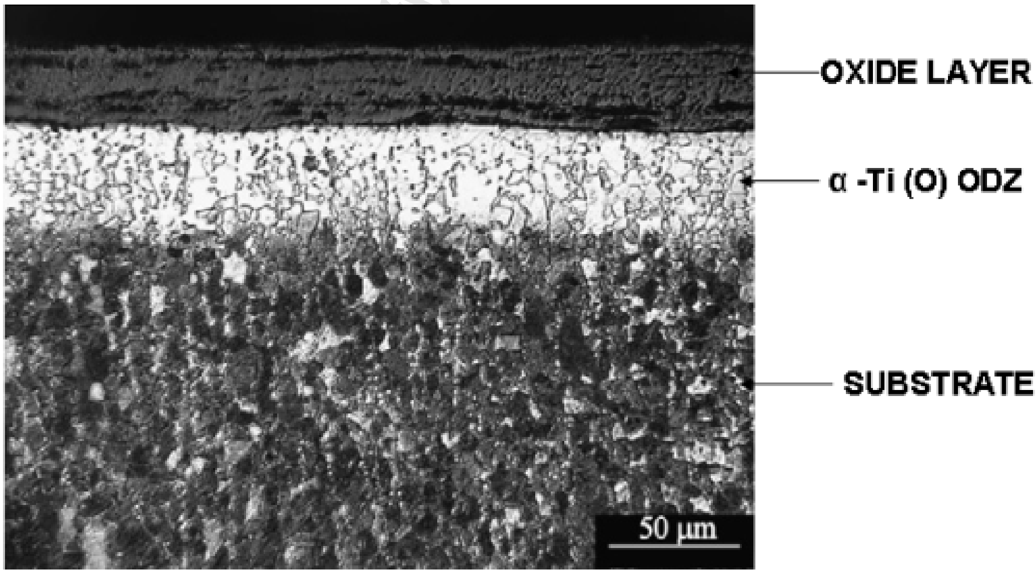

Figure 28: Light micrograph of the 800℃ treatment for 6hrs showing the various areas of the cross-section (Guleryuz and Cimenoglu 2009).

Figure 28 is a light micrograph of a treatment performed by Guleryuz and Cimenoglu (2009) the oxide layer, α-Ti (O) layer (ODZ) and the underlying substrate, a mixture of α and β phases, are shown and labelled.

4.2.1 The Mechanism of the Boost Diffusion Process

The oxygen boost diffusion hardening (OBDH) process consists of two steps namely an oxidation step and a diffusion step. The first step serves to produce an oxide layer which will act as an oxygen source for the second step.
Zang et al (2007) concluded that the dissociation of oxygen during the boost diffusion process follows the particular mechanisms illustrated in Figure 29.
Zang et al (2007) concluded this based on the experimental evidence showing that the concentration of oxygen through the oxide layer was not of the stoichiometric ratio for TiO_2 and more oxygen deficient oxides were present namely TiO, Ti_2O_3 and Ti_4O_7. Thus the relationship between O and Ti in the oxide would best be represented by Ti_aO_b where $a > (b/2)$. The formation of these oxygen deficient oxides could possibly be by reaction 1 in Figure 29; however, TiO_2 could also be dissociated by the removal of oxygen as in reaction 2. Both cases produce oxygen which diffuses into the titanium substrate.

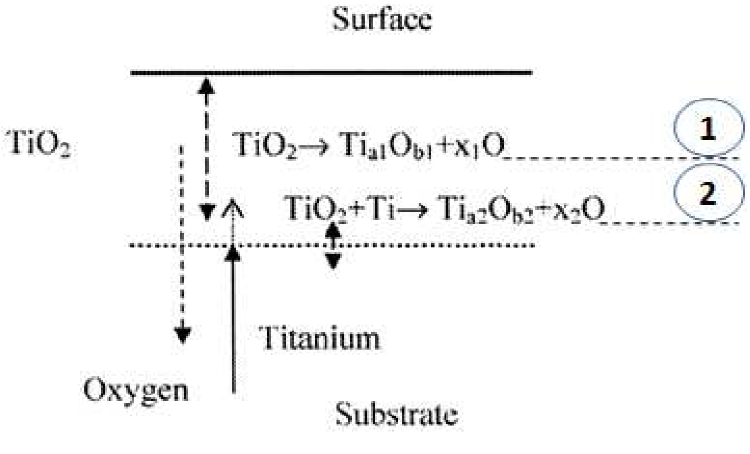

Figure 29: Reactions postulated for the way in which the rutile layer dissociates to liberate oxygen (Zang et al 2007).

Reaction 1 would result in the absorption and diffusion of oxygen into the substrate and as a result no gas is liberated and this would cause no weight loss to occur. However, in the second reaction O could be liberated leading to some measurable weight loss, but mass measurements before and after the boost diffusion process showed that no significant difference occurred. This would imply that the oxide dissociation would occur at the substrate/Oxide interface instead of the Oxide/Air interface.

4.2.2 OBDH as a Surface Modification Technique

Boost diffusion experiments completed by Dong and Li (2000) were successful in providing a boost diffusion process that was able to produce a hardened case to a depth of 300µm. This hardened case depth was produced by pre-oxidizing the samples at 850℃ for 30 minutes for the first step and diffusion treating the samples in the second step for 20 hours in a vacuum at 850℃. Other treatments were also performed and these and the above mentioned parameters are shown in Table 8. Hardness profiles and two-body abrasive wear tests were performed; the latter showed that the above treatment also provided the greatest increase in wear resistance even when compared to the oxidation treatment (A1-Table 8).

Designation	Step I	Step II	Note
A1	30 min	–	Oxidation only
A2	20.5 h	–	Oxidation only
A3	30 min	20 h	Oxide removed before the step II
B1	15 min	20 h	Dense adherent oxide layer
B2	30 min	20 h	Dense adherent oxide layer
B3	45 min	20 h	Partially adherent oxide layer
B4	60 min	–	Crumbly and loose oxide

Table 8: Treatment conditions of the work performed (Dong and Li 2000).

Work performed by Streicher et al (1991) showed that the boost diffusion technique greatly increases the tribological properties of titanium alloys.

Titanium has been used as joint replacements as early as the 1960's. However, once the passive TiO_2 film has worn away the underlying substrate material undergoes excessive wear via the process of three body abrasion. This is due to the worn off oxide particles occurring between the articulating sections. The research performed by Streicher et al (1991) employed various surface modification techniques to characterise the performance of these techniques under different conditions of corrosion, fatigue and wear.

The material used was an alpha beta titanium alloy, Ti-6Al-7Nb. Three surface modification techniques were employed. The first was physical vapour deposition (PVD) of a 3µm layer of TiN. The second was ion implantation of N^+ ions into the titanium substrate. This involved exciting the N^+ ions in an electric field to energies of 35 to 160eV which penetrated the titanium surface causing lattice deformation. The third method was the oxygen boost diffusion hardening (OBDH) process. Two separate wear tests were performed on a pin on disk arrangement with the pins constructed out of medical grade ultrahigh-molecular-weight polyethylene (UHMWPE) and abrasive tests using pins constructed from acrylic cement containing ZrO_2. Test conditions included a constant pressure of 3.45MPa at a sliding velocity of $0.025 m.s^{-1}$. The testing environment was a mixture of Ringer’s solution and 30% calf serum stabilised at a pH of 7,2. The solution was used to simulate biological conditions. Titanium counter-faces were machined into 50mm diameter cylindrical discs with a height of 8mm. The surface hardness and tribological tests showed that although the OBDH method only provided a maximum hardness of 900HV as opposed to the 2200HV obtained by the PVD method it provided the greatest improvement of wear resistance, showing the lowest wear rate, lowest friction coefficient and showed impressive performance in the abrasive test. Only a depth of 1µm was achieved for the abrasive groove after 900hr exposure time as opposed to the 10 hour lifespan of the N^+ treated sample layer.

Friction coefficients and wear mechanisms were evaluated between oxygen diffusion hardened titanium (pin) and a cobalt alloy (counter-face) with reference to the mated pair of grade 1 Ti (Krol et al 2004) also known as CP-Ti. Figure 30 shows the friction coefficient plots for the Ti/Co pair and the Ti (O)/Co pair. The relatively low coefficient of friction was expected for the reference pair showing an initial increase and then drop and stabilization in the steady state zone. The coefficient of friction for the Ti (O)/Co pair showed the mean µ value was reached almost immediately after the test was started but high fluctuations occurred throughout the test. This was attributed to three body abrasive wear occurring due to oxide particles between the two mated surfaces. Three body abrasion is illustrated in figure 29 (Long & Rack 1998). The coefficient of friction values for the various tests both treated and untreated are relatively similar and the entire range is between 0.32-0.35.

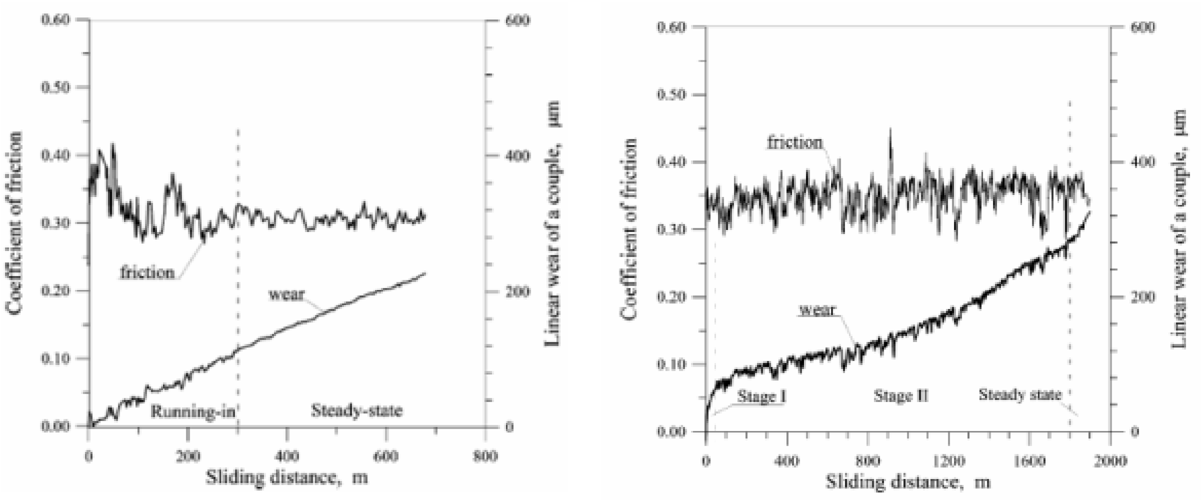

(a) (b)

Figure 30: Friction coefficient and linear wear plots for (a) Ti/Co-alloy couple and (b) Ti (O)/Co-alloy couple (Krol et al 2004).

Analysis of the wear scars by SEM analysis showed that for the Ti/Co couple transfers from both surfaces to the adjacent surface occurred via the processes of adhesion and plastic flow. Due to high flash temperatures; measured during testing at the pin contact area; transferred Ti exhibited thin films of rutile (TiO_2) at the surface. Another wear mechanism found involved the scraping of the accumulated transfers along the wear track by the front end of the pin. Figure 32 is an example of the transfer of Ti to the Co surface; rutile is also marked.

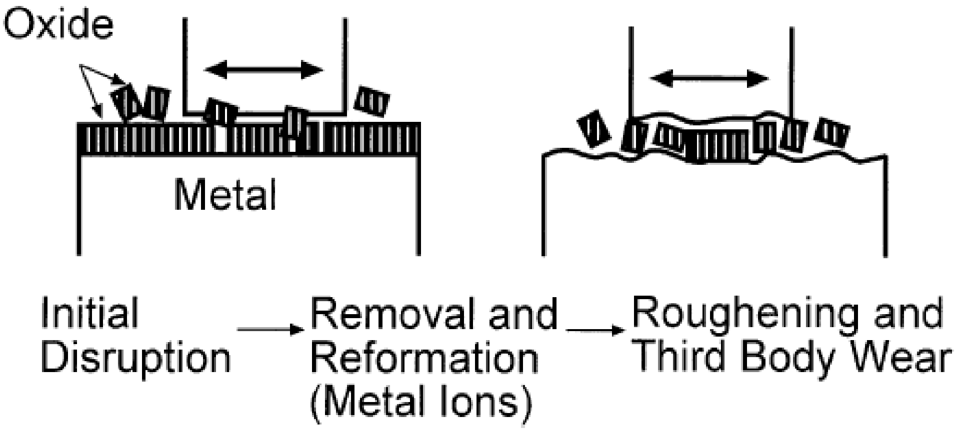

Figure 31: Diagrammatic representation of three body abrasion between an oxide and a metal (Long & Rack 1998).

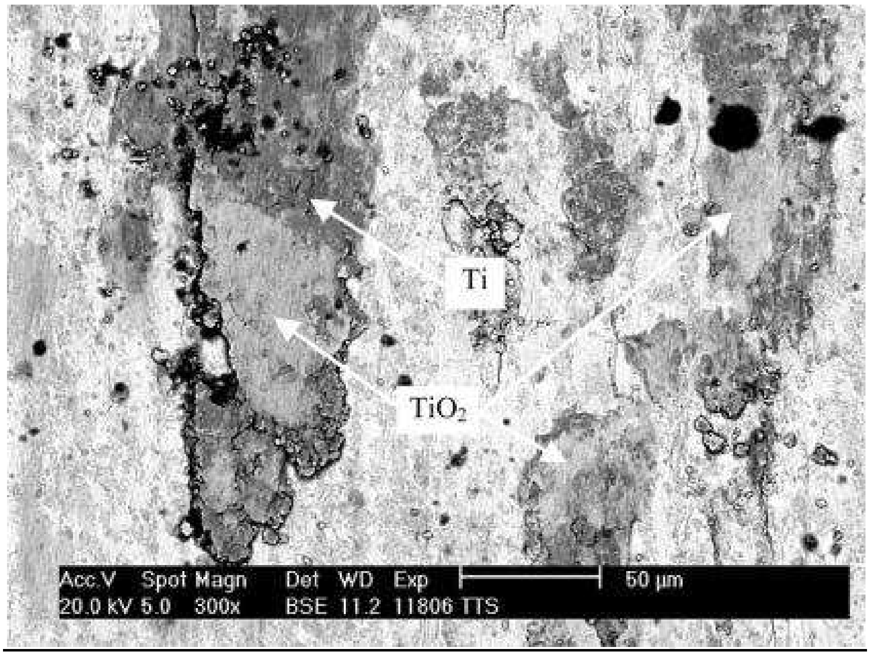

Figure 32: SEM micrograph of the wear surface of the Co-alloy specimen showing flattened transfers of Ti and the surface rutile layer (Krol et al 2004).

As shown in Figure 30 (b), the modified Ti (O)/Co-alloy pair has three distinct phases throughout the length of the test. Stage I shows high linear wear, up to 6 times that for the reference pair, are seen for the first 200m. This can be attributed to the crushing of the brittle Ti (O) layer by high normal stresses and strong adhesion at asperity contacts. SEM analysis of the worn surface of the Ti (O) pin showed micro-cracking at and below the surface of the Ti (O) pin and the hard Ti (O) particles caused ploughing and micro-cutting in the surface of the softer Co-alloy counter-specimen. During stage II (up to 1800m of sliding) the modified Ti (O) layer is completely pulverised into the smaller Ti (O) particles, with three body abrasion causing micro-cutting and ploughing in both the softer Co-alloy surface as well as exposed unaffected Ti (shown in Figure 33 a and b). Nearing the end of stage II the hardness of the Ti (O) particles decreases due to the fact that older abrasive Ti (O) particles are being replaced by newer ones from deeper within the affected Ti zone. This decrease in hardness is attributed to the decreasing gradient of solid solution oxygen within the Ti. On the onset of Stage III (steady state) there is a complete removal of the affected Ti (O) zone and now the mated pair is that of Ti/Co-alloy exhibiting the same wear mechanisms as seen in the original reference couple.

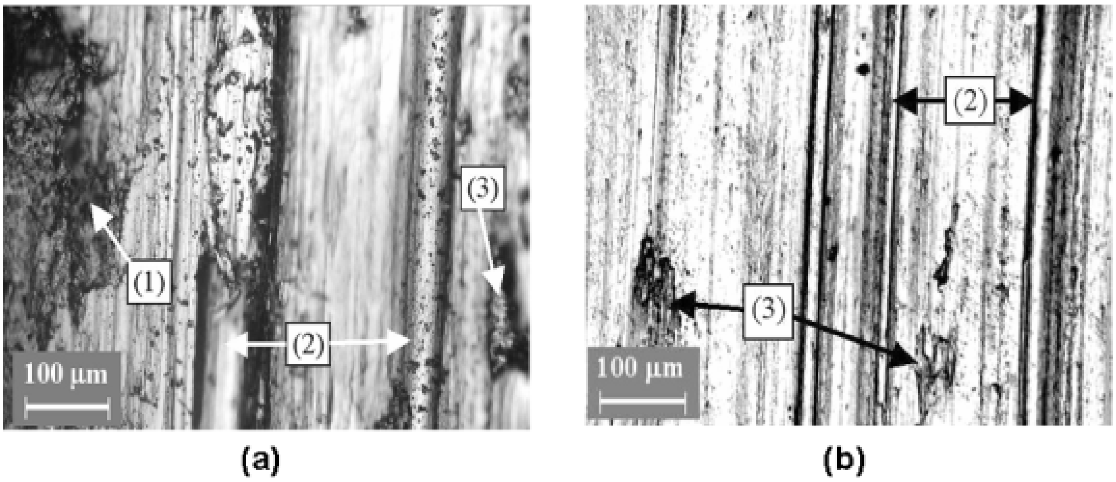

Figure 33: Optical micrographs of the two surfaces of the Ti (O)/Co pair. (a) Surface of the Ti (O) pin showing (1) Ti (O) layer, (2) abrasive grooves and (3) hard Ti (O) particles (b) Co-alloy surface showing (2) abrasive grooves and (3) embedded Ti (O) particle (Krol et al 2004).

Key points to note:

- The continuous Ti (O) layer had a short lifespan due to its low resistance to brittle fracture caused by high normal loads and high adhesive forces during ploughing into the softer Co-alloy surface.
- The embedded Ti (O) particles within both surfaces acted as raised areas which had the capability of carrying higher loads and effectively increased the wear resistance of the mated pair.
- Although the Ti (O) layer broke down during the test, the Ti (O)/Co-alloy pair still showed lower amounts of linear wear. This is shown in Figure 30, as after 700m the Ti/Co-alloy pair exhibits a linear wear of 230µm while that for the Ti (O)/Co-alloy pair amounted to 140µm.
- In both cases the wear mechanisms involved adhesive and abrasive processes.

The two step boost diffusion process has shown the ability to greatly improve the wear performance of titanium alloys, due to the fact that the increased hardness of the diffusion zone reduces the penetration of abrasives. A side effect of the increased hardness is a loss of ductility and fatigue resistance but experimental work has shown that through the process of shot peening the fatigue limit of the treated samples can be completely restored (Dong & Li 2000).

5 EXPERIMENTAL PROCEDURE

The scope of this work is to assess the relative wear performance of the different treatments for the Ti-64 alloy. As titanium has excellent mechanical properties but exhibits very low resistance to wear, surface modification techniques are employed to improve on the latter condition.

For the purpose of this work Ti-64 samples were subjected to various heat treatments in an attempt to improve the wear resistance of the samples. Oxidation treatments as well as the OBDH method have been used to increase the surface hardness of the alloy in attempt to lower the rate of wear experienced for the treated samples.

Optical and SEM imaging were used to evaluate wear mechanisms and to further investigate the effects of the treatments on the microstructure of the samples. This was coupled with cross-sectional hardness to assess the level of penetration of oxygen into the metal substrate.

Once treated the samples are subjected to linear reciprocating tests to evaluate the amount of material removed and to compare the results between treatment conditions in an attempt to conclude the effectiveness of the treatments. Friction data for the different samples were also evaluated to conclude whether any relationship existed (for these parameters) between the coefficient of friction and the relative wear performance of the different treatments. Separate tests were conducted on a pin-on-disk tribometer to compare volume measurements and frictional data to that obtained from the linear reciprocating rig.

The following outcomes are expected:

1. The OBDH and the oxidation treatments will increase the surface hardness of the alloy,
2. The OBDH method will allow for sufficient diffusion of oxygen into the metal substrate to allow a deep hardened case of α-phase Ti to form,
3. The samples with higher surface hardness will exhibit lower wear volumes and thus wear rates. This is based on the Archard equation that volume loss is inversely proportional to the hardness of the softer material,
4. The coefficient of friction will provide limited insight into the variation of wear mechanisms between the different samples however; no conclusions on the wear performance will be evident from this data.

5.1 Materials used

5.1.1 Ti-6Al-4V samples (Counter-face)

Ti-6Al-4V sample material was sourced from Goodfellow Cambridge Ltd and was supplied in 5mm plate and 25mm Ø rod, both in the annealed condition. The plate was used to produce samples for the linear reciprocating rig, with the sample dimensions being 55X12X5mm. The rod was used to produce samples for the tribometer. The rod was sectioned to produce 7mm thick samples.

5.1.2 Steel balls (Wear pins)

Steel balls were used in two sizes, 8mm and 6mm Ø; these were used for the linear reciprocating wear rig and the tribometer respectively. The steel balls were of the material AISI 52100 and were chosen for their relatively high hardness compared to Ti-6Al-4V. The balls had a hardness rating of 750HV (62HRC). The steel balls were kept in a film of bearing oil to prevent rusting and were only cleaned when ready to be used for testing.

5.2 Sample preparation

5.2.1 *Surface preparation for heat treatment*

The sample preparation discussed pertains to both sets of samples used for either wear rig. Prior to any heat treatments the samples were firstly ground using SiC grinding paper of decreasing roughness from 500grit, 800grit, 1000grit, 1200grit to 4000grit. This lowered the surface roughness from an as-machined condition with a R_a value of 0.35±0.05µm to a R_a value of 0.07±0.03µm.

Samples were then cleaned with washing liquid and cotton wool to remove grit and grease followed by hot air drying. The samples were then ultrasonically cleaned in acetone for 2 minutes and dried under hot air; final cleaning involved ultrasonically soaking the sample in methanol for 2 minutes and then hot air drying. During the entire process gloves are worn to prevent the contamination of the surface to be treated by finger grease as described in ASTM G115 (2004).

5.2.2 *Heat Treatments*

Various treatments were performed on the untreated Ti-64 samples, all of which are summarized in Table 9 below.

Treatment	**Key**	**Oxidation Temp (ºC)/ Duration (Hrs)**	**Oxidation Environment**	**Diffusion Temp (ºC)/ Duration (Hrs)**	**Diffusion Environment**
Medical Treatment	MT	600 / 20	Air	N/A	N/A
Oxidation	OX	850 / 0.5	Air	N/A	N/A
Oxygen Boost Diffusion Hardening	OBDH	850 / 0.5	99% O_2	850 / 20	10^{-5} mbar Vacuum

Table 9: Conditions for the various treatments tested.

The MT and OX type treatments were carried out in a separate furnace from that of the OBDH samples, treatments were performed at the various temperatures for specific time periods but both were performed in an air environment.

OBDH samples were treated in a vacuum furnace setup which allowed consecutive switching between the oxidation and diffusion step to occur at temperature i.e. without the need to lower to room temperature. The oxidation portion was carried in an environment of O_2 (99%pure). This oxidation consisted of a 2 step process of allowing oxygen to flow through the sample chamber for 1min and then a soak period for 9min at atmospheric pressure. This flow/soak oxidation also called a pulsed oxidation was repeated 2 more times to produce an oxidation time of 30minutes. Diffusion was carried out in a vacuum at $4x10^{-5}$ mbar for 20 hours; this allows sufficient time for the oxygen to diffuse from the adherent oxide layer into the substrate.

5.2.3 Surface preparation for wear testing

After heat treatment, the MT and OX samples were manually polished using a 0.25µm ø20cm MD-NAP polishing pad and 0.25µm diamond paste with a DP-blue lubricating solution supplied by Struers. At a rotation of 300rpm and under a pressure of ca 0.07Mpa for the given area (55x12x5mm) the samples were successfully polished down to a roughness of 0.15±3µm within 20 seconds and 60 seconds for the MT and OX samples respectively.

A different procedure was used for the untreated and OBDH samples. These samples were surface ground to achieve the 0.15µm R_a roughness value. OBDH samples were surface ground to a specific depth of 50µm as it was experimentally determined that 40µm was the minimum depth to achieve a consistent metallic surface for the treated samples. Once hand polished or surface ground to the required R_a value of 0.15µm the samples were successfully prepared for wear testing.

5.3 Linear reciprocating wear rig

5.3.1 Overview

All wear tests performed in the Centre for Materials Engineering were carried out on the linear reciprocating wear rig, Figure 34. The rig allows for a stroke length of 50mm so that one full cycle measures 100mm. The velocity profile is sinusoidal. Frictional measurements are captured by means of a load cell as a microvolt output and are subsequently amplified before being captured as frictional data.

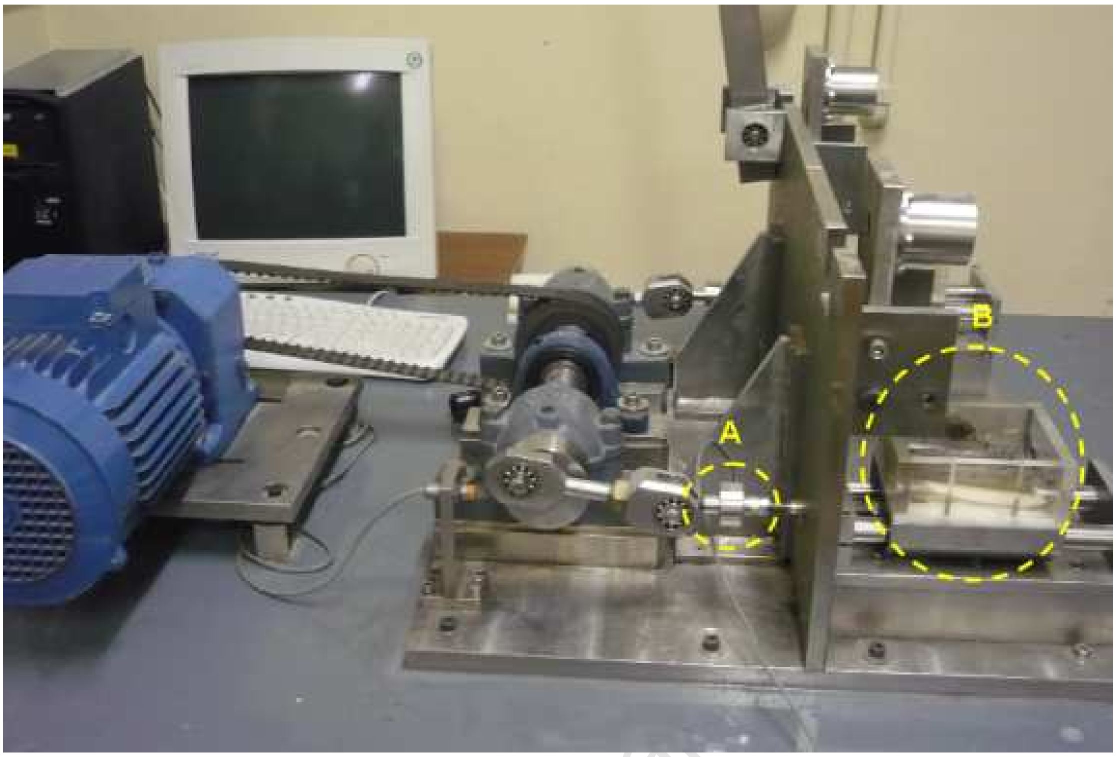

Figure 34: The linear reciprocating wear rig. "A" indicates the load cell and "B" is the reciprocating shuttle where the sample is placed.

5.3.2 Wear testing parameters

Wear tests were performed under a normal load of 5N, which included the mass of the steel ball holder arrangement, the steel ball and a weight of 300g. Distances for testing included 100, 200, 300, 400, 500, 600, 800, 1000, 1200, 1600, 2000 and 2400m; this applies to all samples. Wear tests were carried out at a speed of 0.05m.s^{-1} through a stroke length of 50mm (half-cycle) at room temperature with no lubrication.

5.3.3 Frictional force data capture

Frictional forces experienced between each sample/ball pair is measured by the load cell connected to the shuttle via a shaft. The load cell was calibrated with predetermined weights to produce an output that characterises the force being experienced by outputting a specific voltage. The voltages acquired during testing correspond to specific sample data points which are stored as an excel spreadsheet. Software converts these voltage (mV)/sample data pairs to force (N)/distance (m) measurements using the sample rate, reciprocating speed and load cell calibration. A magnified output of the friction against distance plot for a wear test is shown in Figure 35.

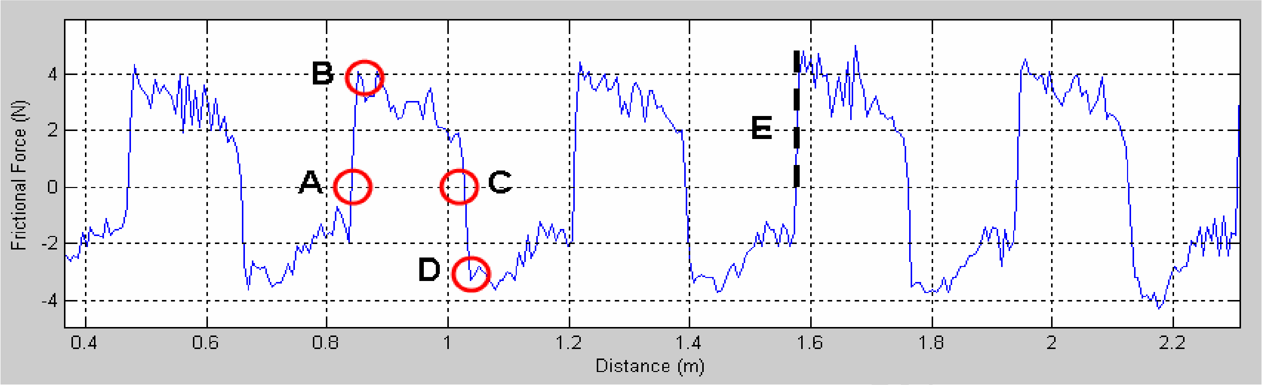

Figure 35: Frictional output obtained from a wear test highlighting key points on the plot.

From the plot in Figure 35 frictional coefficient data can be extracted; this is performed using a separate Matlab program (the Matlab code is provided in the appendix). Friction during reciprocating motion follows a sinusoidal plot; the static frictional force (μ_s) is what is used to calculate the static frictional coefficient. In Figure 35 point “A” corresponds to the start of motion from rest. Initially a large amount of force (B); relative to the normal load; is required to initiate motion. Once motion has begun a smaller force is required to maintain motion and a maximum velocity is reached. Upon nearing the second rest phase there is a deceleration in the shuttle. Point “C” is the second rest phase i.e. the initiation point for the reverse portion of the reciprocating cycle. Each reciprocating cycle in the wear tests performed allows the shuttle to traverse a distance of 100mm, thus a half cycle (point “A” to point “C”) is a 50mm distance. Point “D” represents the frictional force required to initiate motion in the reverse direction. As discussed earlier the static frictional coefficient (μ_s) is the ratio between the static frictional force and the normal load applied to the system. The static frictional force for each cycle has the magnitude of “E” and the normal load is predetermined for the wear test. In this manner the μ_s for each cycle can be measured and plotted as a function of distance.

5.4 Pin on Disk tribometer

5.4.1 Overview

Wear tests were also performed on a CSM pin on disk tribometer shown in Figure 36. The tribometer produces a circular wear track on the surface of the specimen under a specific load. The ball holder can accommodate a ball diameter of 6mm and a maximum normal load of 60N. Testing speed can be varied between 0.3-500rpm with a maximum separate setting of 1500rpm. A data capture system involves a computer separate to the machine itself on which the data is captured and stored. Frictional forces are measured by the deceleration of the rotating mandrel when a frictional force is experienced at the contacting surfaces.

The wear tests performed on the tribometer were conducted to provide a comparison to the data obtained using the linear reciprocating wear rig.

Figure 36: Pin on Disk Tribometer at the Materials Department at the University of Witwatersrand.

5.4.2 Wear testing parameters

The tribological test parameters included a testing speed of 0.05m.s^{-1} under two separate loads of 2N and 5N. Distances covered were 400m and 1200m for untreated, oxidised and OBDH samples. A ball diameter of 6mm was used for the AISI 52100 balls as this was the standard size accommodated by the machine. The wear track circumference was fixed at 16mm for all tests. Samples to be tested were polished according to the specifications discussed earlier.

5.4.3 Frictional data capture

The tribometer was set to capture data points at a frequency of 10Hz and store the results in text format to be analysed accordingly. Unlike that for the linear reciprocating rig, the tribometer analysed the change in the dynamic frictional coefficient instead of the static frictional coefficient.

5.5 Profilometry

5.5.1 Overview

After the wear tests were performed profile plots were taken of the surface of the wear tracks to determine the depth of penetration into the sample as well as to assess the level of volume loss that took place during the test.

5.5.2 Calculation of Volume loss of Specimens

5.5.2.1 Volume loss of the ball specimen

As the ball wears, the scar that is generated can either be that of a flat surface or the worn area could have a slight curvature. Methods of analysis performed by Jun Qu et al (2006) proposed a formula whereby analysis of this curved area could be analysed and factored into the calculation for the volume loss of the spherical slider. For the scope of this report that method could not be performed reliably with the equipment available and thus all ball wear volumes are calculated with the assumption that the worn area is entirely flat in nature i.e. a 2D wear scar. The equation for volume loss for a spherical slider with a 2D wear scar (Figure 19 (a) from ASTM G133) was used as the method of analysis:

$$V_p = (\pi h/6)[3D^2/4 + h^2]$$

$$h = R - [R^2 - (D^2/4)]^{1/2}$$

Where:
V_p = Wear volume of a flat ball wear scar,
D = Diameter of the circular wear scar,
R = Original ball radius,
h = Height of material removed.

If the wear scar on the ball specimen is flat but not circular a maximum and minimum measurement is taken and the average of the two will be used as the diameter of the wear scar (*D*).

5.5.2.2 Volume loss of the flat specimen

Figure 37 is an illustration of the condition when the ball has worn into the flat specimen. It is an equatorial plane perpendicular to the sliding motion.

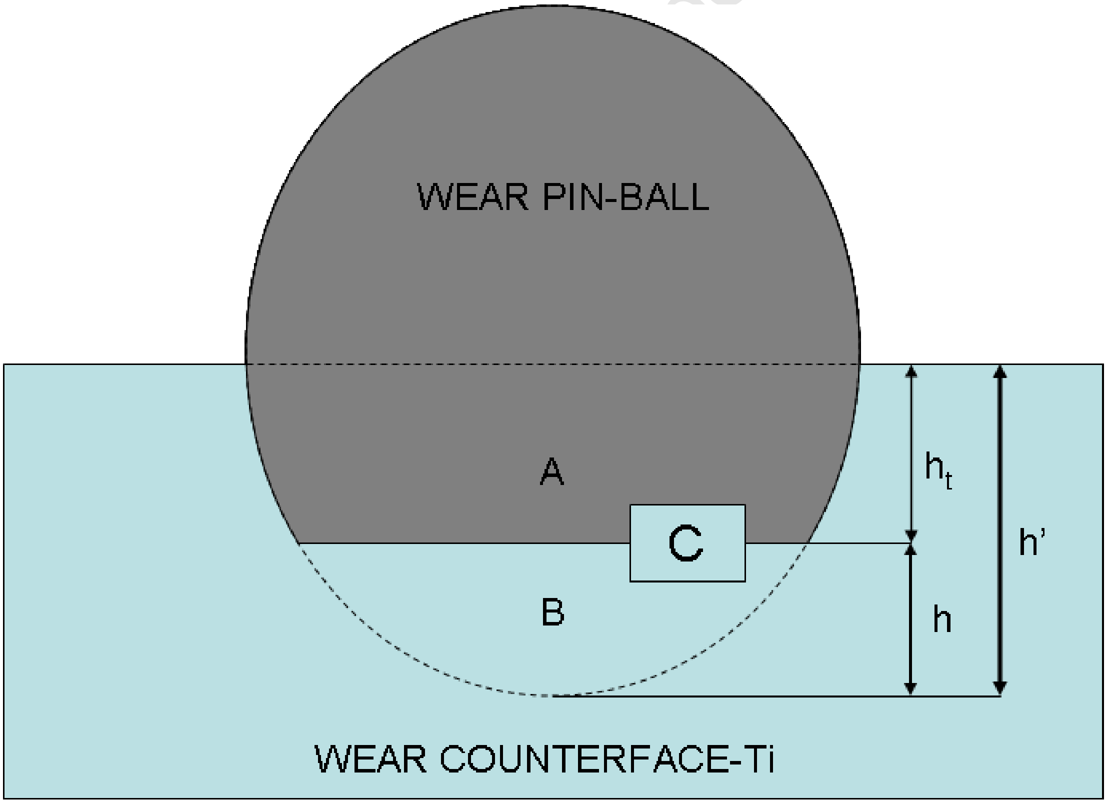

Figure 37: Illustration of the variables used to calculate the volume loss of the flat specimen.

Where:

Area “A” = Area of Ball worn into sample, taking a 2D wear scar for the ball
Area “B” = Area of Ball lost during sliding
Area “C” = Sum of Areas A and B
h_t = Actual height of wear track
h = Ball height lost
h’ = Theoretical height of the wear track if the ball did not wear

Area B and Area C (Figure 37) are calculated using the following relationship between height (h) and the circle radius (R) which is used to calculate the area of the circular segment, the shaded portion of Figure 38.

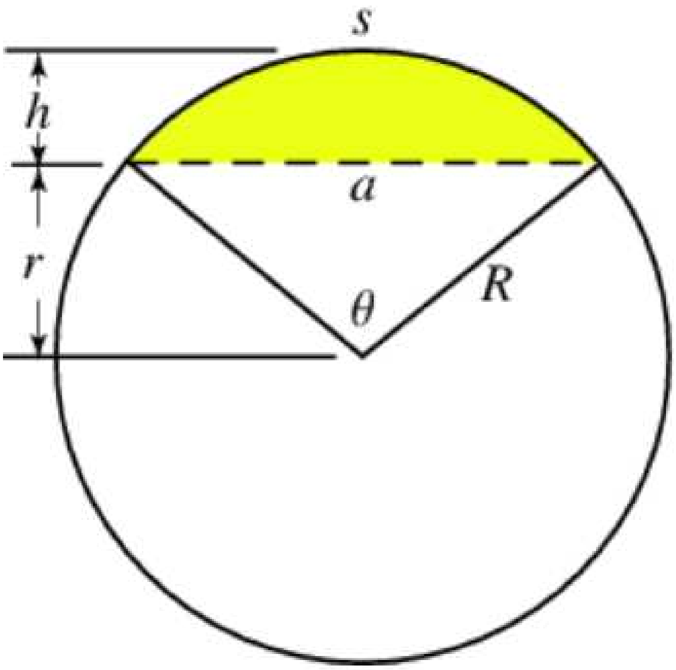

Figure 38: Illustration for the calculation of a circular segment

Relating this to the variables of Figure 37:

$$B = R^2 \cos^{-1}\frac{(R-h)}{R} - (R-h)\sqrt{2Rh-h^2}$$

$$C = R^2 \cos^{-1} \frac{(R - h')}{R} - (R - h')\sqrt{2Rh' - (h')^2}$$

Area A, which is in effect the cross-sectional area of the wear track, is thus the difference between Area C and Area B in Figure 37 i.e.

$$AreaA = AreaC - AreaB$$

The volume loss of the wear track (V) is thus the product of the length of the track (L) and the derived Area A, namely:

$$V = A \times L$$

5.6 Deviation from ASTM G133 – 95

The linear reciprocating wear tests are not in full compliance with the provisions of ASTM G133 (Procedure A) because the pin tip radius used was 8.0mm Ø not 4.76mm Ø, the oscillating frequency was 12Hz not 5Hz, the normal load used in these tests were 5.0N, instead of 25.0N as prescribed by the standard and the stroke length was 50mm instead of 10mm. Ambient conditions including humidity were not measured as it was not expected that these conditions would vary in the laboratory.

6 EXPERIMENTAL RESULTS AND DISCUSSION

6.1 Surface Finish and Microstructure

6.1.1 Introduction

This section deals with the analysis of the features of the various treatments. Changes on the surface occur as variations in the colour and roughness after the different treatments. The micro-structural changes are investigated using light microscopy, SEM and micro-hardness measurements. Micro-hardness measurements were performed under a load of 50gf as this produced indents that could be easily analysed and lower the error during investigation. Analysis of the surface hardness of the treated samples proved to be difficult as the nature of the surface produced disfigured indents which were hard to distinguish from the surrounding area due to the colour change in the sample as well as numerous defects. This was apparent for the OBDH and oxide treated samples. In this case the load was increased to 100gf and indents were measured until a reasonable trend was seen. It is to be noted that although measurements are reported for the surface hardness of the treated samples, this average value cannot be considered as a true reference as the indent itself passes into the layer, measuring material hardness through the surface. When performing the hardness profile analysis, indents were not taken within a distance of 20µm from the surface or any edge as the indents produced were disfigured to such an extent that no reliable measurements could be taken. Table 10 is a key of all the treatment conditions and the respective keys that will be used throughout the text for referral.

Treatment	**Oxidation temp/time**	**Oxidation Condition**	**Cooling**	**Diffusion temp/time**	**Diffision Condition**	**Cooling**	**Key**
Untreated	N/A	N/A	N/A	N/A	N/A	N/A	ASR
OBDH (Oxygen Boost Diffusion Hardening)	850℃/30min	99% O_2	N/A	850℃/20hrs	10^{-5} mbar Vacuum	5℃/min	OBDH
OBDH 50µm (Surface ground at 50µm depth)	850℃/30min	99% O_2	N/A	850℃/20hrs	10^{-5} mbar Vacuum	5℃/min	OBDH[50]
850℃ Oxidation	850℃/30min	Air environment	3℃/min	N/A	N/A	N/A	Ox(850)
600℃ Oxidation (Unpolished)	600℃/20hrs	Air environment Air environment	3℃/min	N/A	N/A	N/A	Ox(600)[U]
600℃ Oxidation (Polished)	600℃/20hrs	Air environment Air environment	3℃/min	N/A	N/A	N/A	Ox(600)[Pol]

Table 10: Key for the various treatments, as well as treatment conditions.

6.1.2 As-Received and OBDH Samples

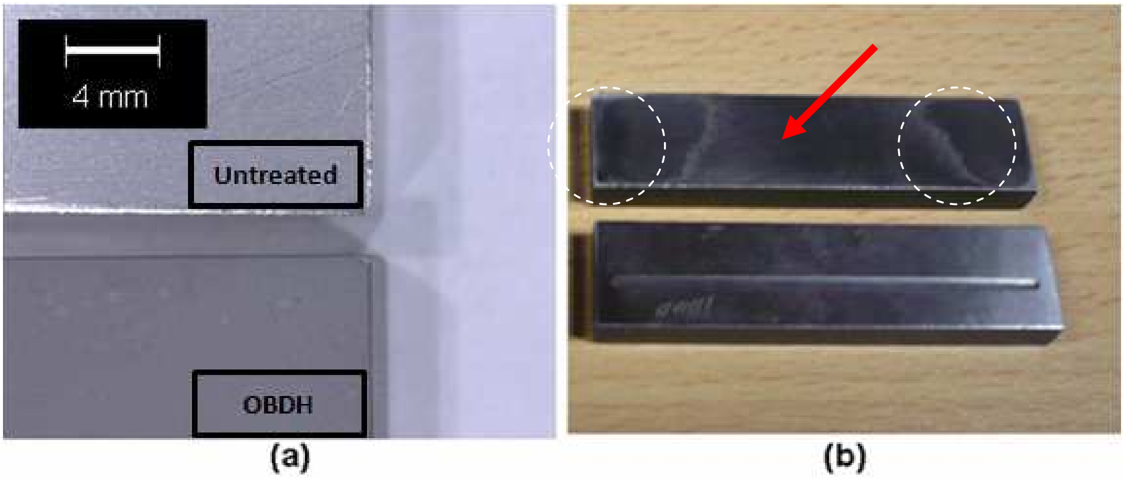

Figure 39: Images showing the (a) change in colour from As-Received to OBDH and (b) an OBDH sample at a 30µm depth (red arrow) showing problem layers (white circles), the lower sample has been machined to a 50µm depth.

Figure 39 shows a comparison between the untreated samples and the OBDH treated samples. As can be seen the OBDH sample before surface grinding has a light blue-grey colour. This is due to oxide scale that remained after the vacuum treatment (the second step of the OBDH process). This scale decreased the surface R_a from 0.59±0.02µm to 0.21±0.01µm. The high roughness of the as-received condition was due to machining lines caused during manufacturing of the titanium plate. The thin oxide film remaining was easily removed by polishing with 0.25µm diamond paste to reveal a dark blue colour beneath. Polishing for 1-2min under a force of 35N was sufficient to completely expose this underlying material. This colour was attributed to the diffusion of oxygen into the metal substrate. Further polishing for another 3min revealed a light brown colour, which persisted until a metallic finish was achieved by grinding. Up to 40µm of the material (from the surface) had to be removed to completely reach a metallic finish. Figure 39 (b) (red arrow) shows a depth of 30µm into the surface, although the majority of the surface had a metallic lustre small light brown areas still remained (white circles). As it was found that 40µm was sufficient to completely achieve a metallic finish, a 50µm depth was chosen as the testing condition. These samples were not ground by hand but had to be machined to this depth to ensure a perfectly flat surface, and a final R_a of approximately 0.15µm with a tolerance of 0.03µm.

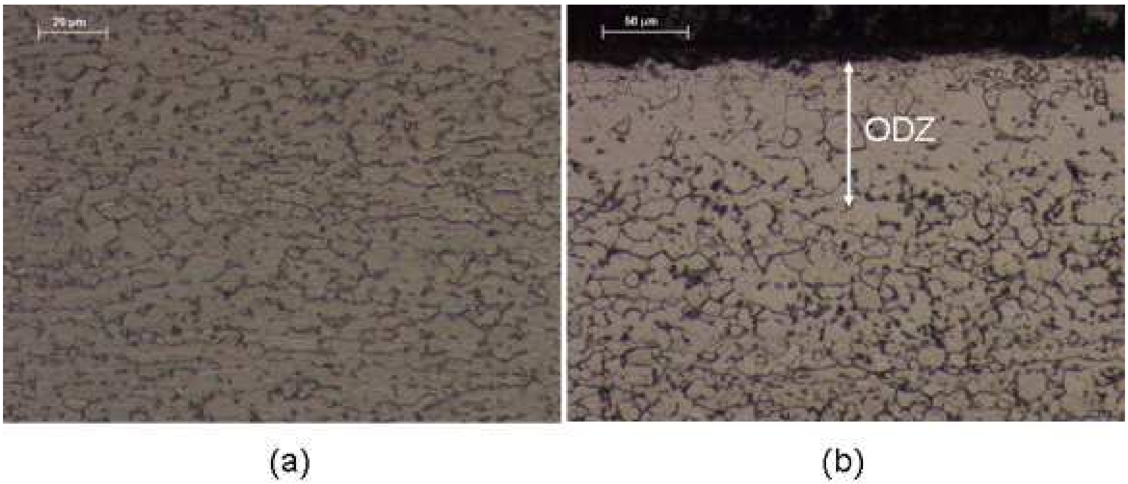

Figure 40: Optical micrographs of the (a) As-received microstructure and (b) the cross-section of the OBDH treated sample showing the hardened Oxygen Diffusion Zone (ODZ).

The untreated microstructure is shown in Figure 40 (a), the larger lighter grains being the h.c.p. α-phase titanium and the darker smaller grains being that of the b.c.c β phase. This is a typical microstructure for Ti-64 in the annealed condition. The stabilised α-phase of the OBDH treated samples can clearly be seen in Figure 40 (b). As was discussed before the α-phase is stabilised by the interstitial diffusion of oxygen into the h.c.p. lattice and is known as the “diffusion zone” or “Oxygen Diffusion Zone (ODZ)”. This stabilized region has α-grains much larger in size than in the untreated condition and due to the diffused oxygen this exhibits greater hardness. This hardness is directly proportional to the oxygen content of the titanium and due to the decreasing gradient of oxygen from the surface into the bulk of the material, a hardness profile is formed. From the light micrograph of the OBDH treated sample in Figure 40 it appears that the ODZ is approximately 80µm in size, however the effects of the diffused oxygen penetrates much deeper.

Figure 41 shows surface cracks that occur in the ODZ of the samples treated with the OBDH method. These cracks originate due to the diffusion of oxygen into the metal matrix which increases the hardness but as a result a loss in ductility occurs and the material in this region becomes embrittled.

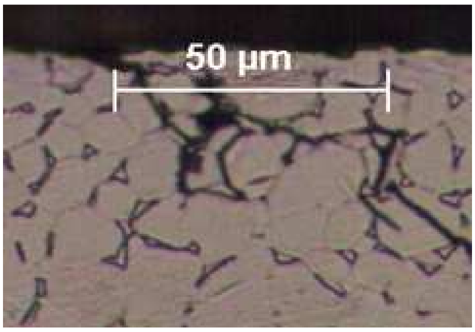

Figure 41: Optical micrograph of the ODZ of an OBDH sample showing cracks beneath the surface.

6.1.3 Air Oxidation Samples

6.1.3.1 Air oxidation at 850℃

Figure 42 shows the Ti-64 samples treated with a single oxidation step at 850℃ for 30min. It is to be noted that the samples were furnace cooled from this temperature and ambient conditions were reached after approximately 6 hours, which corresponds to an average furnace cooling rate of 2.3ºC/min. A dull dark yellow-brown oxide was achieved which was uniform on the surface. The roughness of the oxide formed decreased from the untreated condition to a value of 0.36 ±0.03µm for the R_a value. Furthermore, polishing was needed to drop the R_a value to 0.15µm (tolerance of 0.03µm accepted); this was achieved under a normal load of 35N using 3µm diamond paste for 30sec to 1min. The final polished condition is shown in Figure 42 (lower sample); although retaining a yellow-brown colour in the polished state, the samples obtain a shiny lustre.

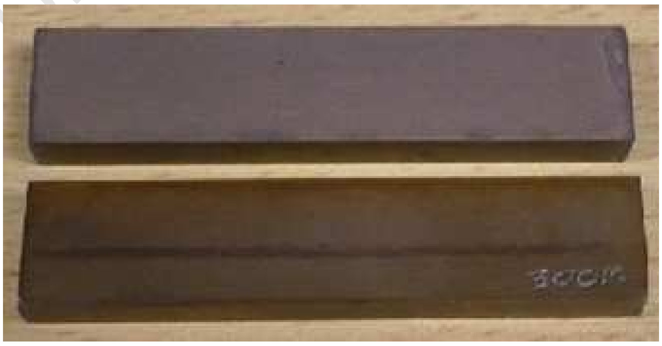

Figure 42: Samples treated at 850℃ showing dark yellow brown oxide, bottom sample has been polished to the testing R_a condition.

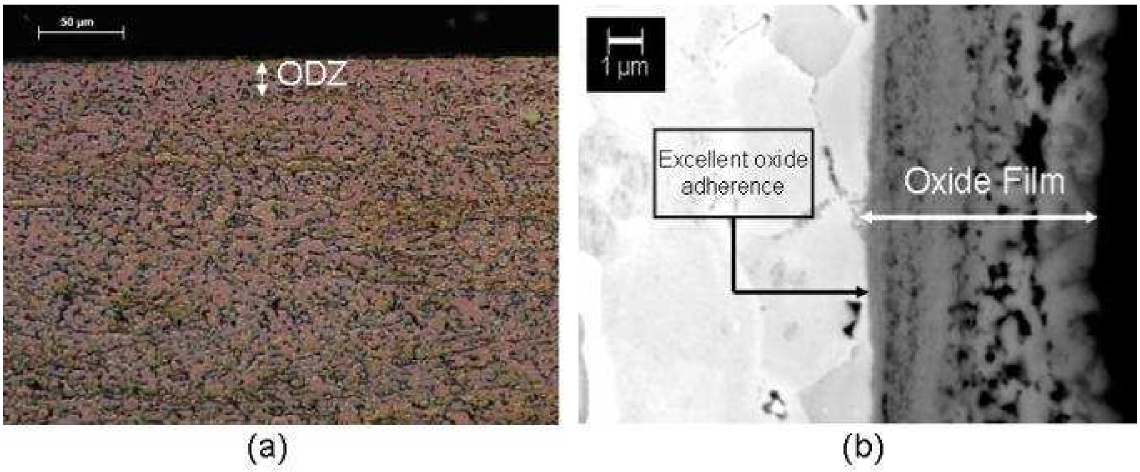

Figure 43: (a) Optical micrograph showing ODZ of the 850℃ oxidation treated samples and (b) secondary SEM image showing the thickness of the oxide layer.

The ODZ generated from the thermal oxidation treatment at 850℃ is considerably smaller than that formed during the OBDH process as can be seen in Figure 43 (a). An oxide layer of approximately 8µm thickness is formed and this is shown in Figure 43 (b). This agrees with the work performed by Siva Rama Krishna et al (2007) which showed that 850ºC was the best temperature to form a thick adherent oxide layer on Cp-Ti. When the samples were soaked at this temperature for a period of 30 minutes and allowed to furnace cool at a rate of 2ºC/min down to ambient conditions, the thickness of the oxide layer developed was approximately 8µm. Their work also showed that by increasing the oxidation soak time it was possible to produce an oxide layer in excess of 140µm thick; this was achieved by a soak time of 5 hours followed by furnace cooling. However, Dong et al (2000) showed that Ti-64 specimens, oxidised at 850℃ for more than 30 minutes in an ai r environment, formed partially adherent oxides. This complements trial treatments that were performed in which Ti-64 samples were oxidised in an air environment for 45 minutes as opposed to 30 minutes. This change in soak time dramatically decreased the adherence of the oxide. Before removing the samples from the furnace the oxide showed a high degree of delamination off the surface. Such a surface oxide layer would provide little protection to the underlying material. Samples prepared at a temperature of 850ºC for a soak time of 30 minutes followed by furnace cooling showed excellent adherence to the metal substrate, as is seen in Figure 43 (b).

This exceptional adherence at the oxide/metal interface is crucial for improving the wear performance as a low adherence to the underlying substrate could lead to delamination of this oxide during wear testing, compromising the protection of the metal. However it is seen that the oxide itself contains many pores, which are formed during the formation of the oxide by alternating layers of Al_2O_3 and TiO_2 as discussed earlier. As these pores are closer to the surface there is a greater risk of delamination wear occurring under the high normal stresses produced by the normal load and hardened steel ball. This would result in segments of the oxide being removed by cracking, either surface or sub-surface propagation, ultimately removing the segment. The exposed titanium substrate would then be susceptible to 3 body abrasion. Wear mechanisms found are discussed more thoroughly in sections to come. Thermal oxidation of titanium samples were performed by Guleryuz and Cimenoglu (2009), and the oxide layer produced showed signs of these subsurface pores to a high degree, as well as low adherence of the oxide to the substrate.

6.1.3.2 Air oxidation at 600℃

After oxidation in an air environment at 600℃ for 20hrs (furnace cooling for 6hrs) a much smoother surface oxide, light yellow-brown in colour, was achieved as shown in Figure 44 (a) (white arrow). The oxide exhibited a R_a value of 0.12µm ±0.02µm; however the oxide film was especially thin. Its thickness could not be determined via light microscopy (Figure 44 (b)) and the attempt to mount and evaluate using SEM imaging showed that the oxide had been fragmented off the metal surface during cooling after hot mounting. This is due to the difference in thermal expansion coefficients between the metal, oxide and the resin.

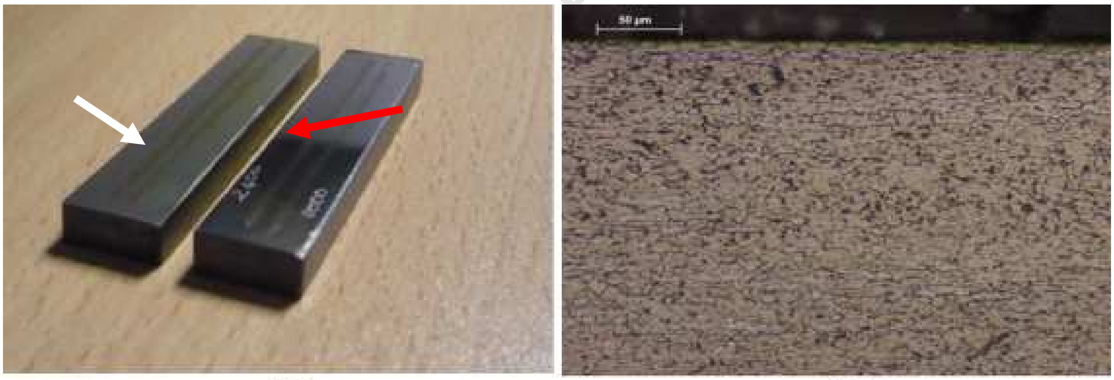

(a) (b)

Figure 44: (a) Samples oxidised at 600℃ for 20 hours, polished condition indicated by red arrow and (b) Optical micrograph showing the cross-section of a 600℃ oxidised sample.

To simulate in service use of oxidised components in the medical industry, separate 600℃ oxidised samples were polished using 0.25µm diamond paste for 1-1.5min under a normal load of approximately 35N to achieve a metallic finish. This further lowered the surface roughness to a R_a value of 0.04µm ±0.02µm. This highly polished state is shown in Figure 44 (a), designated with a red arrow.

It is also seen that the ODZ is not distinguishable from the rest of the microstructure, however oxygen diffusion effects are further investigated using the hardness profile in Figure 45. The research performed by Dong and Bell (2000) showed that an ODZ was present beneath the oxide formed at 600℃ and penetrated into the surface to a depth of 20µm.

6.1.3.3 Pilling-Bedworth Ratio for oxidized samples

When an oxide grows by the inward diffusion of anions the new oxide layers are generated at the oxide/metal interface. As a result the new oxide will be constraint between the previously formed oxide and the metal substrate. This causes growth stress to be generated within the newly formed oxide. As the volume of the new oxide formed is rarely equal to that of the metal consumed, either a compressive or tensile stress will develop within the oxide. These stresses can cause delamination and cracking of the oxide which in turn prevents the oxide from protecting the underlying metal. Tensile stresses are produced when $R < 1$ while compressive stresses arise when $R > 1$. Apart from the compressive and tensile stresses experienced as a result of the mismatch in the volumes of the oxide and the base metal, the difference in the thermal expansion coefficients can also add to low adherence of the oxide to the metal substrate (Xu and Gao 2000).

This section is dedicated to the evaluation of the R value for the Ti-6Al-4V alloy as opposed to that of Cp-Ti. The calculation of the R value will be based on two main assumptions:

1. That the R value may be calculated using TiO_2 (rutile) as the only constituent of the oxide,
2. That the R value may be calculated using the h.c.p. lattice parameters.

During the high temperature oxidation of Ti-64 between 500 - 900ºC, the oxide layer is composed of not only TiO_2 but also Al_2O_3 and V_2O_5. Work conducted by Garbacz and Lewandoska (2003) showed this during the oxidation of Ti-64 and Ti_3Al in this temperature range; the compositional results of the oxides formed are tabulated in Table 11 and were determined by means of X-ray phase analysis and X-ray microanalysis.

Scale	**Ti-64**			**Ti3Al**	
	TiO_2	**Al_2O_3**	**V_2O_5**	**TiO_2**	**Al_2O_3**
1	98.9	n/a	1.1	86.2	13.8
2	98.4	n/a	1.6	76.4	23.6
3	95.7	2.8	1.5	89.5	10.5

Table 11: Composition (%) of the oxide scales formed on the Ti-64 and Ti_3Al alloys Garbacz and Lewandoska (2003).

Oxidation for these samples was carried out at 900ºC in an air environment for 170 hours. As can be seen the majority of the oxide is composed of TiO_2. A separate investigation into the oxidation behaviour of Ti-64 in the range of 600 -700ºC was conducted by Frangini et al (1994). The work performed provided the same insight into the relative amounts of the various oxides formed. As a consequence of this the R value for Ti-64 will be based on an oxide of TiO_2 forming and the oxides Al_2O_3 and V_2O_5 will be ignored.

Two phases are present in the Ti-64 alloy, namely the α-phase (h.c.p.) and the β-phase (b.c.c.) (ed. Donachie 1988). However during high temperature oxidation the inward diffusion of oxygen into the metal lattice stabilises the α-phase, because of this the area below the metal/oxide interface will be primarily α-phase as shown in the present work as well as previous work such as Dong and Li 2000b. For this reason the calculation of the R value for Ti-64 will be based on the h.c.p. lattice parameters.

As discussed earlier, the calculation for R is as follows:

$$R = \frac{Md}{amD} \equiv \frac{V_{mo}}{V_{mc}} \text{ (Zang 2000)}$$

The following reaction occurs during the formation of TiO_2:

$$\text{Ti (IV)}^{4+} + 2O^{2-} = TiO_2 \text{ (Grant 1958)}$$

From the above equation it is evident that 1 mole of Ti produces 1 mole of TiO_2. Thus as 1 mole of Ti is consumed during the production of the oxide, 1 mole of TiO_2 is formed. The volume of 1 mole of both the metal and the oxide is used for the calculation of the R value. Xu and Gao (2000) provide the following equations to calculate the molar volumes of the oxide and the metal/alloy respectively:

$$V_{mo} = \frac{nM}{\rho} \quad \text{and} \quad V_{metal} = \frac{N_a V_{cell}}{n_{cell}}$$

Where:

V_{mo} = Volume of the metal oxide formed (cm^3),

n = Moles of the oxide formed (in this case 1 mole),

ρ = Density of the oxide ($g.cm^{-3}$),

V_{metal} = Volume of the metal consumed (cm^3),

N_a = Avogadro's number (6.023×10^{23})

V_{cell} = Volume of the lattice unit cell (cm^3)

n_{cell} = Number of atoms in the unit cell.

Based on its geometry the volume of the h.c.p. lattice unit cell can be determined by:

$$V_{h.c.p.} = \frac{6}{4} a^2 c \sqrt{3}$$

Where:

$V_{h.c.p.}$ = Volume of the h.c.p. lattice cell

a = lattice parameter (Å);

c = lattice parameter, height of the h.c.p. unit cell (Å).

The information required for the comparison of the R values of Ti with that of Ti-64 is shown in Table 12.

	M (g.mol-1)	**ρ (g.cm-3)**	**a (Å)**	**c (Å)**
TiO_2	79.865(1)	4.28(1)	n/a	n/a
Ti	n/a	n/a	2.95(2)	4.68(2)
Ti-64	n/a	n/a	2.92(3)	4.66(3)

Table 12: Data required to calculate the R values for Ti and Ti-64 ([1] Grant 1958)([2] Donachie 1988)([3] Halevy 2010).

From the equations it was calculated that Ti has an R value of 1.76 which correlates to the value stipulated by Uhlig (1985) of 1.8. The value of R for Ti-64 was calculated as 1.79, relatively identical to that of Ti. It must be emphasised however that this calculated R value for Ti-64 makes two main assumptions, which have been discussed. The purpose of this calculation was to investigate the difference in R values of the two metals taking into account the substitutional elements of Al and V which would alter the unit cell parameters of Ti-64. The value of approximately 1.80 for the R value of Ti-64 should indicate that the oxide formed on the surface is a protective layer. Although this was the case for the current work, separate work has shown that the integrity and adherence of the oxide layer is highly dependant on the oxidation temperature, atmosphere and soak time (Dong and Li 2000a) (Dong and Li 2000b). For example, work performed by Dong and Li (2000a) showed that Ti-64 oxidised at 850ºC for 30 minutes produced a strong adherent oxide layer while continuing the soak time to 45 minutes lead to the oxide delaminating from the metal surface. Tests run during the current work confirmed this outcome. Although the R value cannot be used to predict the protective nature of the oxide it can assist in determining the type of stress that will be experienced in that oxide. As was shown, 1 mole of oxide formed occupies close to double that of the volume of the metal consumed. Due to new oxides forming at the metal/oxide interface (Burnell-Gray et al 1994), high compressive stresses will be experienced in this oxide.

6.2 Hardness profiles for the different treatments

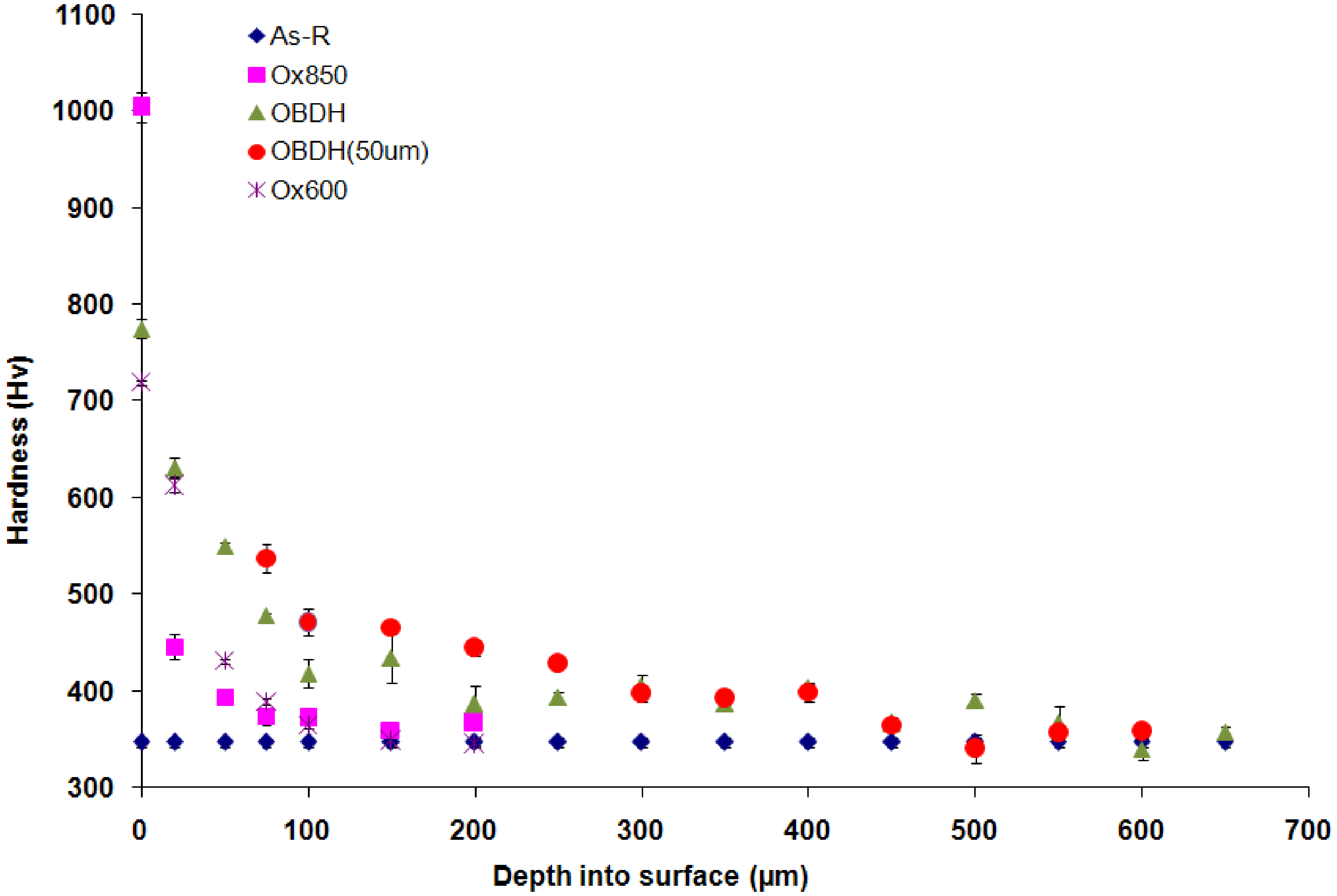

Figure 45: Hardness profile of the various treatments performed including the 50µm section removed from the pulsed samples.

The above graph (Figure 45) shows the micro-hardness profiles for the various treatments. Each point on the curve represents a mean value of 5 readings at a specified depth. The standard deviation is plotted as error bars on each point. Oxidation at 850℃ for 30min produced the greatest increase in hardness from as-received, namely 347.2Hv ±8.9Hv to 1004.0Hv ±31.7Hv. However the penetration depth of the oxygen into the substrate is fairly shallow and bulk hardness is reached after approximately 100µm into the surface, the majority of the strength being lost in the first 20µm. An affected zone of 450µm is achieved with the OBDH method; this is much greater than the observed 80µm thickness of the hardened α case as shown in the optical micrograph of Figure 40 (b). The OBDH treatment produced a surface hardness of 775.4Hv ±19.3Hv, dramatically greater than the untreated condition. However as discussed earlier the OBDH samples are surface ground and polished to a depth of 50µm to achieve a metallic finish. After being surface ground, sample hardness profiles were plotted to compare the similarity to the OBDH standard plot. As it can be seen the plot follows the same trend of decreasing hardness to increasing depth, and the actual hardness when wear tested is 537.5Hv ±21.4Hv. When compared to the other treatments the oxidation at 600℃ for 20hrs performed the weakest in terms of increasing hardness, as the surface hardness increased to 719.6Hv ± 16.3Hv from the untreated condition. The ODZ for this treatment is relatively the same as that achieved by the 850℃ oxidation process, namely 100µm, but is much deeper than the 20 µm observed in the research conducted by Dong and Bell (2000).

Table 13 is the summarised results reported in this section, which covers surface characteristics and micro-structural properties of the various conditions of the Ti-64 specimens.

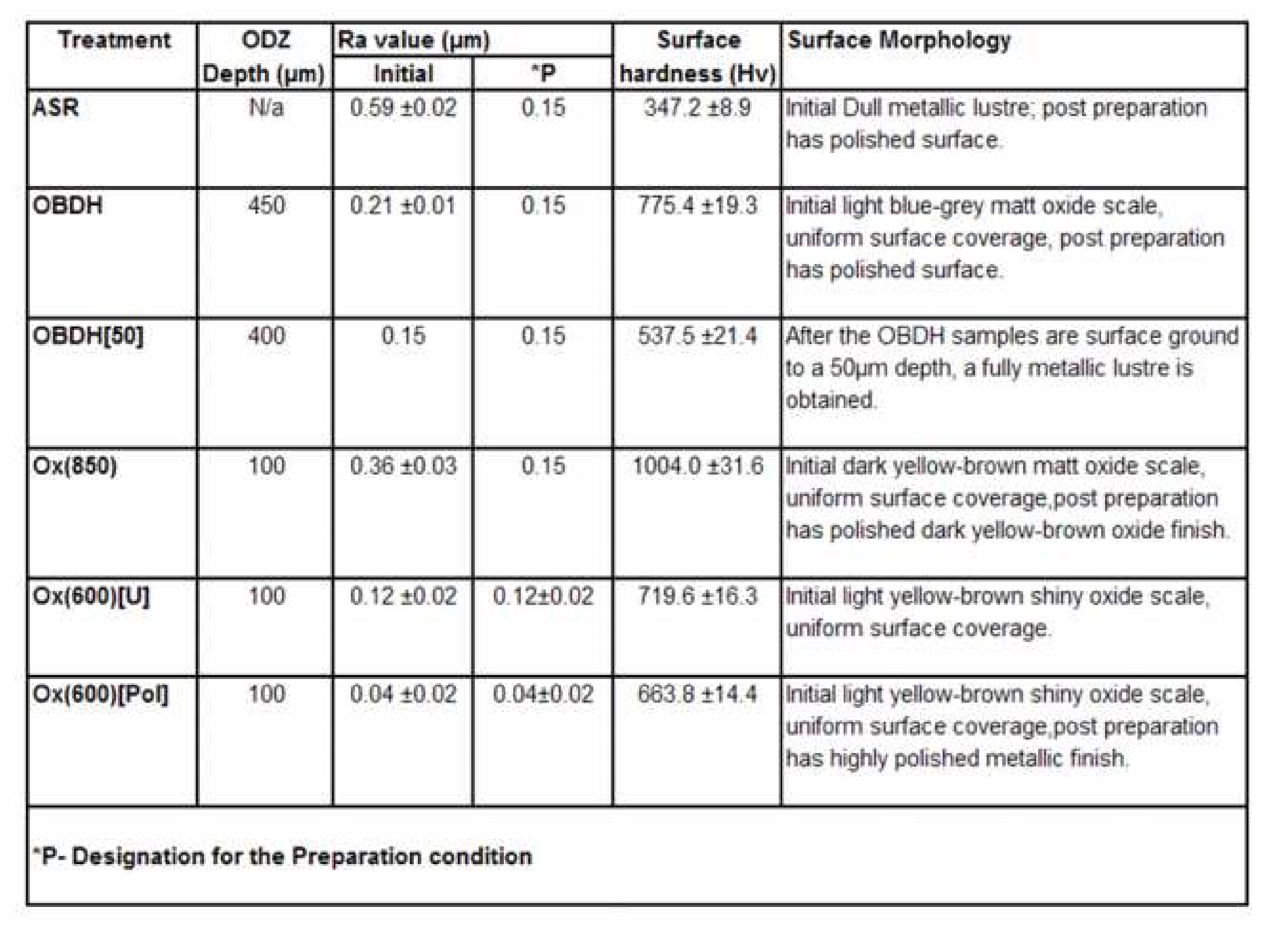

Treatment	ODZ Depth (μm)	Ra value (μm)		Surface hardness (Hv)	Surface Morphology
		Initial	*P		
ASR	N/a	0.59 ±0.02	0.15	347.2 ±8.9	Initial Dull metallic lustre; post preparation has polished surface.
OBDH	450	0.21 ±0.01	0.15	775.4 ±19.3	Initial light blue-grey matt oxide scale, uniform surface coverage, post preparation has polished surface.
OBDH[50]	400	0.15	0.15	537.5 ±21.4	After the OBDH samples are surface ground to a 50μm depth, a fully metallic lustre is obtained.
Ox(850)	100	0.36 ±0.03	0.15	1004.0 ±31.6	Initial dark yellow-brown matt oxide scale, uniform surface coverage,post preparation has polished dark yellow-brown oxide finish.
Ox(600)[U]	100	0.12 ±0.02	0.12±0.02	719.6 ±16.3	Initial light yellow-brown shiny oxide scale, uniform surface coverage.
Ox(600)[Pol]	100	0.04 ±0.02	0.04±0.02	663.8 ±14.4	Initial light yellow-brown shiny oxide scale, uniform surface coverage,post preparation has highly polished metallic finish.

***P- Designation for the Preparation condition**

Table 13: Summary of the results obtained through light microscopy, SEM and micro-hardness measurements.

7 WEAR TEST RESULTS

The results obtained through wear testing are presented in the following subsections. Analysis of the wear performance was categorised by volume loss, frictional coefficient data and the relative wear mechanisms that occurred. A final discussion of the all the results will be presented and conclusions drawn.

Samples were mated against steel balls (wear pins) and worn through specific distances. After the tests the samples were analysed to determine volume loss by profilometry as well as what kind of wear mechanism occurred.

7.1 Volume Loss

The main focus of this section was to evaluate the relative wear performance of the different treatments using volume loss as a function of sliding distance. As discussed in the experimental procedure, the volume loss of the samples was derived from the wear track width of the track and the ball scar diameter. Figure 46 below is an example of a profile that was examined to derive the wear track width. The sample is in the ASR condition and was worn through 2400m on the linear reciprocating rig. The profilometer cannot assess a depth greater than 50µm, and this is clearly seen in the figure below. The track width (red arrow) is measured from these profiles and used in the volume calculation. A total of 5 profiles are taken per track, to derive an average track width.

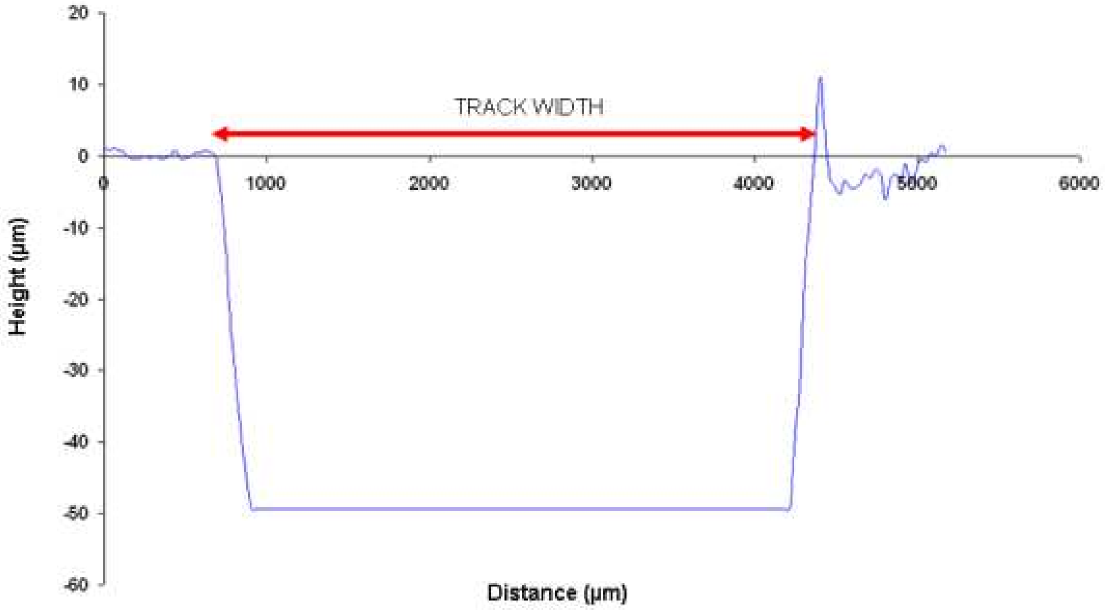

Figure 46: Profile trace across the wear track of an ASR sample, worn though a distance of 2400m.

7.1.1.1 Volume losses of the counter-face and pin specimens

As discussed the volume loss as a function of distance was plotted for each sample and a combination of all these plots is shown in Figure 47. As the pin wear is of importance the volume loss of the steel balls for the corresponding tests were also plotted and are shown in Figure 48. Each point on these graphs (Figure 47 and Figure 48) represents averaged values. The volume loss at each sliding distance interval represents an average of two tests whereas the total volume loss after 2400m is the average of four tests for each respective condition.

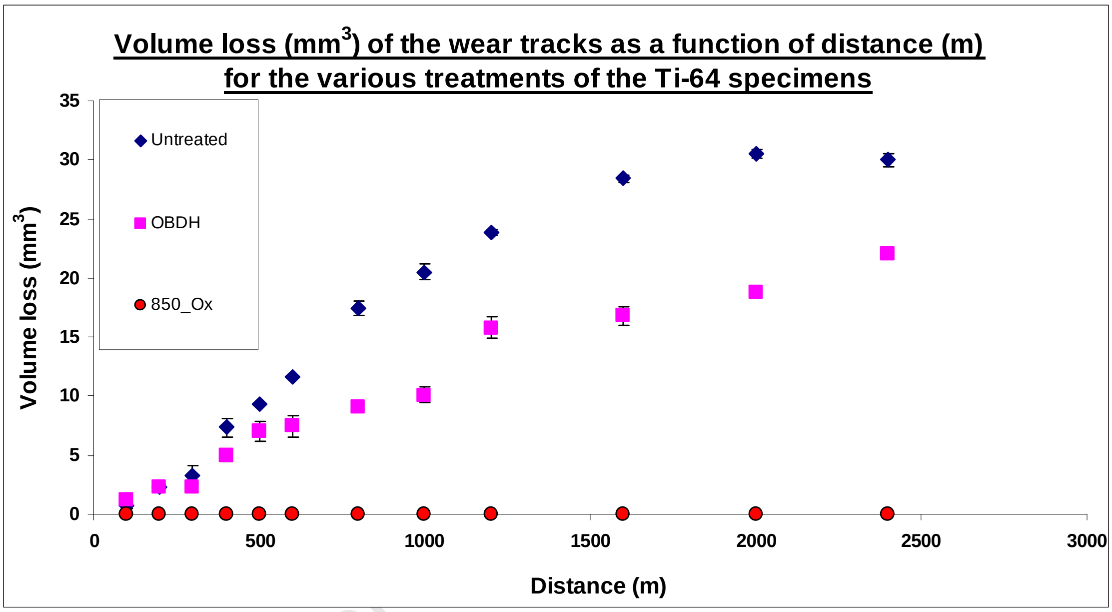

Figure 47: Volume loss of the counter-face Ti-64 samples as a function of distance, for the various treatments.

From Figure 47 above it is clear that the greatest wear loss occurred for the untreated condition of the Ti-64 samples. Initially the untreated and OBDH samples showed similar volume losses and this occurred up to a distance of 300m, after which a clear distinction occurs as the tests progress. OBDH treated samples however showed a final reduction in volume loss of 25% when compared to the untreated samples for 2400m. Profiles taken across the wear tracks of the oxidised samples showed no distinct track width or depth, and thus no volume loss for these samples could be determined. For comparative purposes these results were plotted on the same axis as the ASR and OBDH specimens. Similarly no measurable wear track could be determined for the samples of both 600℃ oxidation treatments, these results were not included. A comparison of the steel ball volume loss is shown in Figure 48.

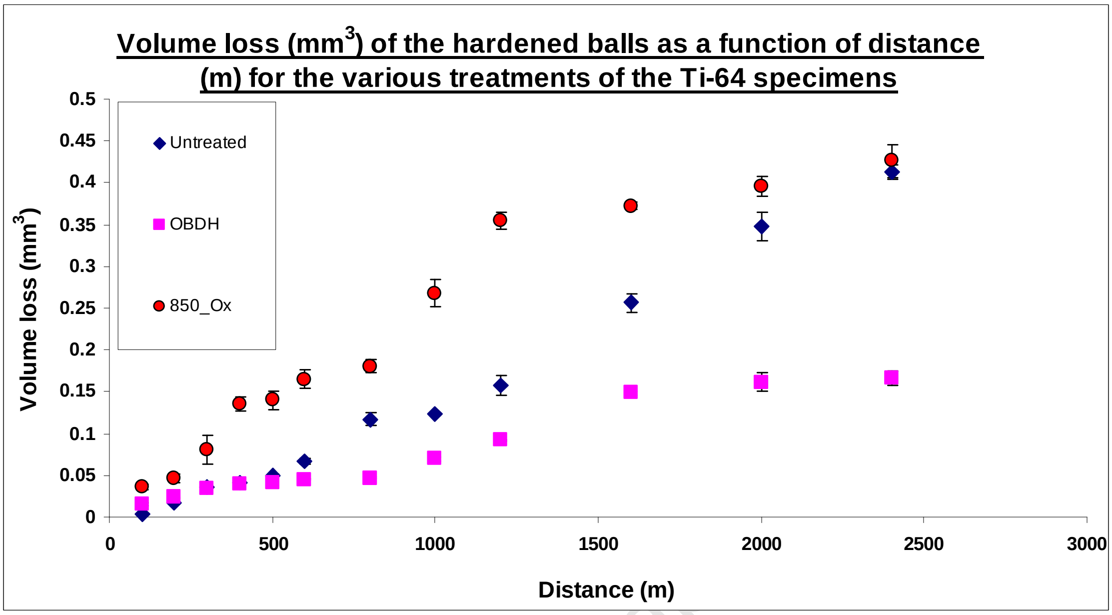

Figure 48: Volume loss of the steel balls as a function of distance, for the various treatments.

The greatest volume loss relating to the steel balls occurred for the tests where the balls were worn against the samples oxidised at 850ºC and the untreated samples. Although showing much greater volume losses than the oxide samples the OBDH tests generated the lowest volume loss of the steel balls after 2400m.

Figure 49 and Figure 50 provide the wear rates of the samples as a function of surface hardness. In the former figure the total specific wear rates (ball + Ti alloy) are shown, the wear rates are calculated based on the Archard wear equation (a) shown below:

$V = K\frac{W}{H}S$ (ed. Hutchings 1997) (a)

Where:

V = Wear volume

K = Wear coefficient

W = Normal load applied to the system

H = Hardness of the softer material of the mated surfaces

S = Sliding distance

Where “V” is reported in $m^3.m^{-1}$ the other units are reported as the standard SI units for the relative property i.e. Pascals (Pa) for “H”, meters (m) for “S” and Newtons (N) for “W” (Podra and Anderson 1997). Thus the above equation can be rearranged to determine the wear rate ($m^3.m^{-1}.N^{-1}$) illustrated as equation (b):

$$\frac{V}{(WS)} = \frac{K}{H} \qquad \text{(b)}$$

The left hand side of the equation is calculated by the experimental determination of the volume lost, as both the normal load and the sliding distance is known. From this equation it can be seen that the wear rate is inversely proportional to the hardness of the softer material. A drawback of the Archard equation is that it does not encompass the contribution that sliding velocity as well as surface topography has on the wear mechanisms and thus the wear rate.

The reason for reporting the total specific wear rate of the Ti-64/ball couple (Figure 49) instead of the specific wear rate of the Ti-64 samples was due to the fact that the wear rates of the steel balls were in the range of 10^{-14} while that of the Ti-64 samples was determined to be in the range of 10^{-12}. Essentially the total specific wear rate curve was identical to the specific wear rate curve for the Ti-64 samples.

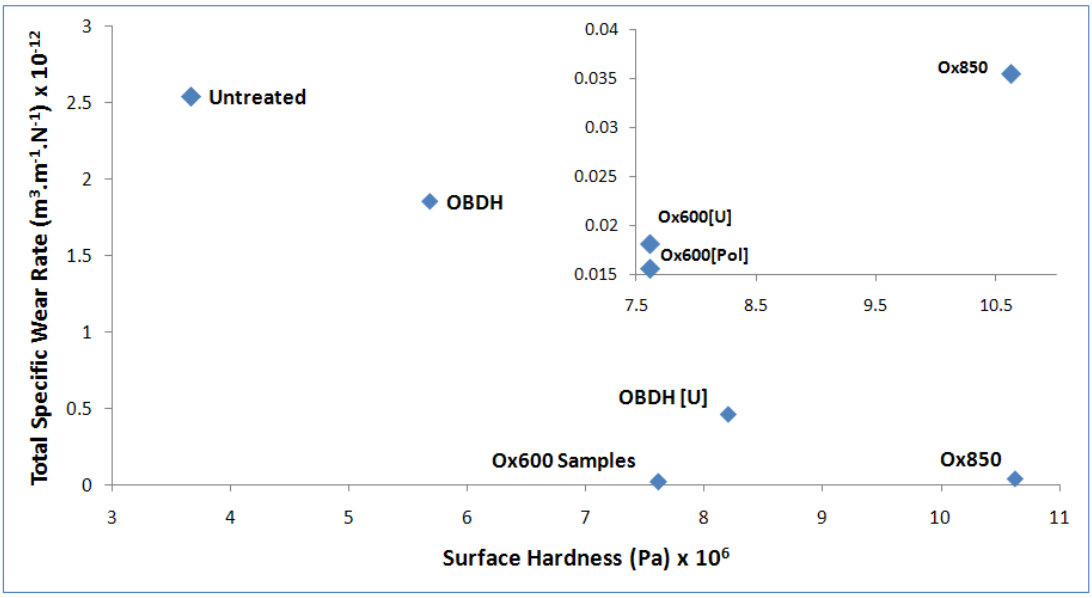

Figure 49: Plot of Total Specific Wear Rate (steel ball and Ti-64 sample) as a function of surface hardness for the various treatments. Wear rate calculated after a distance of 2400m.

When assessing the main plot of Figure 49, it would seem that the overall trend is that the experimental wear rates obtained obey the Archard wear equation as the wear rates are inversely proportional to the surface hardness. However, the OBDH [U] samples although having a higher hardness than both the Ox600 samples, exhibits a higher wear rate. When the points for the oxidation treated samples are magnified in the upper right corner of Figure 49 we see that although both Ox600 conditions are at the same surface hardness level their total wear rates differ by a marginal amount. Finally the Ox850 mated samples exhibits a wear rate double that of the Ox600 samples even though its surface hardness is 40% higher. This then shows that the experimental data obtained does not obey the Archard wear equation which but as was previously explained the equation itself does not take into account the types of wear mechanisms occurring at the contacting surfaces. In the case of the untreated and the OBDH sample the interaction is that of metal to metal contact but for the remaining samples a i.e. OBDH[U], Ox850 and the Ox600 samples the interaction is one of metal to ceramic. What is evident from Figure 49 is that between the hardness of the OBDH samples and that for the Ox600 samples there is a dramatic drop in the wear rate for the mated couple. When the specific wear rates of the steel balls are plotted as a function of surface hardness (Figure 50) we see the same outcome. No correlation can be made between the wear rate and the surface hardness of the Ti-64 sample. Although it was found that the results do not obey the Archard wear equation, a clearer understanding of the reason behind this will be evident after the wear mechanisms are analysed.

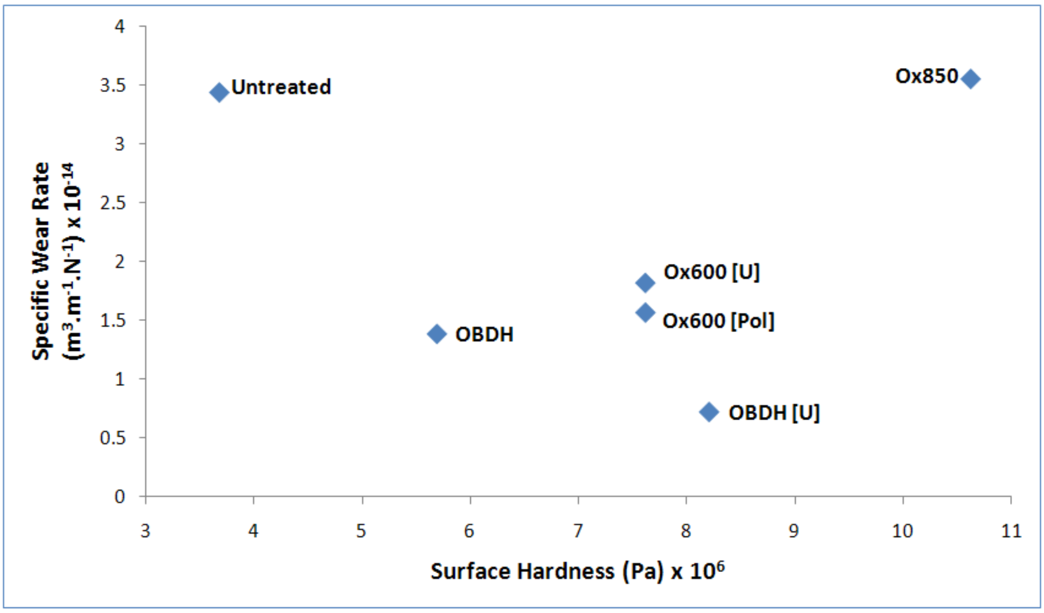

Figure 50: Specific wear rate of the steel balls as a function of surface hardness for the various treatments. Wear rate calculated after a distance of 2400m.

Figure 51 incorporates both scenarios of wear loss and shows the relative performance of the Ti-64 conditions after the wear tests. Most severe wear occurs in the mated pair of untreated Ti64 and the steel balls. Both the sample and the ball experience large degrees of wear when compared to the other treatments.

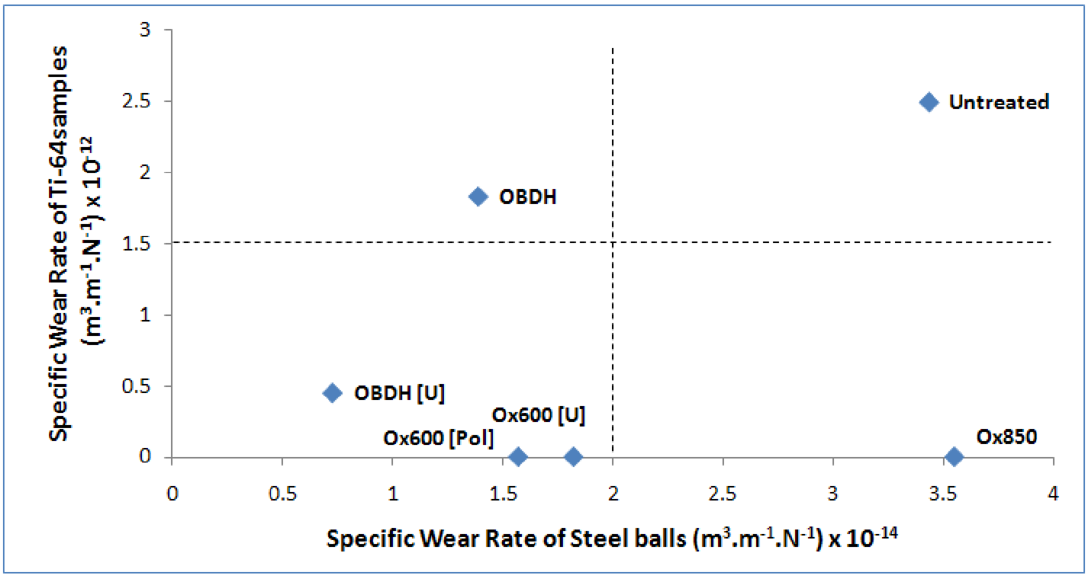

Figure 51: Quantitative representation of the wear performance for the different treatments showing the specific wear rates of the Ti-64 samples against the corresponding wear rates of the steel balls.

Although the OBDH treatment shows improved performance when compared to that of the untreated condition, the OBDH [U] samples provided the lowest wear rates with respect to the steel balls as well as decreased wear when compared to that of the OBDH samples. All the oxide treatments exhibit relatively low degrees of wear for the Ti-64 specimens. However, the highest wear rate for the steel balls occurs against the Ox850 treatment. Both Ox(600) treatments show low volume losses for the Ti-64 samples and the steel balls, relative to the other treatments.

7.1.1.2 Assessment of wear performance of OBDH samples without prior surface grinding

Certain tests were performed whereby boosted samples were not surface ground to a depth of 50µm to achieve a metallic finish. These samples once diffusion treated were subject to a small degree of polishing to lower the roughness to a more suitable value. Samples once prepared had an overall R_a value of 0.14µm ±0.04µm, and this was achieved by hand polishing using 3µm diamond paste under an approximate of 35N load for approximately 2min. Polishing removed the oxide scale that remained from the OBDH treatment and as discussed earlier the OBDH samples had a dark blue colour with certain areas being prone to a slight brown discolouration. These samples retained high hardness at the surface as the depth into the surface after polishing was shallow in comparison to the surface ground samples. This allowed the surface hardness to remain at a value of 753Hv ±16.2Hv instead of 537.5Hv ±21.4Hv. It is shown that this had a dramatic effect on the level of volume loss during the tests. These new OBDH samples, designated OBDH[U], were tested at 600m and 2400m. The results plotted in Figure 52 for this treatment are the result of two tests being performed at each distance.

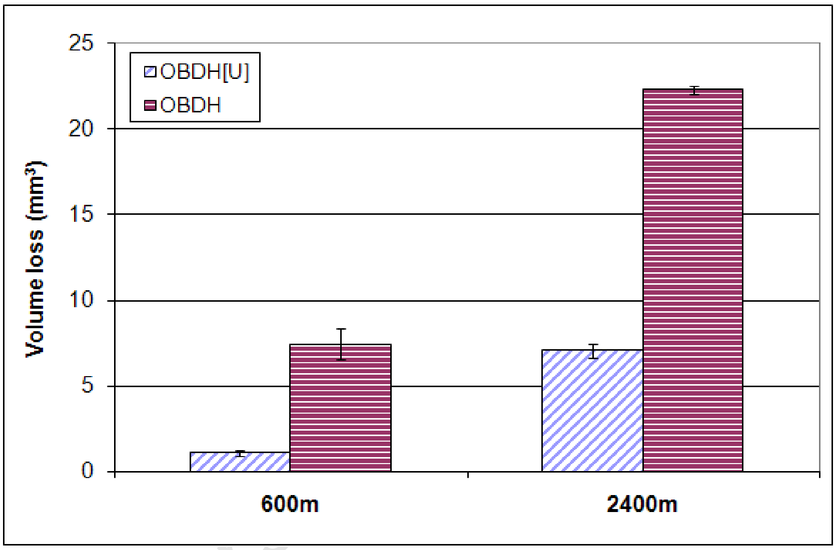

Figure 52: Volume loss of the OBDH[U] and OBDH samples after a sliding distance of 600m and 2400m.

It is clear that this condition provides a much greater improvement in the wear performance of the OBDH samples. As only a small degree of polishing is performed which removes an arbitrary amount of surface material, the samples retain the high hardness.

7.1.1.3 Work hardening of sub-surface layers

Cross-sections were taken of the untreated and OBDH samples to assess the level of plastic deformation that occurred directly below the wear scar. This is reported as hardness profiles as a function of depth below the scar. The results from these cross-sections are shown in Figure 53 and Figure 54. Hardness measurements were taken at depths of 20µm and 50µm below the wear scar to assess the degree of work hardening that the substrate material was being exposed to. The values reported in the graphs are averaged from 5 readings at each depth; this was repeated for the distances 200m, 500m, 1000m and 2400m.

It was discovered that between the distances of 0 and 500m for the ASR samples that there was an increase in the strength of the materials from the surface condition of 347Hv. After this distance the strength reaches a steady state and fluctuates around 418Hv. This is however not observed at a depth of 50µm below the wear scar, and it is shown that the hardness of the material fluctuates around the surface condition.

A similar "run-in" phase is seen for the OBDH samples, with steady state being reached after 500m. Stable hardness values at the 20µm depth after 500m fluctuates around 570Hv as opposed to the surface condition of 535Hv. Similarly no significant change occurs at a depth of 50µm. It is important to note that although both conditions exhibit a change in properties due to work hardening, the degree is greater in the ASR condition than for the OBDH samples. The ASR samples experience an increase in hardness of 20% while the OBDH samples show a 7% increase.

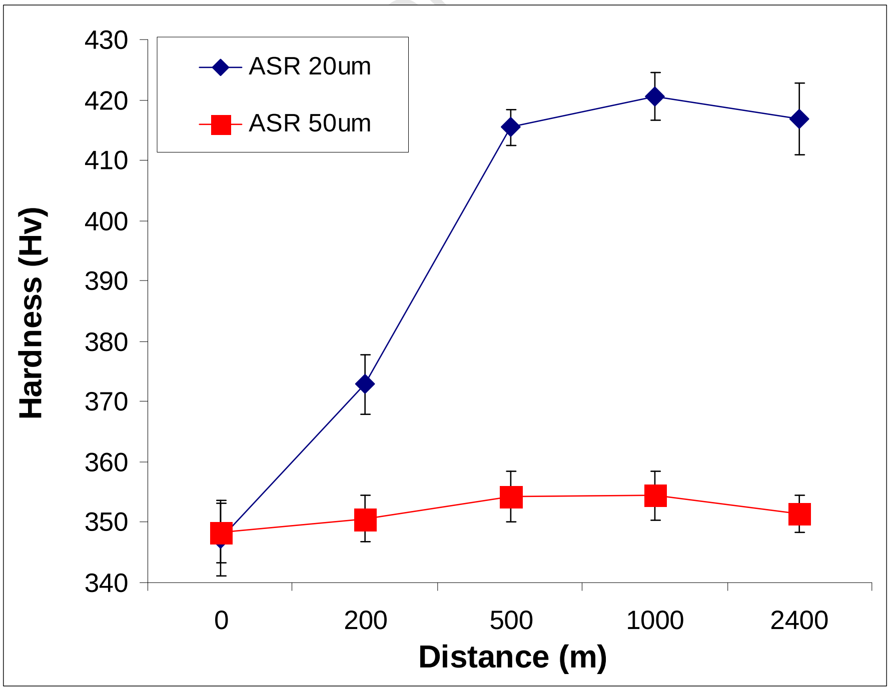

Figure 53: Hardness profile for the ASR condition showing work hardening below the wear scar, at depths of 20µm and 50µm, for various distance intervals.

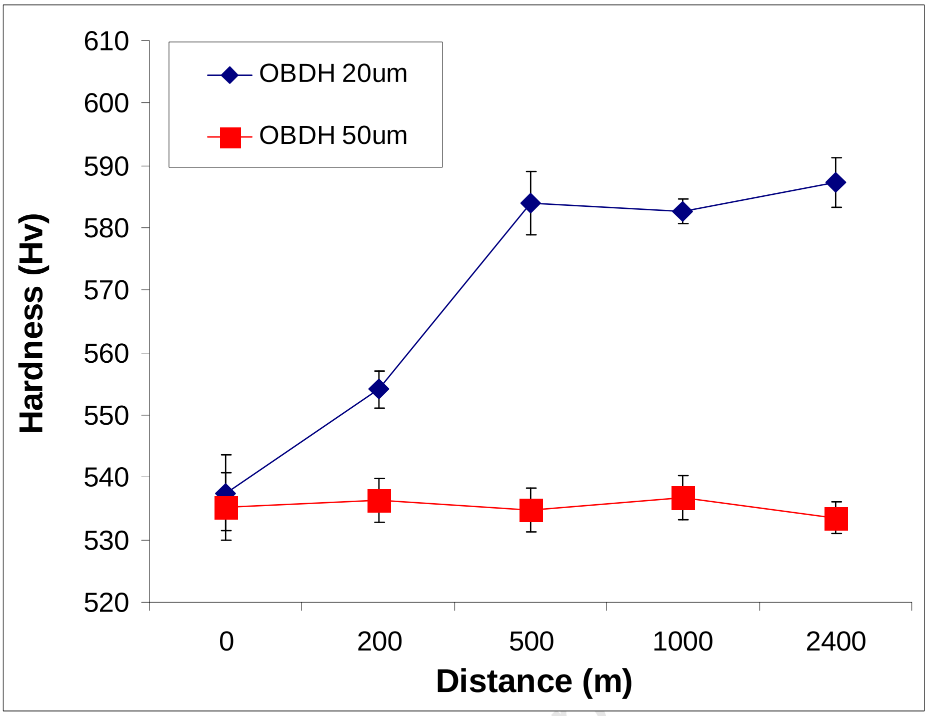

Figure 54: Hardness profile for the OBDH condition showing work hardening below the wear scar, at depths of 20µm and 50µm, for various distance intervals.

7.2 Examination of the Wear Surfaces

In this section the worn areas of the Ti-64 samples as well as the hardened balls are examined to assess the mechanism by which wear occurred during the tests. Secondary imagining as well as backscatter electron imaging was used to assess modes present.

7.2.1 The Untreated Condition

The greatest degree of wear was observed in the untreated condition, and was clearly shown in the previous section. These samples showed clear signs of stick-slip; adherence and transfer related wear which will be shown in the current sub-section. Figure 55 is a SEM secondary image of the wear track of the untreated condition after a wear test of 300m. The sliding direction is indicated (bold white arrow) and a section of material deposited on the surface is highlighted (red circle). It can be seen that the surface was subject to abrasive wear and this is evident by the abrasive grooves, which were found throughout the track. A 3-D representation taken of a section of the wear track is shown in Figure 56 (a) Numerous surface profiles were taken at 1.5mm spacing over a pre-determined area; the profiles were then combined to form a 3-D construction of the wear scar. The illustration shows abrasive grooves which are likely caused by hard particles ploughing through the softer ASR material. Areas that have been plastically deformed during sliding motion are also labelled.

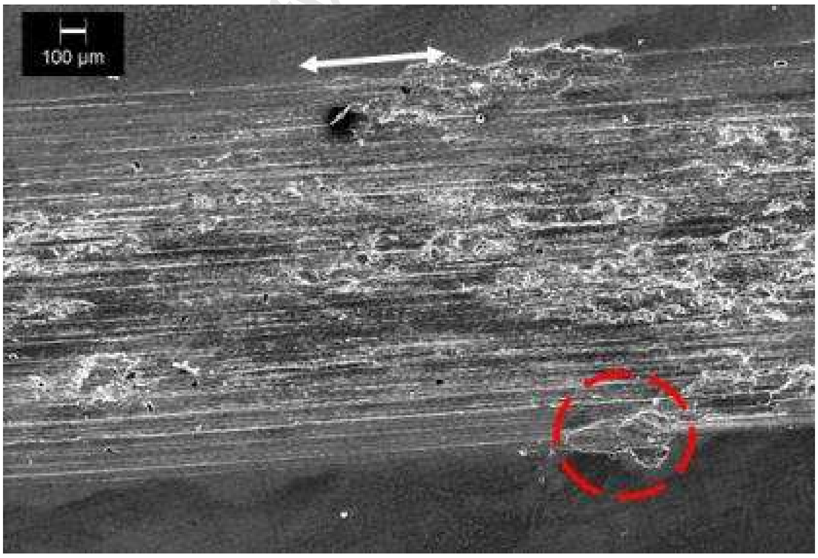

Figure 55: Secondary image of the wear track of a Ti-64 specimen in the As-received condition showing various features.

An EDS analysis (Figure 56 (b)) of the deposited area presented in Figure 55 showed that Ti and Fe were present in the material. Due to the interaction volume of the electron beam it is difficult to assess actual quantitative compositions for the material being investigated. However the EDS data does indicate that Fe has been transferred onto the surface of the Ti-64 sample.

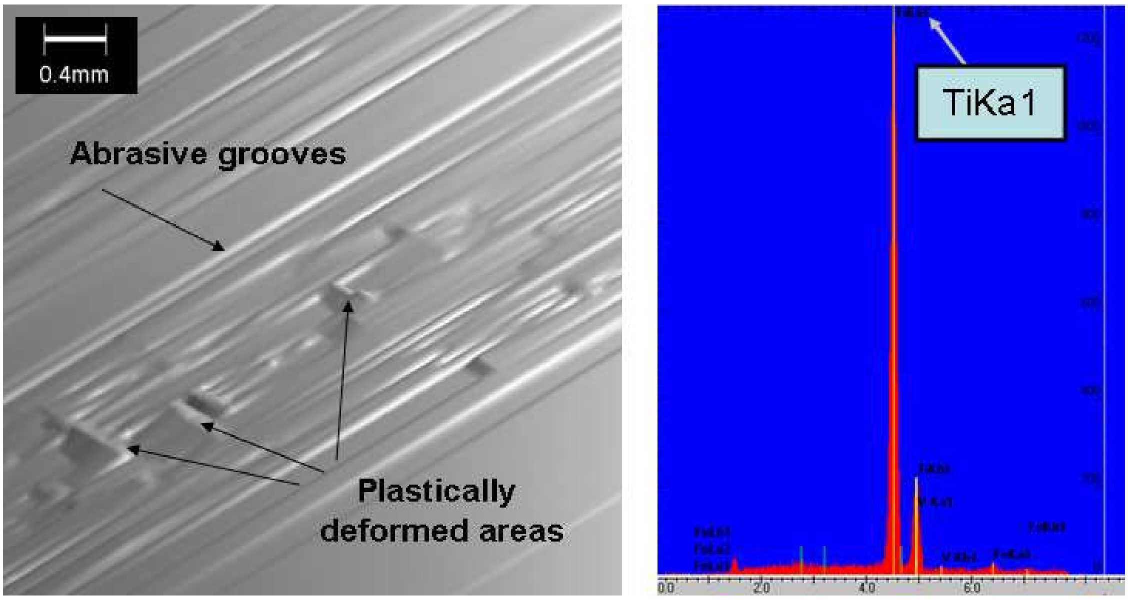

(a) (b)

Figure 56: (a) 3-D image of a section of the wear track showing abrasive grooves and plastically deformed areas, (b) EDS analysis of a section of material found on the surface.

This type of wear is common for metal/metal sliding surfaces where one material is significantly harder than the other material. The harder material ploughs into the softer material causing plastic deformation in the surface layers of both materials, but to a larger extent in the softer metal. These plastically deformed regions can be removed as the tangential forces overcome the shear strength of the material. The removed hardened areas are then pulverised into smaller wear particles. These hardened particles plough through the softer material by the process of three-body abrasion, being trapped between the two surfaces during sliding. Another method for the formation of hardened particles would be through asperity removal via adhesive forces. The asperities are removed and then become work hardened between the surfaces. Figure 57 (a) shows a wear particle found on the surface of the wear track of the ASR sample. These particles are primarily responsible for the formation of the abrasive grooves shown in Figure 56 (a). An EDS scan of the particle shows that both Ti and Fe were present. This indicates that the particle itself contains Fe, either through mechanical alloying occurring during sliding or that the particle itself was removed from the steel ball. As discussed earlier under constant load and deformation, areas become work hardened. When exposed to high pressures and sudden impacts localised surface and sub-surface cracks form in these regions. Together with strong adhesive forces these cracks propagate and result in entire sections of the surface being removed. This type of delamination wear is shown in Figure 58 (a) in which an entire area of the Ti-64 surface was removed. This delaminated material is carried between the two surfaces until it is deposited on either the Ti-64 or the steel ball surface. A magnified image of a transfer layer is shown in Figure 58 (b). This was found on the Ti-64 wear track and EDS analysis showed that Fe was present. Delaminated segments can also be deposited on the pin surface. Figure 59 (a) shows the wear scar of the ball worn against the Ti-64 specimen where deposited material is indicated (red arrow). The results of the EDS scan are shown in Figure 59 (b), which shows a large degree of Ti present. As the surface below the deposited material is that of the steel ball, it would be expected that due to the interaction volume, that a higher peak for Fe would be present. This, however, is not what is observed. A large peak for Ti is present with smaller quantities of Fe which would indicate that the deposited material is sufficiently thick to decrease the discrepancies introduced by the interaction volume. What the results have indicated is that during the sliding of the untreated Ti-64 and the steel ball, material from either surface is removed, and is either transferred to the opposite surface or deposited on the same surface.

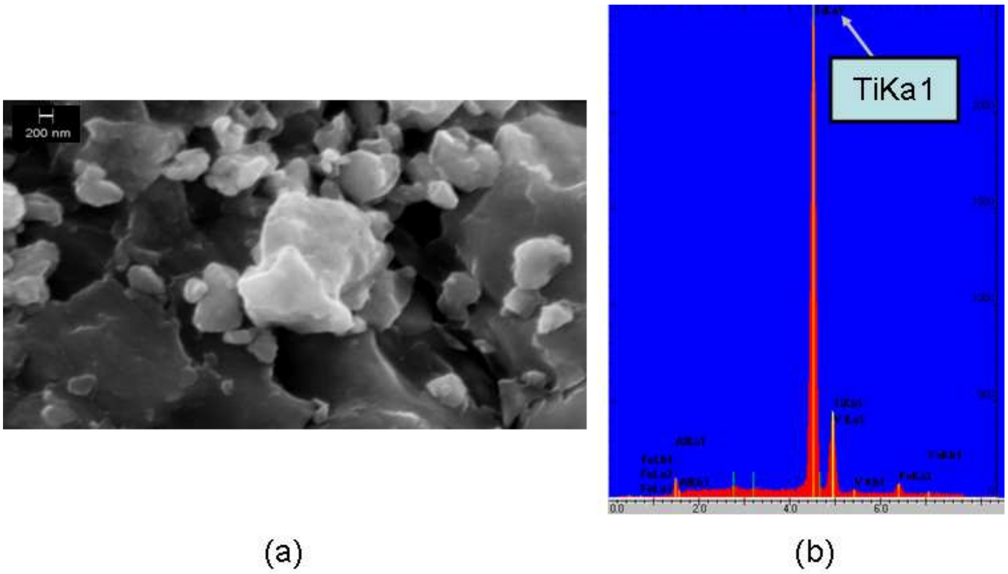

Figure 57: (a) A wear particle found on the wear track, and (b) an EDS scan of the wear particle.

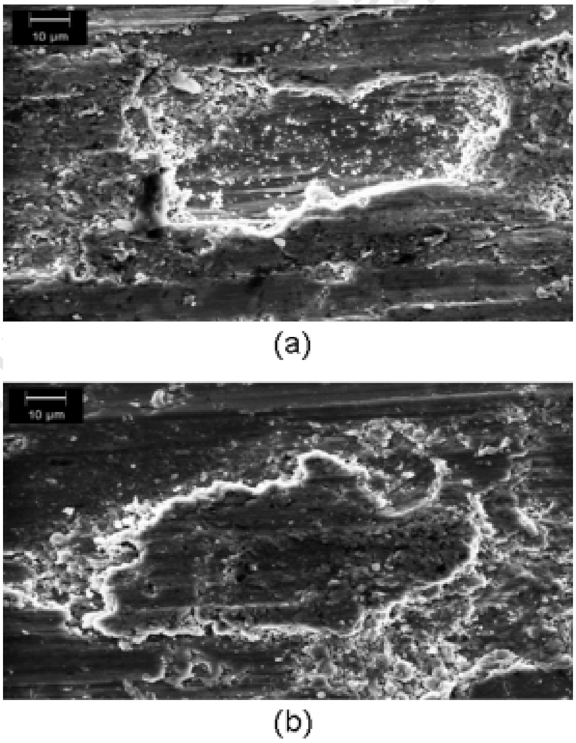

Figure 58: Secondary images of (a) section of Ti-64 removed due to the process of delamination and (b) a transfer layer of Ti and Fe on the worn surface of the Ti-64 sample.

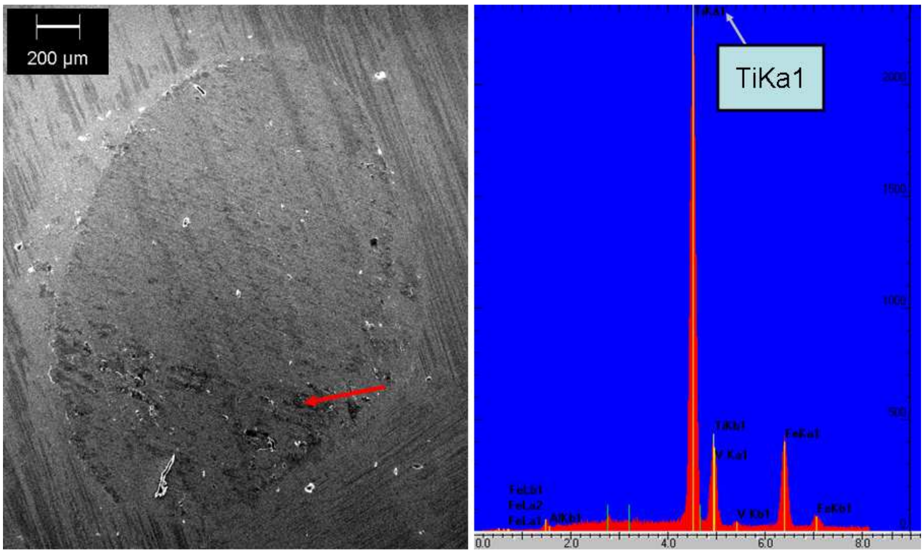

(a) (b)

Figure 59: (a) Wear scar of the pin (steel ball) with Ti-64 transfer layers shown by the red arrow and (b) the EDS scan of deposited material on the surface of the steel ball.

As described before, during the motion of a hard body against a softer ductile material the softer material deforms. This can lead to material build-up in front of the hard body. This build-up increases the resistance to motion of the hard object, increasing the linear friction to a point where the harder object moves over this build-up. The increase in friction and sudden drop when the hard body traverses the built-up area can be seen as fluctuations on a frictional coefficient plot and is known as stick-slip. This is shown in Figure 60, which is of the worn area of the Ti-64 surface. The material build-up is shown by the red arrow while the white arrow indicates sliding direction. Another important aspect to consider is that as the steel ball moves over the built-up material and lands on the following surface, the impact on this already plastically hardened layer can very well contribute to the formation of the cracks involved during delamination. These impacts further increase the strength of the material, consequently decreasing the ductility, and pulverise any wear debris beneath to form smaller wear particles. Hardness measurements of the area directly beneath the wear scar proved this (Figure 53 and Figure 54) and showed that the material strength was increased from the bulk hardness.

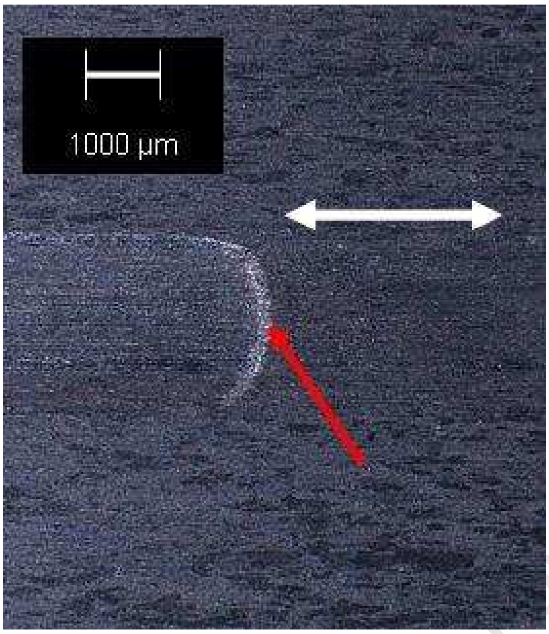

Figure 60: Magnified image of the wear track of a Ti-64 specimen after a 2400m wear test showing plastically deformed regions (red arrow) resulting in stick slip.

7.2.2 The OBDH treatment

7.2.2.1 OBDH samples surface ground to a 50µm depth

The OBDH samples show an increased wear resistance under the same test conditions when compared to the ASR samples. This is shown by the decreased wear volume exhibited by these samples and shown in Figure 47.

A closer look at the wear mechanisms involved during the tests shows that similar modes of wear occurred in the ASR and OBDH samples. In Figure 61 deep abrasive grooves are indicated (red arrow) as well as the sliding direction (white arrow). This would be expected as although the surface is harder than the ASR (537.5Hv compared to 347.2Hv) the steel ball hardness is *ca* 750Hv and thus the scenario is still that of a harder wear pin mated against a softer counter-face.

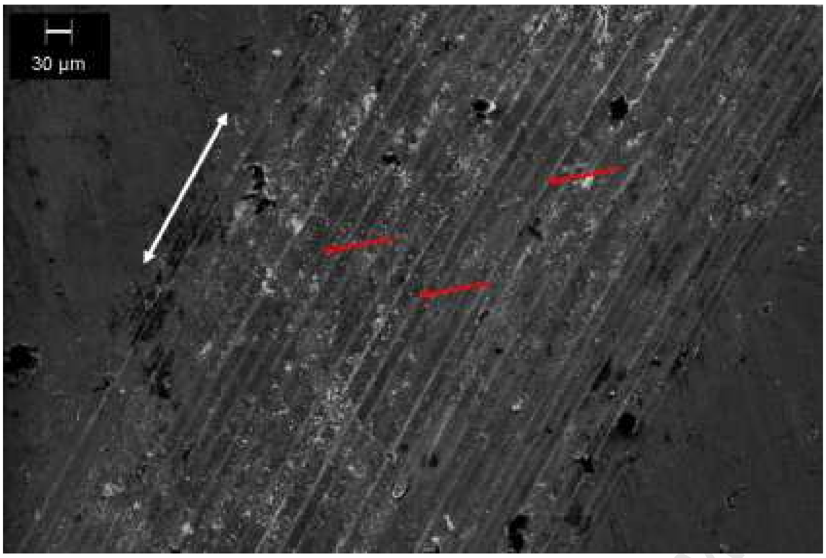

Figure 61: Secondary SEM image of the wear track of an OBDH treated sample, worn against a steel ball for a distance of 1200m. Points of interest shown are abrasive grooves (red arrows).

The OBDH samples show an increase in hardness due to the oxygen diffusion into α-phase Ti; however this causes the sample to lose ductility and become embrittled. As a result the OBDH samples are prone to cracking in these hardened layers. This was shown in Figure 41, where cracks formed in the ODZ. These cracks when exposed to high adhesive and tangential forces propagate and lead to delamination of entire segments. Figure 62 (a) shows an area where material was removed (red arrow) as well as a crack on the surface (white arrow). The area where the segment was removed is filled with wear particles. An EDS scan of a wear particle found on the OBDH surface is shown in Figure 62 (b). The result is that both Ti and Fe are present in the particle. Although the actual composition of the particle itself is not known, the presence of Fe indicates that the abrasive wear particles originate from both surfaces. Although the OBDH surface is harder than the ASR condition, work hardening will still increase the surface hardness of the OBDH specimen, as shown in Figure 54. Wear particles formed from this hardened material will be able to plough into the OBDH surface. Together with the hard wear particles formed from asperity removal and pulverised transfer layers of the ball material, this wear debris causes the abrasive grooves seen in Figure 61. As was seen in the ASR condition, these segments of material can be removed and deposited back on the sample surface or the surface of the pin (ball). A section of deposited material found on the OBDH worn surface is shown in Figure 63 (a). An EDS analysis of the material (Figure 63 (b)) showed that Ti and Fe was present; this would imply that material removed from the steel ball during sliding becomes deposited on the

OBDH sample surface. Similar transfer areas were found on the surface of the untreated Ti-64 specimens.

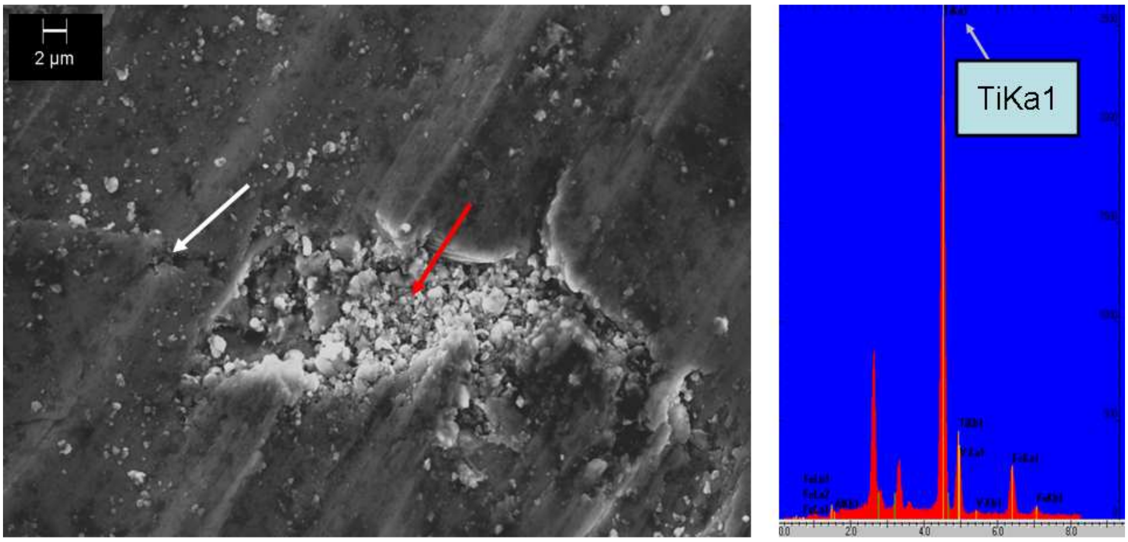

(a) (b)

Figure 62: (a) Area on the surface of an OBDH sample where material was removed via delamination (red arrow), as well as a surface crack (white arrow) and (b) an EDS scan of a wear particle found on the OBDH surface.

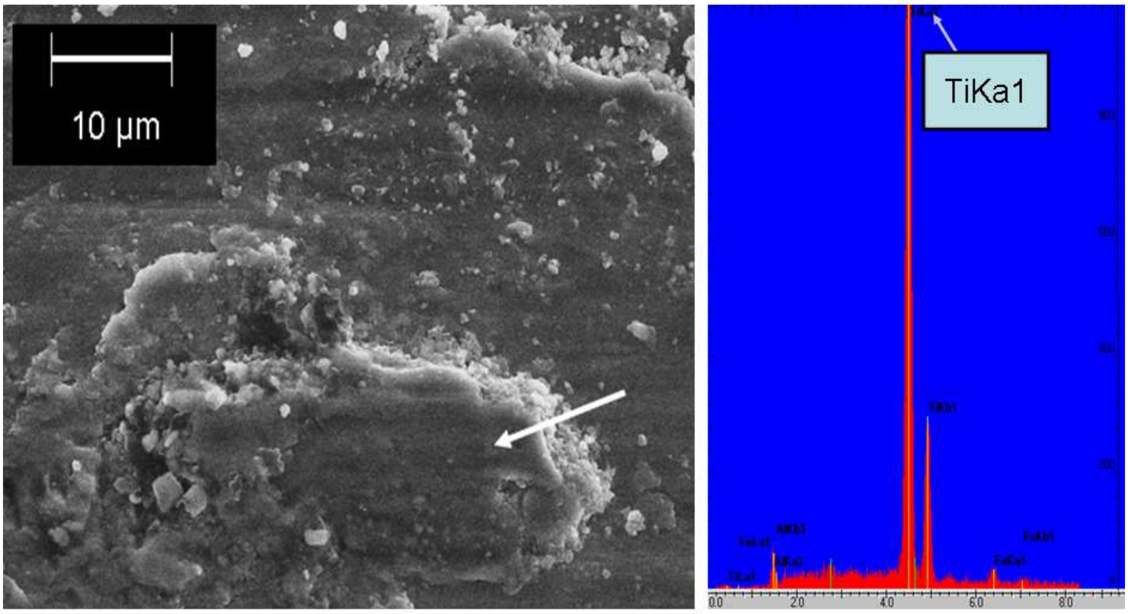

(a) (b)

Figure 63: (a) Deposited material on the surface of the OBDH sample and (b) an EDS scan of the deposited layer.

Analysis of the ball wear scar showed material deposits and abrasive grooves. The worn area of the steel ball in Figure 64 (a) is definitely elliptical in shape and not circular. This definitive shape is also seen in the worn areas of the steel balls which were mated against ASR samples and is common for wear of spherical surfaces in mated systems which exhibit plastic deformation type wear. The worn area is curved, as both the ball and the counter-face are wearing simultaneously, as opposed to a flat wear scar. The longest length of the elliptical worn area is perpendicular to the sliding direction.

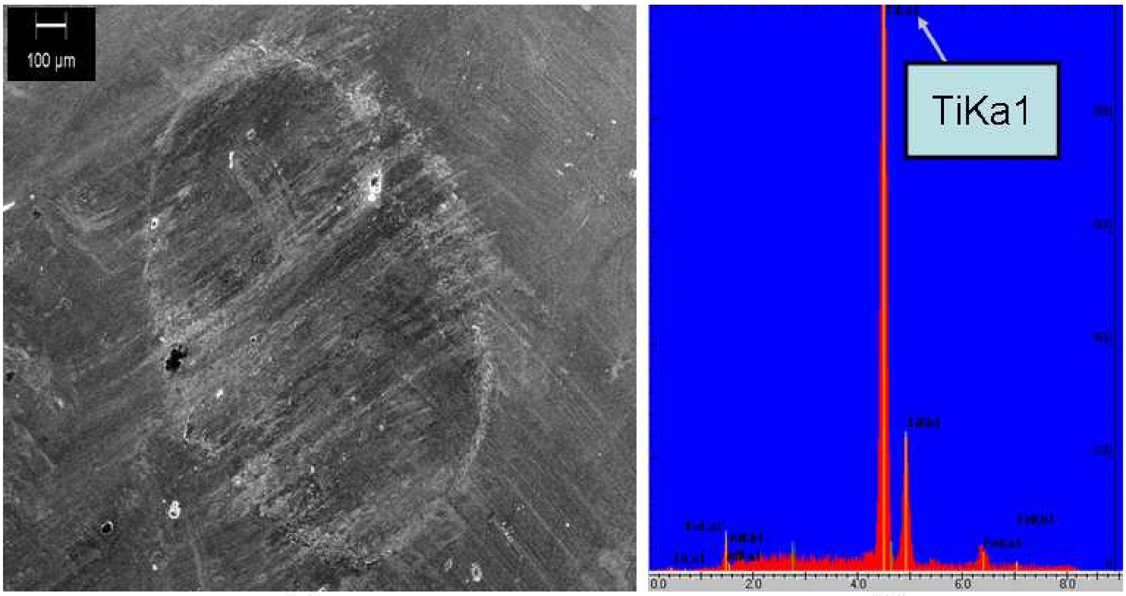

(a) (b)

Figure 64: a) Wear scar of a ball worn against an OBDH specimen and (b) an EDS scan of deposited material found on the surface of the ball.

EDS analysis of the deposited material found on the worn surface of the steel ball shows that the composition consists of Ti and Fe. Although no quantitative results can be drawn from this the high count of Ti for the deposited material on a steel substrate indicates that the material was transferred from the OBDH surface.

From the analysis of both ASR and OBDH samples and the relative steel balls it is apparent that material is being removed from both surfaces. The removed material is then deposited either on the original surface or as transfer material on the opposite surface. This is supported by the volume losses seen for both the Ti-64 counter-faces and the relative steel balls. Due to the fact that no signs of delamination wear occurred for the steel balls mated against both ASR and OBDH samples, volume loss would then be attributed to abrasive ploughing and asperity removal from adhesive forces. Material removed from both surfaces might also become trapped between the sliding pair leading to three-body abrasion; these hard wear particles being the primary reason for the formation of the abrasive grooves. A combination of asperity removal and deposited material fragmentation coupled with work hardening are also accepted sources for the formation of these hard wear particles. Oxidative wear was considered as a possible mechanism occurring during these wear tests because of the exposure to an air environment and hot surface temperatures. However the presence of oxygen on the surfaces as well as the wear debris was difficult to monitor due to the low capability of the detector to measure for light elements. Thus the presence of oxidative wear could not be confirmed.

7.2.2.2 The improved wear performance of the OBDH[U] samples

In separate tests performed, OBDH samples were not subjected to the 50µm surface grinding to acquire a metallic finish. These samples were however polished to a surface R_a that was closer to the surface conditions required for the wear tests. It was previously shown that these OBDH[U] samples exhibited superior wear performance when compared to surface ground OBDH samples. Figure 65 (a) is the wear scar formed on the surface of an OBDH[U] sample worn through a sliding distance of 600m. No real signs of abrasive wear are evident on the Ti-64 surface; however there is a large degree of deposited material which occurs throughout the track (red arrow).

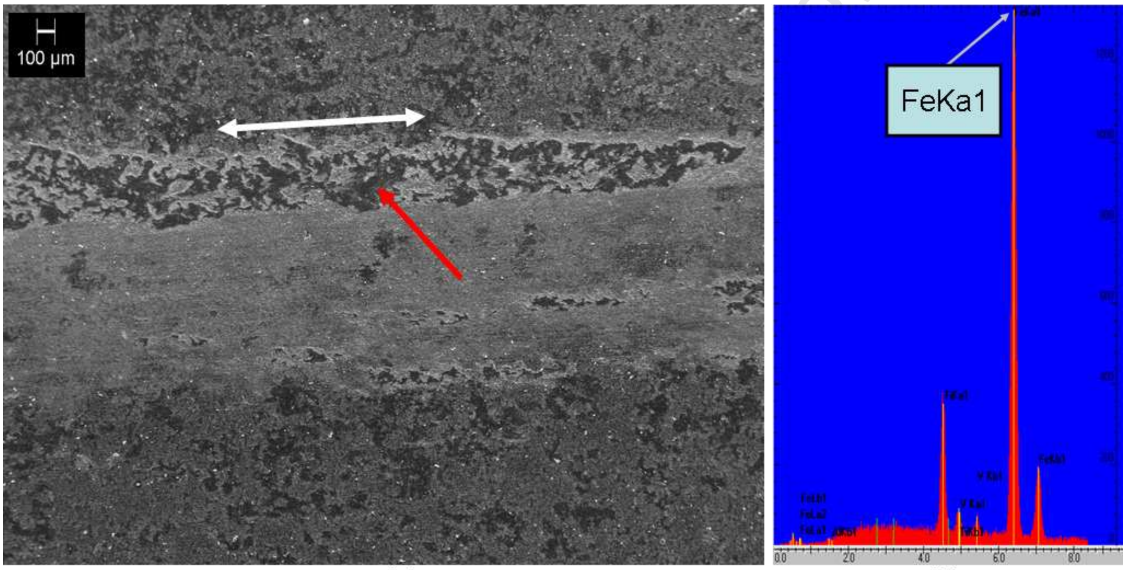

(a) (b)

Figure 65: (a) Wear track of an OBDH sample not subjected to the 50µm surface ground preparation and (b) an EDS scan of the deposited material highlighted in (a).

An EDS analysis of this transfer layer (Figure 65 (b)) along the track showed that the composition was that of Fe and Ti. However, unlike all other EDS scans thus far the major peak was found to be that for Fe. As this was taken on a Ti surface, it shows that the deposited material consists largely of Fe. This greatly contrasts the deposited material observed on the surface ground OBDH specimens. Wear tracks along these samples typically had a width of 1.2mm (at a 600m distance) compared to the average wear track width of 1.3mm for a 50µm surface ground OBDH sample at 100m distance. Together with the lower volume losses that were previously shown this condition shows a vast improvement in the wear resistance of the material. However in industry parts manufactured would be required to be uniform in their surface appearance. Due to this requirement, the metallic finish of the OBDH samples surface ground to a 50µm depth satisfies the condition.

7.2.3 *Air Oxidation Treatments*

7.2.3.1 The 850ºC Oxidation Condition

As with the samples that were oxidised at 600ºC, the worn samples of this treatment show no measurable or observable signs of a wear region into the actual titanium surface. In Figure 66 the wear track of the Ox850, worn through a distance of 2400m, is composed of large regions of deposited material which run along the length of the track. These areas are marked (red arrow) and the sliding direction is indicated (white arrow).

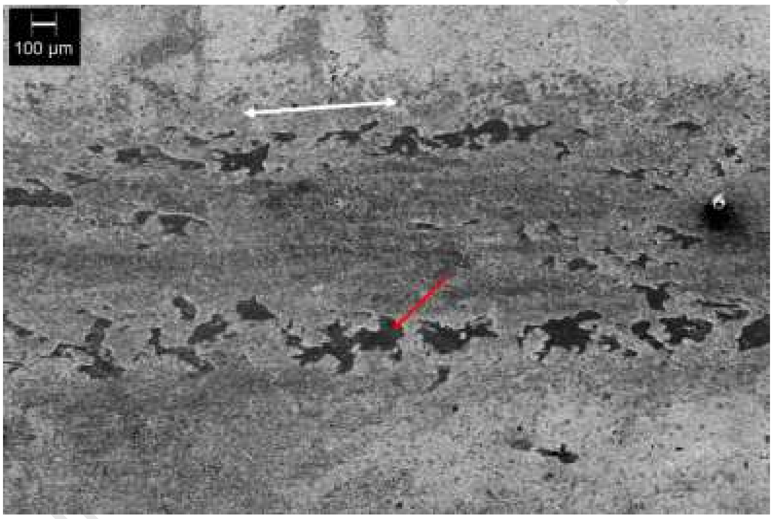

Figure 66: Wear track on the surface of an Ox850 sample worn through a sliding distance of 2400m, highlighting deposited material (red arrow).

An EDS scan of the deposited material is shown in Figure 67 (a), and the result shows that although Ti and Fe are both present, the main peak is that for Fe. A similar scenario was seen for the OBDH samples that were not surface ground, on which material spread along the surface of the wear track showed high amounts of Fe. No measurable volume loss could be determined for these samples, and from the analysis of the worn surface it is evident that ploughing of the oxide was not a dominating wear mechanism. Evaluating the wear scar of the ball provides more insight into the modes of wear that occurred. The ball wear scar, Figure 67 (b), is not elliptical in nature. The circular shape is evidence that the wear scar is flat and not curved as those seen in the cases where the counter-face was ASR and OBDH treated samples. This flat scar implies that no large degrees of plastic deformation type wear occurred between the mated surfaces as well as the fact that the ball was experiencing much larger degrees of wear than the counter-face. The former conclusion is derived from the first scenario of linear reciprocating wear as described by the ASTM standard G133. This shows that the ball of the sliding pair exhibits a flat scar when only the ball wears and the counter-face is left relatively unaffected.

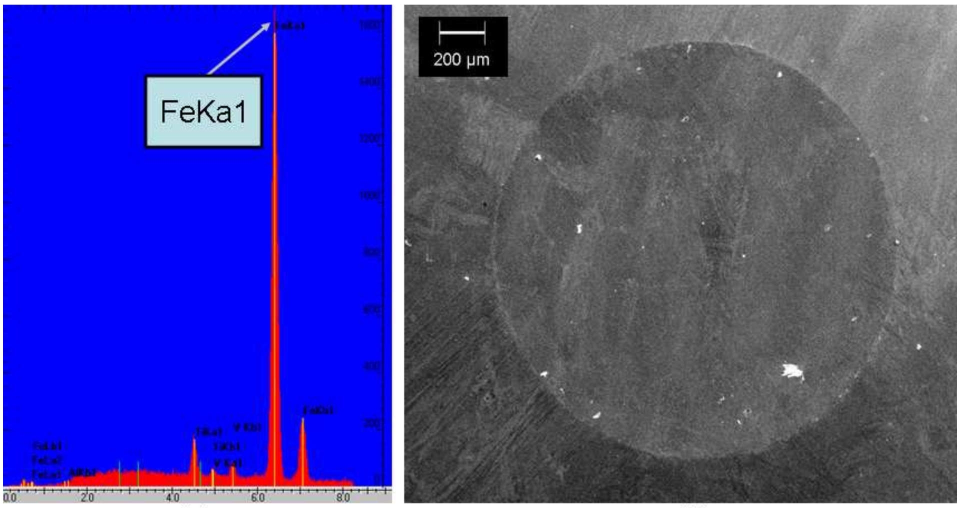

(a) (b)

Figure 67: EDS scan of the deposited material found on the Ox850 worn surface and (b) the wear scar of the ball mated against the Ox850 surface.

As the counter-face (test specimen) does not undergo any plastic deformation, which is expected as the rutile layer formed as the protective surface is a brittle ceramic, no stick-slip will occur within the oxidised Ti-64 material. This greatly lowers the degree of fluctuations in friction that will be experienced and would be clearly seen on the frictional coefficient plots. This would assist to stabilise the steady state friction coefficient, minimising deviation. Wear of the steel balls would then be due to strong adhesive forces causing asperities to break off, and be carried beneath and ahead of the steel ball. These particles would be work hardened and thus act as abrasives which through the process of three-body abrasion would result in wear of the ball. No delamination type wear was seen on the wear surface of the ball, and large deposits of Fe onto the Ox850 surface would have to form by some other process. A hypothesis for the formation of these deposited layers is that wear debris from the ball would agglomerate forming larger nuggets of material, and these would become transfer layers on the Ox850 surfaces. However no evidence was discovered supporting this theory and it therefore remains speculative.

Particles were analysed that did not reside in close proximity to the deposited material, to assess whether rutile fragments were formed during the sliding motion between the two surfaces. One such particle and the subsequent EDS scan are shown in Figure 68 (a) and (b) respectively. The particle showed a composition which consisted largely of Ti. Although Fe was input into the EDS scan search, the peaks for this element were very minor and this would suggest that the particle consists almost entirely of Ti. As oxygen compositions were difficult to monitor by this method, it is assumed that such a particle would be a fragment from the oxide layer. The mechanisms of removal of such a fragment would be propagation of cracks (pre-existing within the oxide), under impacts and strong adhesive forces. The cracks cause sections such as these to be removed from the oxide layer. Figure 43 (b) shows the degree of porosity that lies beneath the surface of the oxide, and it is the porous areas where cracks nucleate or propagate. These hard oxide fragments are a main cause for the high degree of volume loss experienced by the steel balls mated against the Ox850 samples.

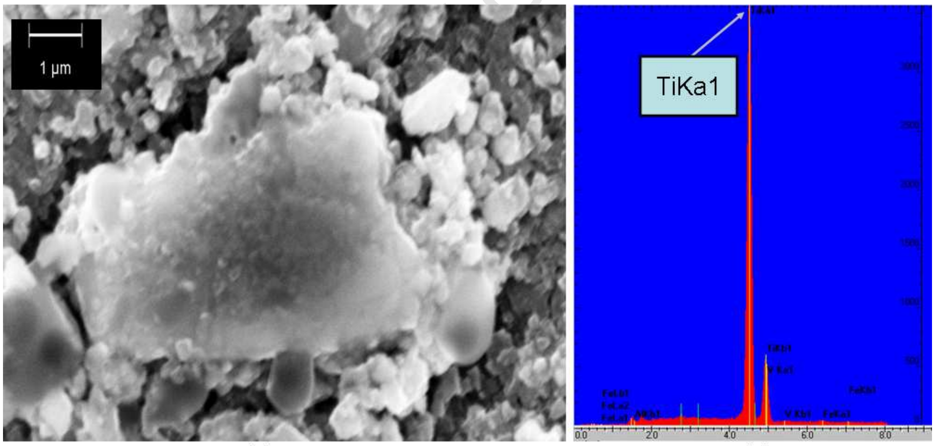

(a) (b)

Figure 68: (a) Wear particle found on the surface of the Ox850 sample and (b) an EDS scan of this wear particle.

7.2.3.2 The 600ºC Oxidation Condition, Unpolished

Wear mechanisms that occurred for the Ox850 samples were similarly found on the Ox600 samples. The wear tracks of both conditions for Ox600 samples consisted of deposited layers of material. Worn areas of the steel balls were circular in nature as those seen for the Ox850 samples.

The wear track shown in Figure 69 is that of an Ox(600)[U] sample worn through a distance of 2400m. The track consisted largely of deposited material. As with the Ox850 samples, no measurable volume loss could be determined by profilometry for these samples. However a low degree of wear is noticed for the oxide layer. The red arrows of Figure 69 show scratches which travel from the unworn areas of the Ox(600)[U] into the wear zone. This is significant in showing that the wear of the surface was not large enough to remove evidence of these deeper scratches. The areas highlighted by the yellow arrows show shallower scratches which disappear upon entering the wear zone. This qualitative analysis shows that wear of the protective oxide does occur but at a very limited scale.

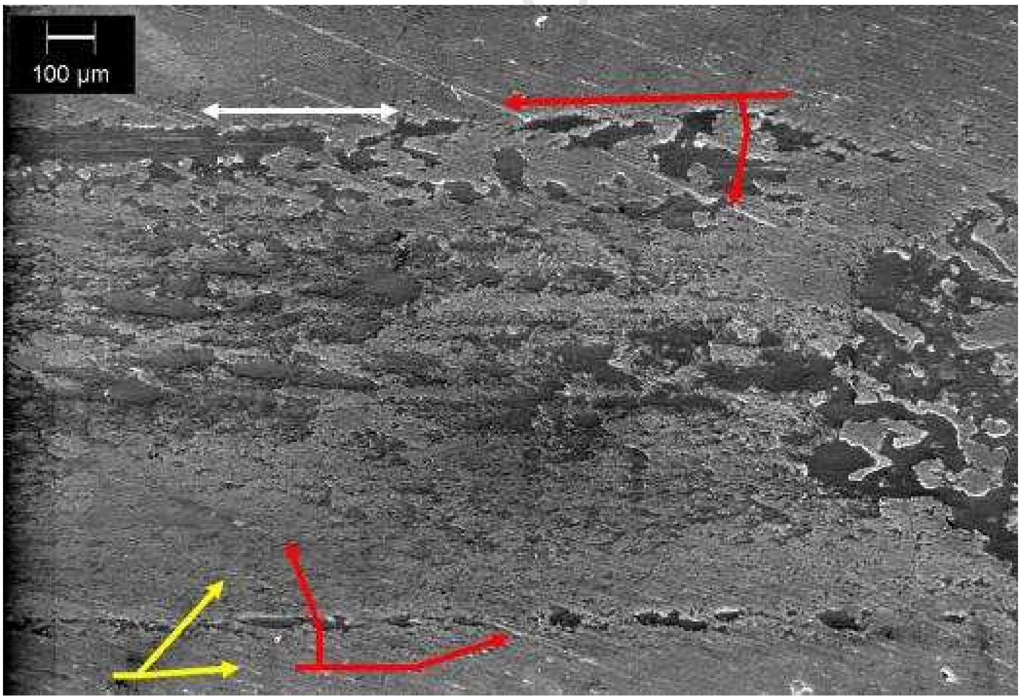

Figure 69: Wear track on the surface of a Ox(600)[U] sample after a sliding distance of 2400m.

A magnified image of the wear track is shown in Figure 70. The left hand portion is the secondary image of the track while the right side is the subsequent backscatter electron image.

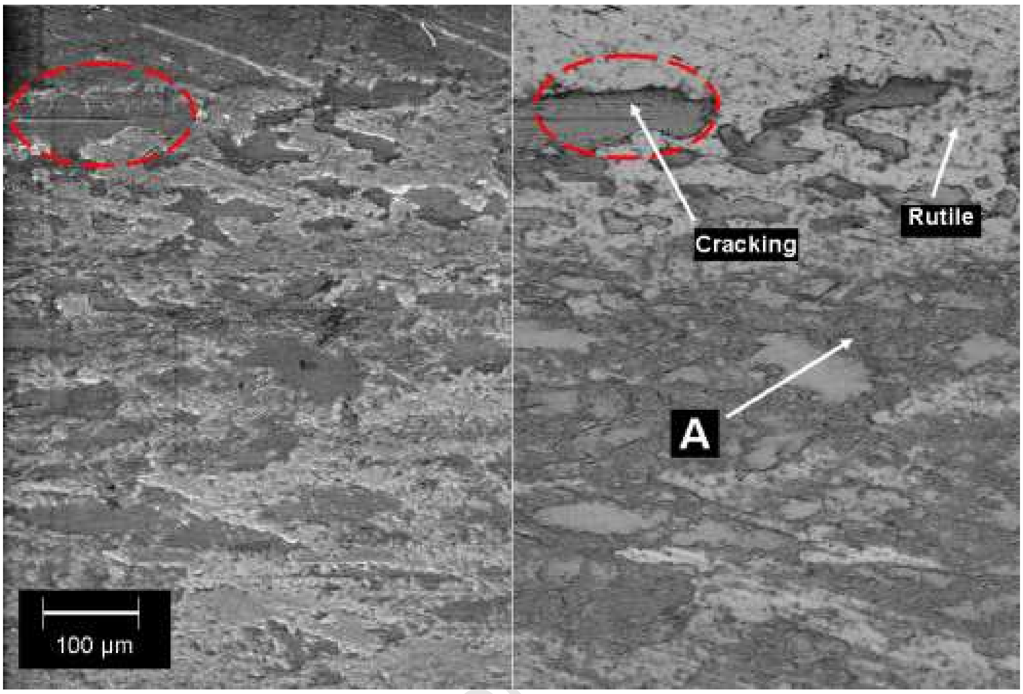

Figure 70: Secondary image of a section of the wear track of the Ox(600)[U] sample (left) and the backscatter electron image of the same region (right).

The deposited material was analysed via EDS examination, Figure 71 (a), and it was shown that these regions consisted of Fe and Ti. A larger peak for Fe, for material on a rutile substrate, would imply that these regions have high Fe content. Therefore the ball is losing material and it is being deposited as transfer regions on the surface of the Ox(600)[U] samples. The backscatter image shows that 3 major types of materials are present on the surface of the wear scar. The original rutile layer, the deposited material consisting largely of Fe and darkened regions between these deposited layers (labelled A). An EDS analysis of the area labelled A as presented in Figure 71 (b) shows that both Ti and Fe are present. Closer analysis of this region showed that it consisted largely of loose wear particles. Another important aspect of this image is the cracking observed on the surface of a section of deposited material. The cracking signifies that the surface condition of that material has become embrittled.

The shape of the ball scar as shown in Figure 72 (a) illustrates that little plastic deformation type wear was experienced as previously discussed for the Ox850 steel balls, which showed the same shape for the ball scar. Although no signs of deposited material existed on the ball surface small wear particles were found. An EDS analysis of one of these particles is shown in Figure 72 (b). A large peak for Ti for a particle found on the surface of an iron substrate would signify a large Ti composition for this particle. It is previously shown that low degrees of wear do in fact occur on the rutile surface. These key points indicate that oxide particles are being removed from the treated Ti-64 surface due to high adhesive forces, as this is a common mode of asperity removal for oxide/metal interactions. As a result the ball surface is being worn by hard oxide particles.

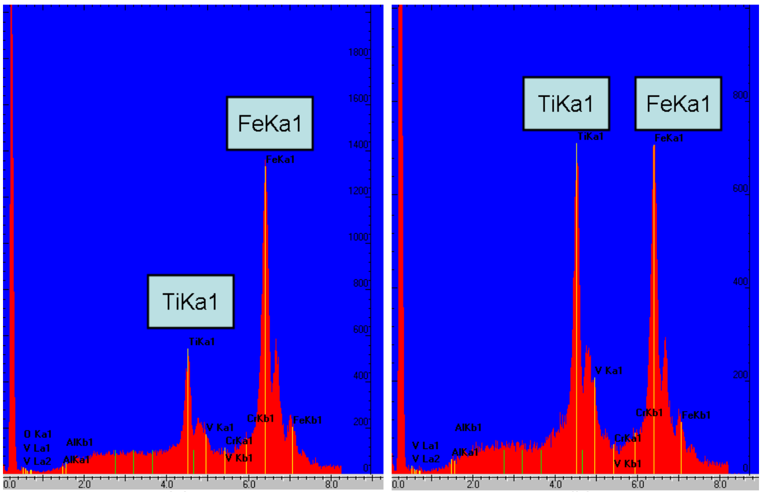

(a) (b)

Figure 71: (a) EDS scan of deposited material of the wear scar and (b) an EDS scan of the darkened region labelled A on Figure 34.

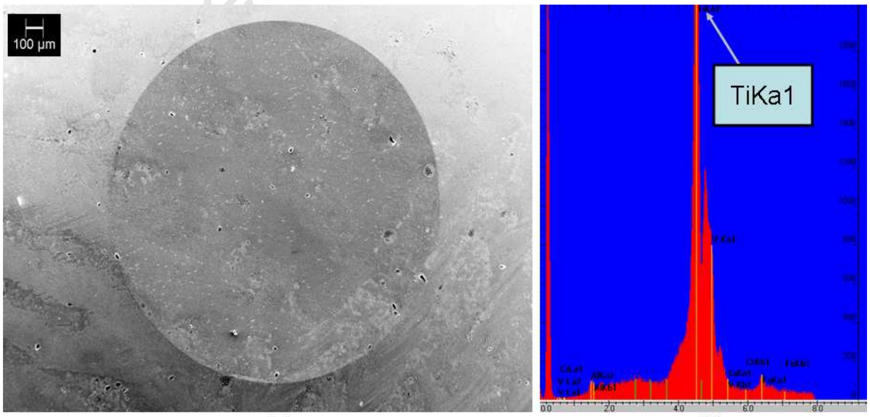

(a) (b)

Figure 72: (a) The wear scar of the ball worn against an Ox(600)[U] sample after 2400m sliding distance and (b) an EDS scan of a wear particle found on the surface of the ball.

7.2.3.3 The 600ºC Condition, Polished

These samples produced the most satisfactory results for the wear tests in terms of volume loss. From Figure 51 it is clear that the tests of these samples show low Ti-64 volume losses coupled with low volume losses for the steel ball. This is the ideal situation whereby both materials are protected during interaction by the modification of only one of the surfaces/materials.

Figure 73 is the secondary image of the wear scar of a Ox(600)[Pol] sample worn through a sliding distance of 2400m. The red lines provide a focal point for the wear zone and the sliding direction is indicated with a white arrow. It is easily seen that when compared to Figure 69 that there is a much lower degree of material deposition taking place at the surface. A magnified section of the wear scar of the Ox(600)[Pol] is shown in Figure 74. Topography analysis (left) shows that small areas of transfer layers occur throughout the wear track of the samples. EDS analysis of the deposited material showed large peaks for Fe, Figure 75. As this is a titanium oxide substrate, the Fe content of the deposited layer is significant when considering the interaction volume. Although the oxide appears to exhibit limited wear it can be seen that small areas have been removed from the surface (Figure 74, white arrow) and that fine abrasive grooves (Figure 74, yellow arrow) exist in the sliding direction. As the surfaces contact during sliding motion the asperities of the softer steel ball become plastically deformed and removed. This results in transfer layers of Fe on the surface of the oxide. As this material transfer increases in amount the mated surfaces change from oxide/steel to steel/steel increasing the tangential forces at the sliding surfaces.

As a result of the increase in tangential forces the deposited material can be detached again, and pulverised between the surfaces to form wear debris. Detachment of these oxide layers usually occurs at the oxide/transfer layer interface due to the lower adhesive forces maintaining this interaction when compared to the shear strength of the substrate or deposited material. However, this detachment can occur at the oxide/substrate interface provided that sub-surface cracks are present in the oxide layer. This was shown in work performed by Dong and Li (2000a). The latter mechanism of detachment would form small craters in the surface of the oxidised Ti-64 samples, and would result in small oxide particles. This is shown in Figure 74 by the white arrow.

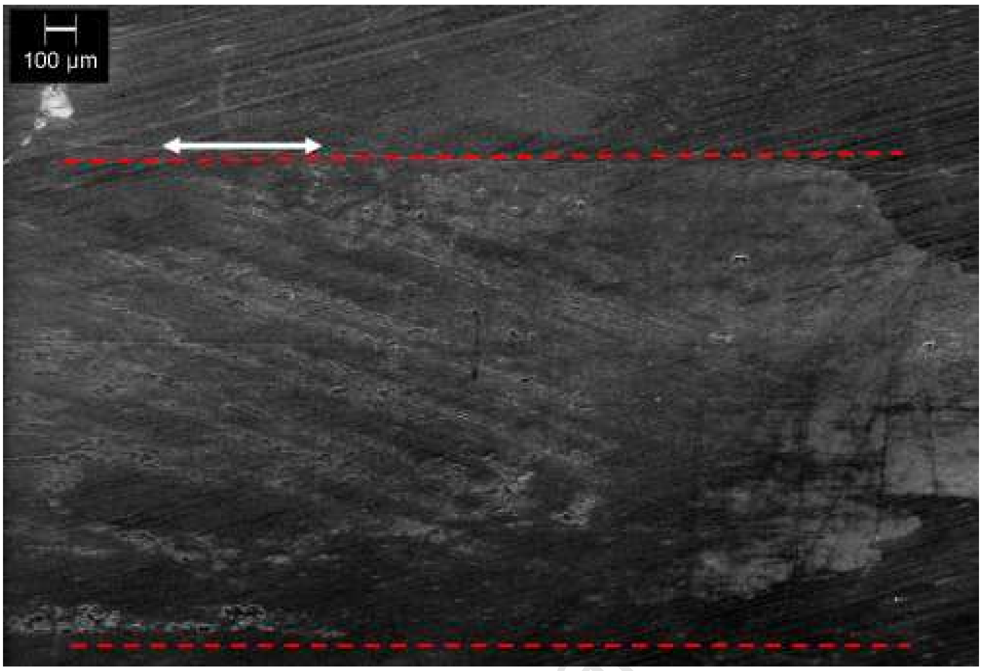

Figure 73: Wear track on the surface of a Ox(600)[Pol] sample after a sliding distance of 2400m.

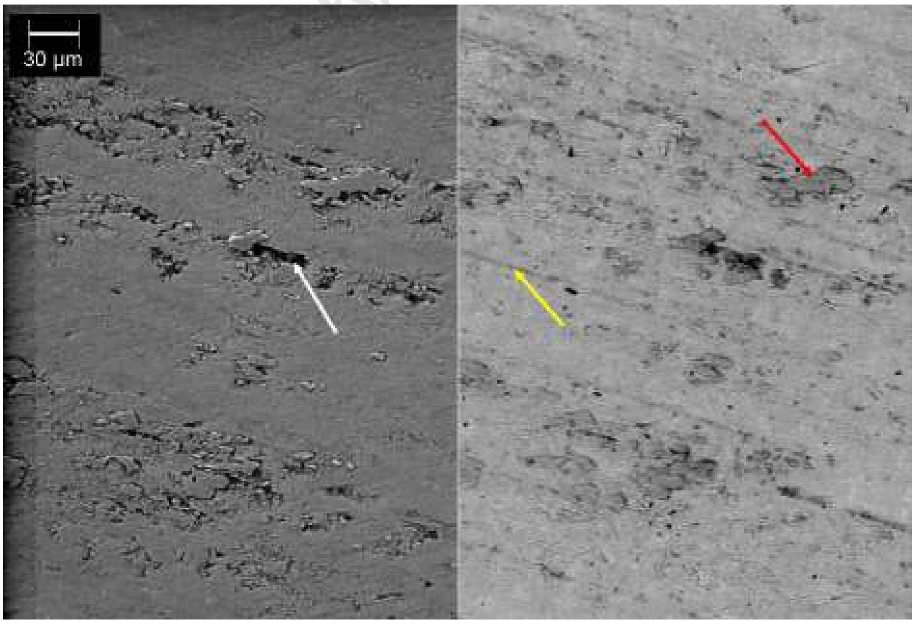

Figure 74: Secondary image of a section of the wear track of the Ox(600)[Pol] sample (left) and the backscatter electron image of the same region (right).

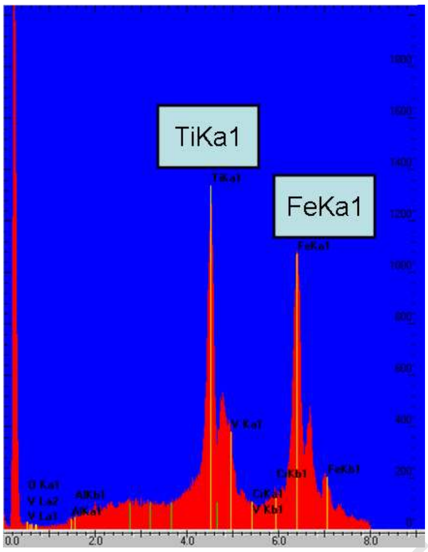

Figure 75: EDS scan of the deposited material found on the surface of the wear scar for the Ox(600)[Pol] condition.

7.3 Friction Coefficients

Frictional data was measured with a load cell connected in parallel with the sliding shuttle. This was captured and converted to frictional coefficient plots as function of sliding distance. Frictional data was captured for the 2400m tests of all the specimens to monitor the change in frictional response of the mated materials. For each treatment condition four frictional coefficient plots are produced. One representative plot of each specimen type is shown in Figure 76, the rest can be found in Appendix A. A 3-D representation of this data was taken to compare trends between treatment types. From these plots the degree of fluctuation, run-in phase, steady state phase and any distinct frictional characteristic is monitored. Of particular importance is assessing if the frictional response shows any signs of a surface layer being compromised, allowing the pin to wear against untreated Ti-64. A comparison of all the frictional data for each test and all treatment conditions is shown in Table 14.

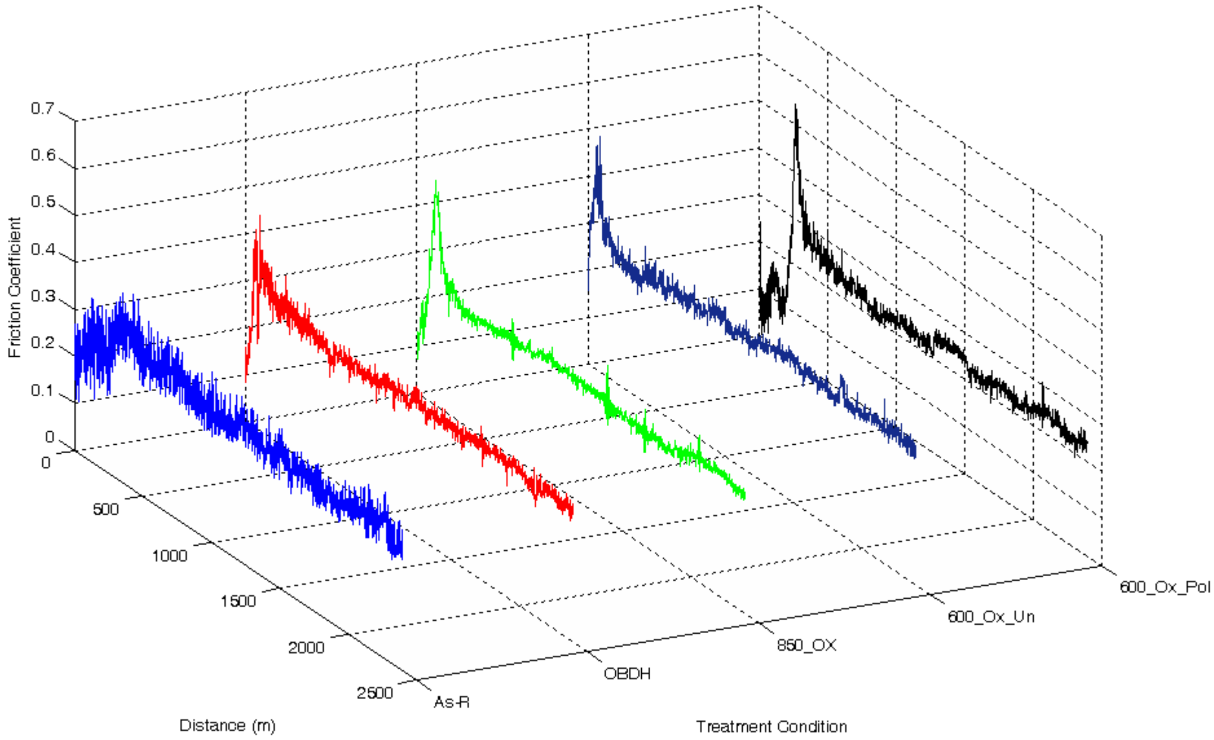

Figure 76: Frictional coefficient plots of the various conditions for the Ti-64 specimens.

Treatment	Test	Steady State Mean	Standard Deviation
As-R	1	0.28	0.02
	2	0.26	0.03
	3	0.31	0.02
	4	0.29	0.01
OBDH	1	0.28	0.01
	2	0.26	0.02
	3	0.27	0.01
	4	0.28	0.01
850_Ox	1	0.25	0.01
	2	0.27	0.01
	3	0.27	0.01
	4	0.28	0.01
600_Ox_Un	1	0.28	0.02
	2	0.29	0.01
	3	0.29	0.01
	4	0.29	0.01
600_Ox_Pol	1	0.24	0.01
	2	0.23	0.02
	3	0.20	0.01
	4	0.20	0.01

Table 14: Frictional data comparison of all the treatment conditions for the Ti-64 specimens worn through a distance of 2400m.

7.3.1 The Untreated Ti-64 Samples

The ASR condition shows a run-in phase that initiates at a level of between 0.18 and 0.22 with a sharp increase to about 0.35 at 250m. After this peak there is a steady decrease until 500m, after which steady state is reached at *ca* 0.28. When comparing all the plots for the ASR samples a range 0.26-0.31 is obtained for the frictional coefficient plots. The ASR frictional coefficient plots are characterised by large fluctuations even once steady state is reached. The untreated condition of Ti-64 showed the highest volume loss for the counter-face, and the second highest volume loss for the steel balls. The undesirable wear performance of these samples is the reason why surface modification techniques have been employed. During the run-in phase the increase until steady state can be attributed to various mechanisms occurring at the mated surfaces. The main cause of wear during this period and the subsequent increase it has on the friction experienced is that of micro-ploughing. This is due to the fact that the steel ball is much harder than the untreated Ti-64 samples and during sliding motion the asperities of the ball surface plough into the surface of the softer Ti-64 specimen. Apart from removing material from the softer surface, the ploughing causes a work hardening effect in both surfaces. The micro-hardness measurements at a depth of 20µm below the wear scar showed a maximum increase in strength in the Ti-64 by 20%. Wear tests performed by Alam and Haseeb (2002), in which Ti-64 was mated against hardened steel in a pin-on-disk arrangement, showed a similar plastically deformed zone. Although testing conditions differed, the zone that was formed is clearly shown in a cross-section of the wear track, and differs from the underlying parent material by distinct grain variation. This micrograph is shown in Figure 77.

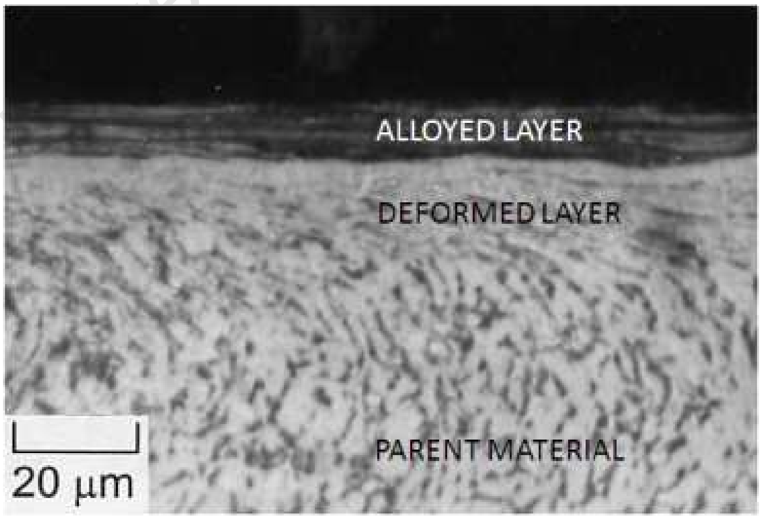

Figure 77: Cross-sectional view of a wear scar, showing the alloyed layer, plastically deformed layer and the parent material (Alam& Haseeb 2002).

A third layer was found above this plastically deformed area, and was comprised of a compositional mix of material from the Ti-64 counter-face and the steel pin. This is consistent with deposited material found on the surface of the ASR samples in the present study. The increase in strength observed for the deformed zone occurs during the run-in phase of the test until a steady state is reached for surface hardness. After this run-in phase various characteristics of the worn areas stabilise and become constant. This is observed for the deformed layer as measurements taken at 500m, 1000m and 2400m showed similar hardness values for the work hardened area at the same depths. However at 200m this increase is not as apparent and only a marginal increase of approximately 7% is observed. This shows that the plastic deformation zone that occurs beneath the wear scar is formed during the run-in period. As the test progresses into the run-in phase the strength of the deformed layer is increasing and this causes a rise in the shear strength of the material resulting in an increase in the friction. Another characteristic that reduces in deviation is the fluctuation of the friction coefficient around the steady state mean. During the run-in phase large fluctuations occur and this is still apparent during the steady state phase but to a lower degree in comparison. However when compared to the other friction coefficient plots of the various treatments it is clearly seen that the untreated condition exhibits much larger fluctuations in the friction coefficient value. This is characteristic of a mated pair in which more severe interactions occur between surface asperities and large degrees of plastic deformation occur in the softer material. Stick-slip is a common cause of these fluctuations and this phenomenon was clearly seen for the untreated samples.

7.3.2 The OBDH samples

A similar trend is observed in the frictional coefficient plots of the OBDH samples. The run-in phase initiates at *ca* 0.15 and shows a sharp increase. This peak reaches a height of 0.37 after *ca* 280m and is followed by a steady decrease until steady state is reached. Steady state initiates after a distance of 500m, and the frictional coefficient data fluctuates around a value of 0.28. Although the OBDH samples experience high degrees of frictional fluctuations, it is much lower than that of the ASR samples. Generally for a situation that involves metal/metal sliding contact, especially for a harder material against a softer one, large fluctuations in the frictional coefficient is expected. This is due to high levels of plastic deformation occurring and ploughing at the surfaces and the occurrence of stick-slip. However as seen in previous sections the OBDH samples experience lower degrees of wear than the ASR samples. This is due to the fact that the OBDH samples have been hardened. Friction coefficient plots for AISI H13 steel hardened to two different levels i.e. 460Hv and 525Hv were compared by Viafara and Sinatora (2009). These plots showed that although both hardened states reached similar steady state values that the harder condition produced a friction coefficient plot with a much lower degree of fluctuations. This was attributed to the change in wear mechanisms between the two states. The low hardness state showed severe wear in the form of delamination and plastic deformation dominated wear. In comparison to this the hardened state showed a mild wear regime dominated by oxidative wear. In the present study, OBDH specimens exhibited similar friction coefficient plots as that for the ASR samples; however a much lower degree of fluctuation is seen for the OBDH tests. This is due to little or no stick slip being observed on the worn areas of these samples. Although the OBDH samples had a higher surface hardness than the untreated condition mechanisms of wear still involved micro-ploughing, material transfer, delamination and adhesive removal of particles. Similarly, a plastically deformed zone was found at a depth of 20µm below the surface of the wear scar. The zone, as shown by Figure 53, shows an increase in the strength of the material up to 500m thereafter stabilising around a mean value.

7.3.3 Air oxidation samples

All the oxide treated samples exhibit a sharp rise in the friction coefficient during the run-in phase followed by a steep drop until steady state is achieved. The initial hypothesis for this distinct rise to approximately 0.45 (and above for 600℃ unpolished) was that the protective oxide layer was being worn through. However profilometry analysis showed that this was not occurring. No measurable wear track could be detected for any oxide treated sample and SEM analysis of the worn regions showed that large degrees of deposited material existed on the surface which acted to protect the underlying oxide.

The oxide specimens all show a large reduction in the degree of frictional fluctuations when compared to the ASR and OBDH samples. This is expected as the interaction has changed form a metal/metal contacting surface to that of a ceramic/metal interface, which experiences different wear mechanisms at the surface. It is seen that the Ox850 samples start the run-in phase as low as 0.1 followed by a sharp increase to 0.4 which is reached after about 130m. Thereafter there is a sharp decrease until steady state is reached after 300m at a value of 0.28. Similar trends are observed for the Ox(600)[U] and Ox(600)[Pol]. The latter samples start the run-in phase at 0.15 and the sharp increase results in a peak which is reached after 130m, the sudden drop results in a steady state being reached after 250m at 0.28. The Ox(600)[Pol] samples showed a slightly different scenario for steady state conditions. Although the basic trend of the plot was similar to that of the Ox(600)[U] treated samples the steady state stabilised at a lower frictional coefficient value than any of the other Ti-64 samples, treated and untreated. As apposed to the 0.28 steady state condition experienced by the other samples, the Ox(600)[Pol] samples showed a steady state as low as 0.2. It was originally hypothesised that this highly polished oxide resulted in a different type of wear scenario at the contacting surface, which caused the lower tangential frictional forces being experienced. SEM analysis shows that the wear track contained small areas of deposited material. However these deposited areas are of a much lower degree than the other oxidised treated samples (Ox850 and Ox600[Pol]). Tangential forces experienced between these oxide/steel interfaces are lower than that for a steel/steel interface and thus a lower frictional coefficient is observed for the former condition. This was confirmed by work performed by Dong and Bell (2000a). It was assumed that a lower degree of deposited material existed on the oxide surface; sufficiently low to allow large areas of the oxide to remain exposed, thus allowing much more oxide/steel interaction. This is shown in Figure 74 which shows the low level of material transfer that occurred on the surface of the Ox600[Pol]. Backscatter shows that the small transfer material differs from the surrounding oxide and EDS analysis of this material, Figure 75, shows that it consists of a large degree of Fe. The information obtained confirms the assumption that this specific treatment condition exhibits lower steady state friction coefficient values due to the higher degree of contact between the polished oxide and the steel ball; a mated pair which generally exhibits lower friction coefficient values. Although the other oxide samples (Ox850 and Ox600[Pol]) produce oxide/steel interfaces, the deposited material (with a high Fe content) leads to a large degree of metal/metal interactions. This causes steady state friction coefficient values stabilising close to that observed for the ASR and OBDH samples. What is distinctive between the various plots is the dramatic decrease in fluctuation of the steady state frictional coefficient when the oxide treated samples are compared to that of the untreated and OBDH samples. The result is due to lower degrees of plastic deformation wear occurring in the former samples as seen in previous sections. As was shown, the treated samples showed an improvement in the level of volume loss that occurred as a function of sliding distance when compared to the ASR condition. This result however could not be extracted from the friction coefficient plots of the different treatments. Although dissimilar plots were seen for the different samples, no conclusive result regarding wear performance could be deduced if consideration was only given to analysis of the friction plots.

A plot of the steady state coefficients as a function of total specific wear rates are shown in Figure 78. The untreated, OBDH, Ox850 and the Ox600[Pol] samples are all within a range of 0.03 with respect to their coefficient of friction values however the total wear rate experienced by these mated pairs are vastly different. This graph emphasises the last point, that no actual conclusion regarding wear performance can be extracted from the derived friction coefficient values.

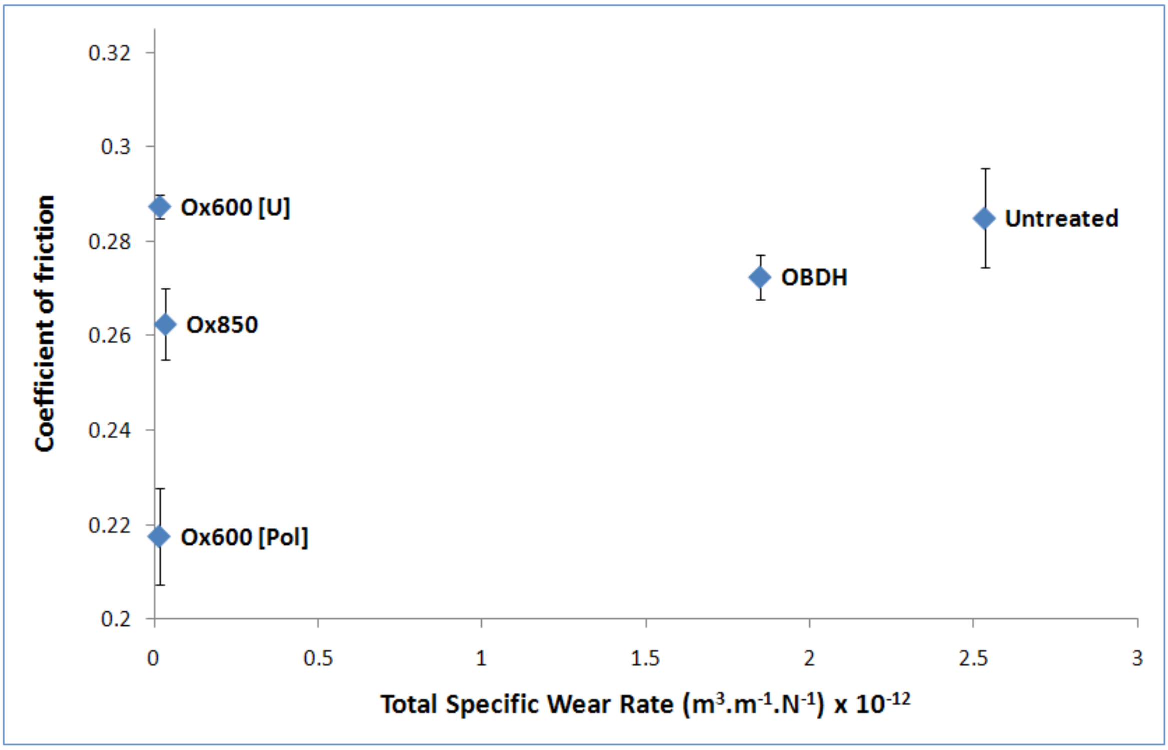

Figure 78: Steady state coefficient of friction plots for the different Ti-64 samples as a function of the specific wear rate after a sliding distance of 2400m.

Friction coefficient plots were also analysed to assess whether a surface layer had been compromised during a wear test. This would result in a sudden change in the progression of the plot. An example of such a response is shown in Figure 79 (Taktak & Akbulut 2007), which are the comparative plots of friction coefficient as a function of sliding distance for untreated Ti-64 samples and samples surface modified by the process of plasma nitriding.

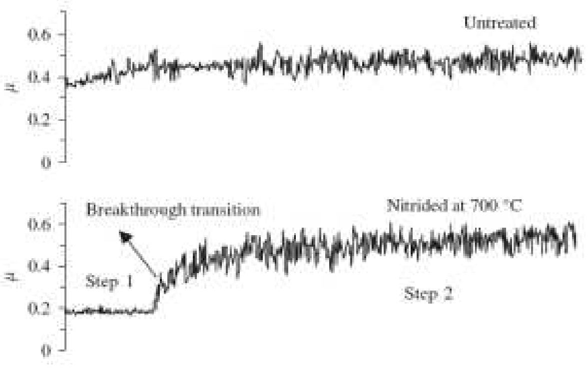

Figure 79: Variation in the frictional coefficient as a function of distance for the untreated condition (top) and the 115itride sample (bottom) (Taktak & Akbulut 2007).

These samples form a surface TiN layer followed by a diffusion case of N in Ti to form a stabilised α-Ti zone similar to that of the ODZ found in the treated samples performed. It can be seen that there is a clear transition in the friction coefficient plot and its fluctuations when the surface affected regions are compromised and wear proceeds into the unaffected Ti-64 zone after about 100 cycles. In this case the wear testing resulted in a penetration of the surface modified layer. This kind of transition is not observed in the oxidised or the OBDH samples. Another important fact is that if either the layers (oxide layer or the ODZ) were worn through completely to the unaffected material the characteristic fluctuations and stick-slip mechanisms observed in the untreated Ti-64 samples would clearly "evolve" after this penetration. This, however, is not observed in the friction coefficient plots or the wear mechanisms examined. For the specific parameters performed in these tests it has thus been shown that no surface layer was completely compromised.

7.3.4 The Pin-on-Disk comparison

Cylindrical Ti-64 samples were tested on a pin-on-disk rig to investigate the frictional response under this constant sliding condition. For these tests the dynamic friction coefficient was analysed. As the pin-on-disk was a highly accurate calibrated CSM tribometer the results were used to validate the relationships seen in the ASR, OBDH and Ox850 samples. It was originally hypothesised that a lower steady state friction coefficient would be experienced for samples that showed lower volume losses. However, it was shown that this was not the case and that even the oxide samples which exhibited dramatically lower volume losses when compared to the ASR and OBDH samples showed similar steady state friction coefficients. The main purpose of the pin-on-disk tests was to confirm whether this was indeed the case. The frictional coefficient plots for the ASR, OBDH and Ox850 samples tested on the pin-on-disk tribometer are shown in Figure 80, Figure 81 and Figure 82. The graphs have been plotted using the same y-axis range.

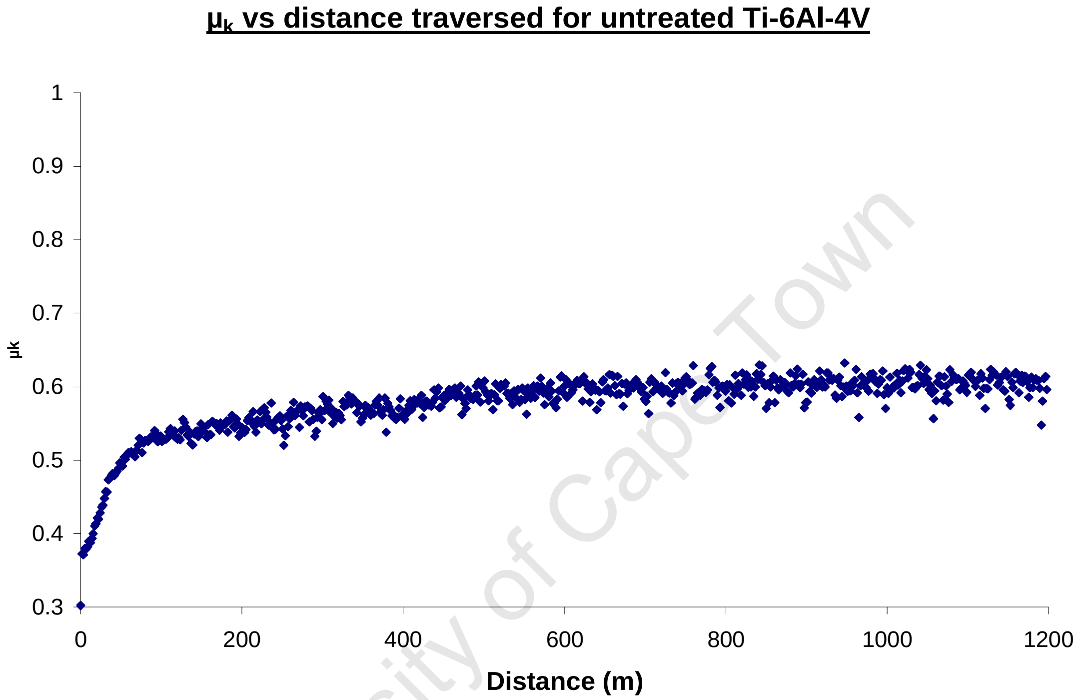

Figure 80: Friction coefficient as a function of distance plot for the untreated condition. Wear tests performed on the pin-on-disk tribometer.

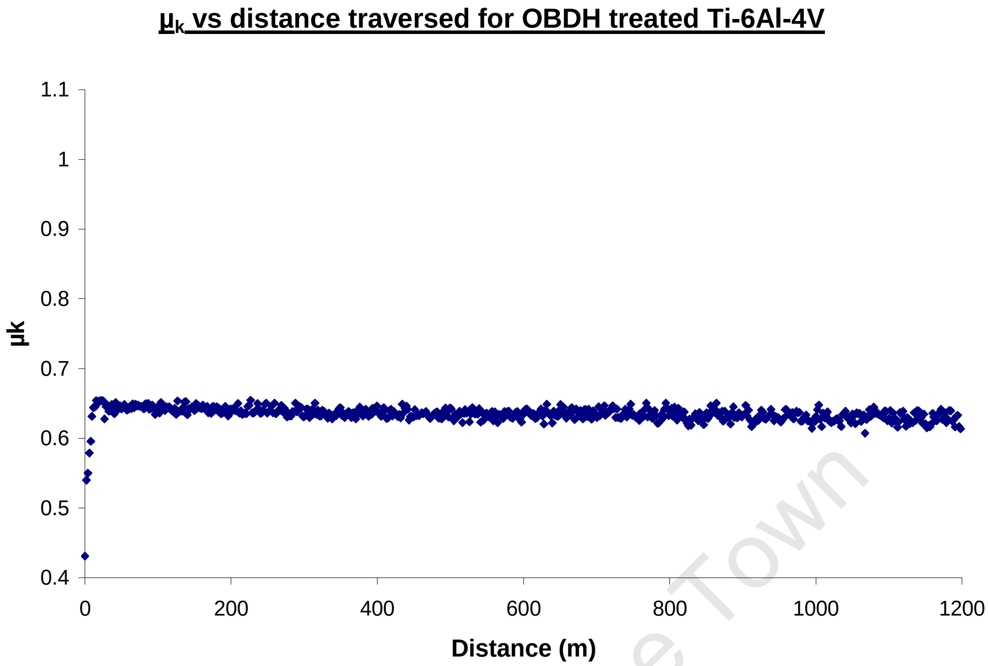

Figure 81: Friction coefficient as a function of distance plot for the OBDH treated samples. Wear tests performed on the pin-on-disk tribometer.

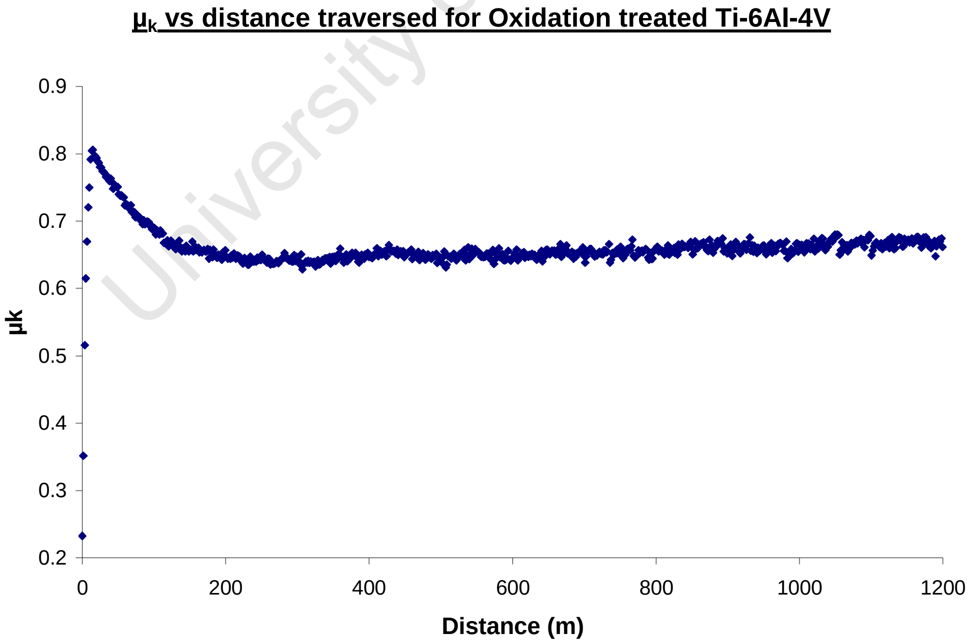

Figure 82: Friction coefficient as a function of distance plot for the samples oxidised at 850°C. Wear tests performed on the pin-on-disk tribometer.

The trends of these plots resemble that of the tests performed by the linear reciprocating rig and steady state μ values of all the tests tend toward the range of 0.6-0.65. The ASR samples showed a run-in period of 500m after which steady state is reached. The OBDH samples showed a sharp rise initially and then a steady decrease until steady state after 570m. Ox850 samples showed a sharp increase followed by a sharp decrease after a sliding distance of 25m and steady state was reached after 200m. Also of importance is that the untreated condition shows a much greater deviation around the steady state friction coefficient, when compared to the OBDH and Ox850 samples. These fluctuations are greatly reduced in the OBDH and the oxide tests. From the comparison between the frictional data of the two rigs it is apparent that the degree of fluctuations decreases going from ASR to OBDH and Ox850. The length of the run-in phases for the different treatments is also similar for both rigs. The samples tested on the pin-on-disk tribometer were tested under a load of 5N through a distance of 1200m. The volume losses under these conditions for the ASR and OBDH samples for both rigs are shown in Figure 83.

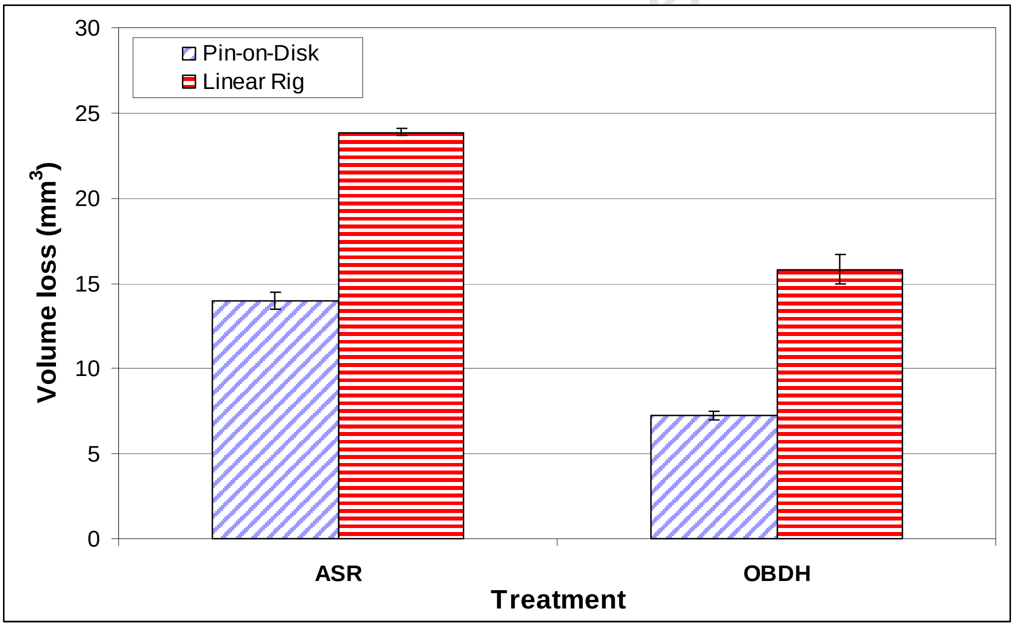

Figure 83: Volume loss of the ASR and OBDH samples tested under a 5N load after a 1200m sliding distance, for both the pin-on-disk and linear reciprocating rig.

The oxide sample tested on the pin-on-disk tribometer again showed no measurable wear track width and thus no volume loss for the Ox850 is plotted. It was determined from the pin-on-disk tests that although lower volume losses occur for the OBDH sample when compared to the ASR, the samples tested on the pin-on-disk tribometer showed lower volume losses than those tested on the linear reciprocating rig under the same conditions.

Comparing steady state friction coefficient values achieved for the respective tests on the different testing rigs, it is clear that tests performed on the pin-on-disk reach higher friction coefficient values than for the tests executed on the reciprocating rig. This phenomenon is not quite understood. It was initially assumed that frictional heating was of a higher degree in the pin-on-disk tests, leading to a drop in the shear strength of the materials involved. This would cause an increase in the friction coefficient value. This increase would be associated with higher degrees of wear occurring on both surfaces. It was calculated that at a testing radius of 8mm for the pin-on-disk tests that a given point would reach itself 60% faster compared to a point on the linear tests. Thus sliding of the surfaces would occur faster resulting in a higher surface temperature. However, from Figure 83, it is shown that under the same load and distance traversed lower material losses occur for Ti-64 samples tested on the pin-on-disk. This disproves the assumption in this case that a drop in the shear strength of the materials involved is causing the dramatic increase in the friction coefficient values.

A more plausible reason for the difference in friction values could relate to the geometry of the two testing rigs and the relative position of the load cell. The comparison of the two designs has not been analysed in detail and is beyond the scope of the present work.

8 CONCLUSIONS

8.1 OBDH treatment produces hardened case

The OBDH treatment, which consisted of a two step process, was successful in developing a hardened α-phase case below the surface. The diffusion zone of oxygen penetrated to a depth of 450µm before reaching hardness conditions of the bulk material; this is much deeper than the ODZ produced by either oxidation processes i.e. 100µm. The hardness profile decreased as the depth below surface was increased which is attributed to the amount of oxygen diffusion that occurred. The trend being that as the degree of oxygen within the lattice increases, so does the hardness of the material.

8.2 Surface hardness increased through treatments

Surface hardness increased from an untreated state of 347Hv to 775Hv after the OBDH treatment. The OBDH samples were surface ground to a metallic finish lowering the hardness to 537Hv. Samples oxidised at 850℃ in an air environment showed the greatest improvement in the surface hardness; the treatment produced a surface hardness of 1004Hv. The 600℃ oxidation treatment w as successful in producing a surface hardness of 719Hv.

8.3 Friction coefficient provides no scope for wear assessment

Friction coefficient data provided no valuable insight into the actual wear performance of the various conditions. As all of the treatments produce a steady state friction coefficient value within close range of each other (aside from the polished 600℃ samples), no ranking system could be produced to categorise the wear performance of the treatments based on friction coefficient plots. It can be noted however that certain assumptions could be made on particular wear mechanisms by analysis of the degree of fluctuation in the actual plots i.e. stick slip and plastic deformation dominated wear. These deductions however had to be confirmed by examination of the specimens (by light microscopy and SEM) after testing was performed. It is thus realised that wear performance cannot be determined on the basis of analysing the produced friction coefficient plots alone.

8.4 OBDH improves wear resistance

Initially it was hypothesised that the increased surface hardness achieved after the OBDH process would increase the wear performance of the Ti-64 samples. This was proven to be the case. The OBDH samples showed a higher resistance to wear than the untreated condition showing a decrease in volume loss after 2400m by 25%. However when compared to the oxidised samples the OBDH clearly performed poorer. No measurable depth could be found for any of the oxide samples, although using SEM analysis it was shown that small degrees of wear did occur on the surface in the form of light abrasive grooves and craters. This was observed for all oxide samples.

As no measurable wear was found for the oxidised samples, analysis of the wear loss by the steel balls provided separate insight into the wear performance. As minimal material loss from either mated surface would be preferred it is shown that the polished condition for 600℃ oxidised samples performs the best. Although the OBDH condition shows the lowest volume loss for the ball samples, no measurable volume loss occurred for the 600℃ polished counter-faces.

8.5 Hardness profile of the OBDH samples directly affects the wear performance

It was originally hypothesised that wear testing at various depths into the hardness profile of the OBDH samples would yield different wear performance levels. This hypothesis was proved plausible by the results obtained. Lower volume losses were obtained for the OBDH[U] samples which were tested at a surface hardness of 753Hv as apposed to the OBDH samples of 537Hv at a 50µm depth. Wear mechanisms also differed for the two sample types. OBDH samples showed clear signs of abrasive wear, in the form of deep grooves on the wear surface (ploughing), delamination wear and the deposited material on the pin surface had high quantities of Ti. These wear mechanism consequently lead to the higher volume losses for the OBDH samples. OBDH[U] samples however showed a much higher degree of deposited material along the surface of the wear track, the track itself having a smooth appearance with no sign of the degree of ploughing seen in the OBDH samples. The deposited material on the wear surface of the counter-face showed high concentrations of Fe, which meant that a much higher degree of pin material transfer was occurring for these samples. When comparing the results shown in Figure 47 and Figure 52 it is clear that the OBDH[U] samples showed a volume loss 4 times lower than the ASR condition after a 2400m sliding distance as apposed to the 30% reduction seen for the OBDH and ASR comparison.

8.6 Wear mechanisms of the different conditions

The untreated and OBDH samples tested showed signs of micro-ploughing, adhesive wear and wear particle formation leading to three-body abrasion which were all characteristic of the severe wear regime. The formation of the wear particles is attributed to asperity removal from either surface or pulverising of deposited material. The Ox850 and Ox(600)[U] samples showed large amounts of material deposition onto the counter-face surface which served to protect the underlying oxide. The oxide surfaces of the Ox850 samples were subject to small degrees of wear mainly attributed to propagation of cracks previously existing as pores in the oxide or cracks formed during the wear test. Strong adhesive forces cause removal of fragments or asperities of the oxide. The Ox(600)[Pol] samples show a much lower degree of material deposition relative to the other oxide treatments. Wear of this polished surface was mainly attributed to detachment of oxide fragments due to high adhesive forces causing crack propagation and finally segment removal.

As was seen when assessing the wear rates for the mated couple and that for the steel balls (Figure 49and Figure 50) no relationship existed between the wear rates and the surface hardness of the Ti-64 samples. As a result the data did not obey the Archard wear equation. This was as a result of the varying wear mechanisms that occurred at the contacting surfaces as explained above.

9 REFERENCE LIST

Alam, O. (Md). & Haseeb, A.S.M.A. (2002). Response of Ti-6Al-4V and Ti-24Al-11Nb Alloys to Dry Sliding Wear Against Hardened Steel. Tribology International, 35, pp. 357-362.

ASM Aerospace Specification Metals Inc. (n.d.). Titanium Grade 1. Available from: http://asm.matweb.com/search/SpecificMaterial.asp?bassnum=MTU010 . (Accessed 02 Jan 2009).

Boyer, R.R. (Editor). (1998). Titanium and Titanium Alloys. In Metals Handbook Desk Edition 2nd edtion. Materials Park: ASM International

Brooks, C.R. (1982). Heat Treatments, Structure and Properties of Non-Ferrous Alloys. Metals Park: ASM international.

Burnell Gray, J.S. (1994). Air Oxidation Behaviour of Ti-6Al-4V between 650 and 850ºC. Corrosion Science, 36, 4, pp. 631-642.

CALPHAD (Computer Coupling of Phase Diagrams and thermochemistry) www.calphad.com (2009). Titanium-Aluminium Phase Diagram. Available from: http://www.calphad.com/titanium-aluminum.html (Accessed 10 November 2010).

Chen, T.J., Zhang, Z., Ma, Y., Li, Y., Hao, Y. (2007). Friction and Wear Properties of Permanent Mould Cast AZ91D Magnesium Alloy. Materials Science and Technology, 8, 23, pp. 937 – 944.

Xu, C. & Gao, W. (2000). Pilling-Bedworth Ratio for the Oxidation of Alloys. Mat Res Innovat, 3, pp. 231-235.

Ding, R., Guo, Z.X., & Wilson, A. (2001). Microstructural Evolution of Ti-6Al-4V during Thermomechanical Processing. Materials Science and Engineering, A327, pp. 233-245.

Donachie, M.J. (Editor). (1988). Titanium: A Technical Guide. Metals Park: ASM International

Dong, H., Bloyce, A. Morton, P.H. & Bell, T. (2001). Surface oxidation of a titanium or titanium alloy article, US Patent 06210807

Dong, H. & Bell, T. (2000a). Enhanced Wear Resistance of Tianium Surfaces by a New Thermal Oxidation Treatment. Wear, 238, pp. 131-137.

Dong, H. & Li, X.Y. (2000b). Oxygen Boost Diffusion for the Deep Case Hardening of Titanium Alloys. Materials Science and Engineering, A280, pp. 303-310.

Dryden Flight Research Centre. (1992). SR-71 Blackbird: 3 SR-71's on Ramp. Available from: http://www.nasa.gov/centers/dryden/multimedia/imagegallery/SR-71/index.html (Accessed 12 September 2009).

Edwards, L. & Endean, M. (1990). Manufacturing with Materials. England: Open University, Materials Dept Butterworths

Excerpt from JISB0601. (1994). Surface Roughness. Available from: http://www.misumiamerica.com/CategoryImages/Metric_2009_pdf/p2839.pdf (Accessed 12 July 2009).

Frangini,S., Mignone, A. & De Riccardis, F. (1994). Various aspects of the air oxidation behaviour of a Ti6Al4V alloy at temperatures in the range 600-700ºC. Journal of Materials Science, 29, pp. 714-720.

Gahr, K-H.Z. (1987). Microstructure and Wear of Materials. Amsterdam: Elsevier Science Publishers

Garbcz, H. & Lewandowska, M.(2003). Microstructural Changes during Oxidation of Titanium Alloys. Materials Chmeistry and Physics, 81, pp. 542-547.

Grant, F. A. (1959). Properties of Rutile. Reviews of Modern Physics, 31, 3.

Guichelaar, Dr. P., William, R.H., Bruce, R.W., Godfrey, D., Ryason, R., Bosser, E. R., Flaherty, A. (2008). Basics of Friction. Available from: http://www.stle.org/resources/lubelearn/friction/default.aspx . (Accessed 06 December 2008).

Guleryuz, H. & Cimenoglu, H. (2009). Oxidation of Ti-6Al-4V Alloy. Journal of Alloys and Compounds, 472, pp. 241-246.

Halevy, I., Zamir, G., Winterrose, M., Sanjit, G., Grandini, C. R. & Moreno-Gobbi, A. (2010). Crystallographic structure of Ti-6Al-4V, Ti-HP and Ti-CP under High Pressure. Journal of Physics: Conference Series, 215, 012013.

Halling, J. (Editor). (1983). Principles of Tribology. London: The Macmillan Press Ltd

Housley, K.L. (2007). Black Sand: A History of Titanium. Hartford: Metal Management Aerospace Inc

Hutchings, I.M. (Editor). (1997). New Directions in Tribology. London: Mechanical Engineering Publications Limited

Hutchings, I.M. (1992). Tribology: Friction and Wear of Engineering Materials. Britain: CRC press

International Titanium Association. (2007a). Titanium: The Ultimate Choice (Brochure). USA: Broomfield

International Titanium Association. (2007b. Titanium Facts (Brochure). USA: Broomfield
Johns, S.M. (1996). Wear resistance of plasma immersion ion implanted Ti6Al4V. Surface and Coatings Technology, 85, pp. 7-14.

Krol, S., Grzesik, W., Zalisz, Z., Hepner, M. (2004). Frictional Behaviour of Oxygen Diffusion Hardened Titanium in Dry Sliding against Co-28Cr-5W-4Fe-3Ni-1Si Cobalt Alloy. Tribology International, 37, pp.633-543.

Lancaster, J.K. (1990). Wear, 141, pp. 159

Lansdown, A.R. & Price, A.L. (1986). Materials to Resist Wear: A Guide to their Selection and Use. England: Pergamon Press Ltd

Leyens, C, & Peters, M. (Editors). (2003). Titanium and Titanium Alloys: Fundamentals and Applications. Germany: Institute of Materials Research

Long, M. & Rack, H.J. (2001). Friction behaviour of selected titanium alloys during reciprocating-sliding motion. Wear, 249, pp.158-168.

Long, M & Rack, H.J. (1998). Titanium alloys in total joint replacement—a materials science perspective. Biomaterials, 19, pp. 1621-1639.

Marumoto, K. & Hirattsuka, K. (2005). Role of Wear Particles in Severe-Mild Wear Transitions. Wear, 259, pp. 467-476.

Materials Property Data (MATWEB). (n.d.). Available from: http://www.matweb.com/index.aspx. (Accessed 25 November 2008).

Moiseyev, V.N. (2006). Titanium Alloys: Russian Aircraft and Aerospace Applications. Boca Raton: CRC Press

Molanari, A., Straffelini, G., Tesi, B. & Bacci, T. (1996). Dry sliding wear mechanism of the Ti6Al4V alloy. Wear, 208, pp. 105-112.

Perrin, B. (1994). Creep, Stick Slip and Dry Friction Mechanics: Experiments and Heuristic Model. Physical Review E, 49, 6, pp. 4973-4988.

Peterson, M.B. & Winer, W.O. (Editors). (1980). Introduction. Wear fundamentals. Materials. In Wear Control Handbook. New York: American Society of Mechanical Engineers

Pinke, P., Caplovic, L. & Kovaks, T. (n.d.). The Influence of Heat Treatment on the Microstructure of the Casted Ti-6Al-4V Titanium Alloy. Available from: http://www.kfki.hu/~anyag/Pinke_2.pdf. (Accessed 03 August 2009).

Podra, P. & Anderson, S. (1997). Wear Simulation with the Winkler Surface Model. Wear, 207, pp. 79-85.

Popp, K. & Stelter, P. (1990). Stick Slip Vibration and Chaos. Philosophical Transactions: Physical Science and Engineering, 1624, 332, pp. 89-105.

Qu, Ju & Truhan, J.J. (2006). An Efficient Method for Accurately Determining Wear Volumes of Sliders with Non-Flat Wear Scars and Compound Curvatures. Wear, 261, pp. 848-855.

Rabinowicz, E. (1995). Friction and wear of materials. 2nd ed. New York: John Wiley and Sons

Rank Taylor Hobson Ltd (n.d.) Surtronic 3P: Operating Instructions. (Booklet). England

Reidenbach, F. (1994). Volume 5: Surface Engineering of Titanium and Titanium Alloys. In ASM Handbook 10th edition. Materials Park: ASM International.

Rosenberg, S.J. & Jordan, L. (1934). J.Res. Nat. Bur. Stand, 13, pp. 267

Sarkar, A.D. (1976). Wear of Metals. Britain: A. Wheaton & Co

Siva Rama Krishana, D., Brama, Y.L. & Sun, Y. (2007). Thick Rutile Layer on Titanium for Tribological Applications. Tribology International, 40, pp. 329-334.

Smith, R., Mulliah, D., Kenny, S.D., McGee, E., Aster, R., Gruner, M. (2005). Stick Slip and Wear on Metal Surfaces. Wear, 259, pp. 459-466.

Standard Guide for Measuring and Reporting Friction Coefficients. ASTM G115. American Society for Testing and Materials, 2004

Standard Test Method for Linearly Reciprocating Ball-on-Flat Sliding Wear. ASTM G133. American Society for Testing and Materials, 1995

Standard Test Method for Wear Testing with a Pin-on-Disk Apparatus. ASTM G99, American Society for Testing and Materials, 2005.

Streicher, R.M., Weber,H., Schon,R. & Semlistch, M. (1991). New surface modification for Ti-6Al-7Nb alloy: oxygen diffusion hardening (ODH). Biomaterials, 12, pp. 125-129.

Taktak, S. & Akbulut, H. (2007). Dry wear and friction behaviour of plasma 127itride Ti-6Al-4V alloy after explosive shock treatment. Tribology International, 40, pp.423-432.

Uhlig, H. H. (1985). Corrosion and Corrosion control: An Introduction to Corrsoin Science and Engineering.New York: Wiley & Sons

Van De Velde, F., De Baets, P. & Degrieck, J. (1997). The Friction Force during Stick Slip with Velocity Reversal. Wear, 216, pp. 138-149.

Vaquila, I., Vergara, L.I., PasseggiJnr, M.C.G., Vidal, R.A. & Ferron, J. (1999). Chemical Reactions at Surfaces: Titanium Oxidation. Surface Coatings, 122, pp. 67-71.

Vaquila, I., Passeggi Jr, M.C.G. & Ferron, J. (1996). Temperature Effects in the Early Stages of Titanium Oxidation. Applied Surface Science, 93, pp. 247-253.

Viafara, C.C. & Sinatora, A. (2009). Influence of hardness of the harder body on wear regime transition in a sliding pair of steels. Wear, 267, pp. 425-432.

Velten, D., Biehl, V., Aubertin, F., Valeske, B., Possart, W., Breme, J. (2000). Preparation of TiO_2 layers on cp-Ti and Ti6Al4V by thermal and anodic oxidation and by sol-gel coating techniques and their characterization. Journal of Biomedical Materials Research, 59, pp. 18-28.

Welsh, N.C. (1965). The Dry Wear of Steels I: The General Pattern of Behaviour. The Philosophical transactions of the Royal Society, 257, pp. 31-50.

Williams, J.A. (1994). Engineering Tribology. Britain: Bookcraft (Bath) Ltd

Winkler, P.J. (Editor). (2000). Materials for Transportation Technology: Volume 1. Germany: Federation of European Materials Societies

Yazdanian, M.M., Edrisy, A. & Alpas, A.T. (2007). Vacuum sliding behaviour of thermally oxidized Ti–6Al–4V alloy. Surface and Coatings Technology, 202, pp. 1182-1188.

Zang, G. (2000). Improving IC Yield with Protective Ceramics. Available from: http://www.3d-rom.net/ProMO/Improving%20IC%20Yield.htm . (Accessed 23 June 2009).

Zhang, Z.X., Dong, H., Bell, T., Xu, T. (2007). The Effect of Treatment Condition on Boost Diffusion of Thermally Oxidised Titanium Alloy. Journal of Alloy and Compounds, 431, pp. 93-99.

Zhang, Z.X., Dong, H., Bell, T. & Xu, B.S. (2008). The Effect of Deep Case Hardening on the Tribological Behaviour of a-C:H DLC Coatings on Ti6Al4V alloy. Journal of Alloy and Compounds, 464, pp. 519-525.

Zang, S.L. & Ji, J.C.M. (2002). Slip Process of Stick-Slip Motion in the Scratching of a Polymer. Materials Science and Engineering, A344, pp. 182-189.

10 APPENDIX A

10.1 Frictional coefficient plots of tests at 2400m distance

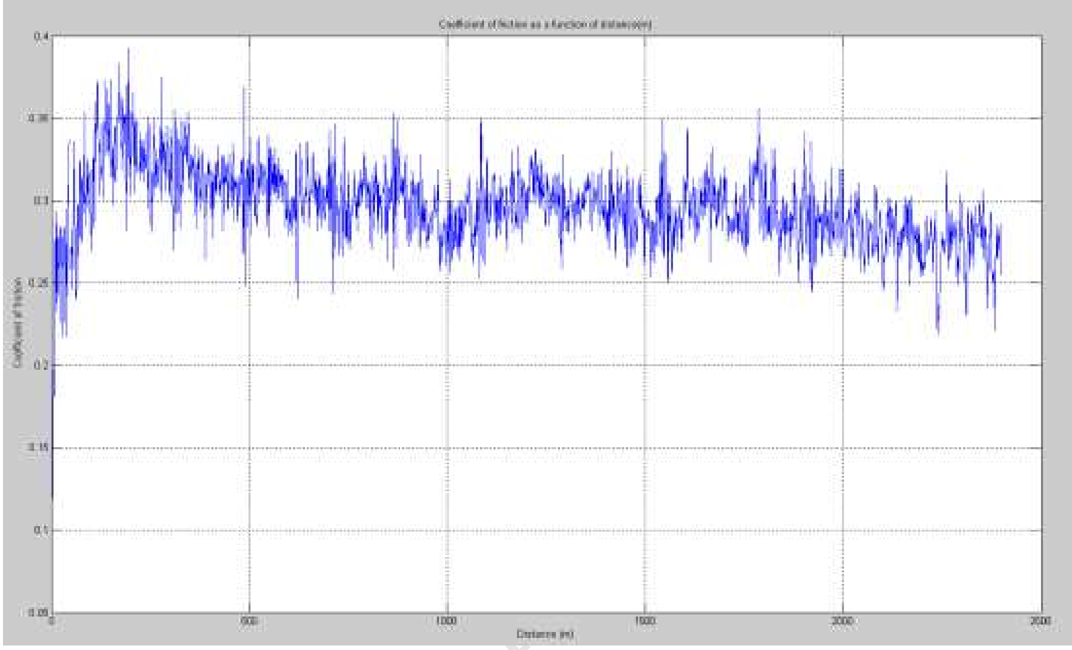

(a)

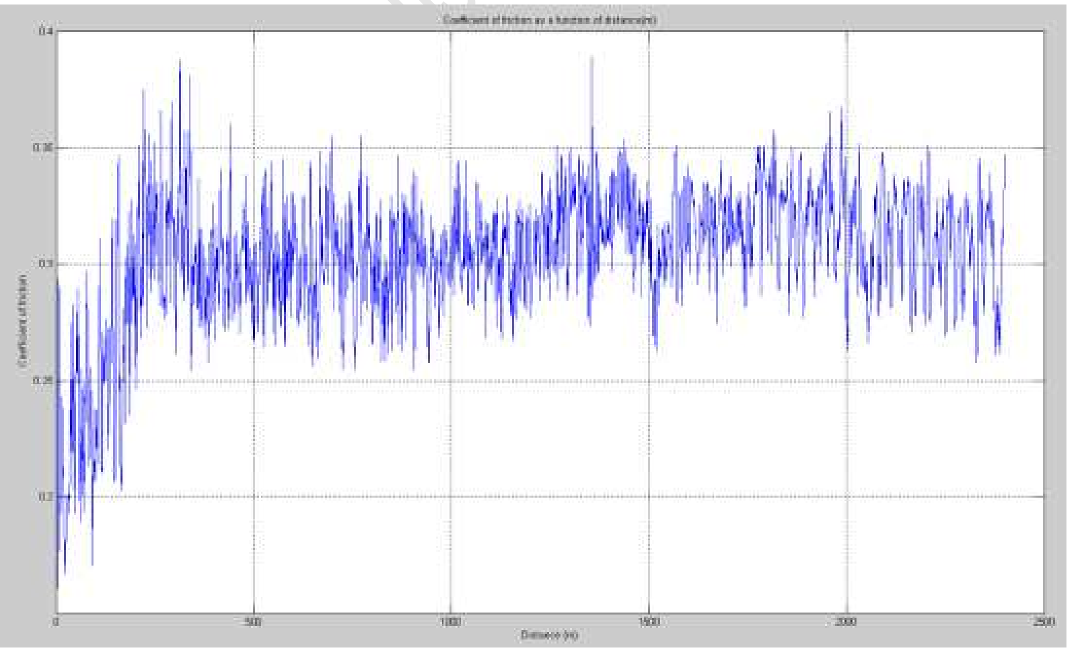

(b)

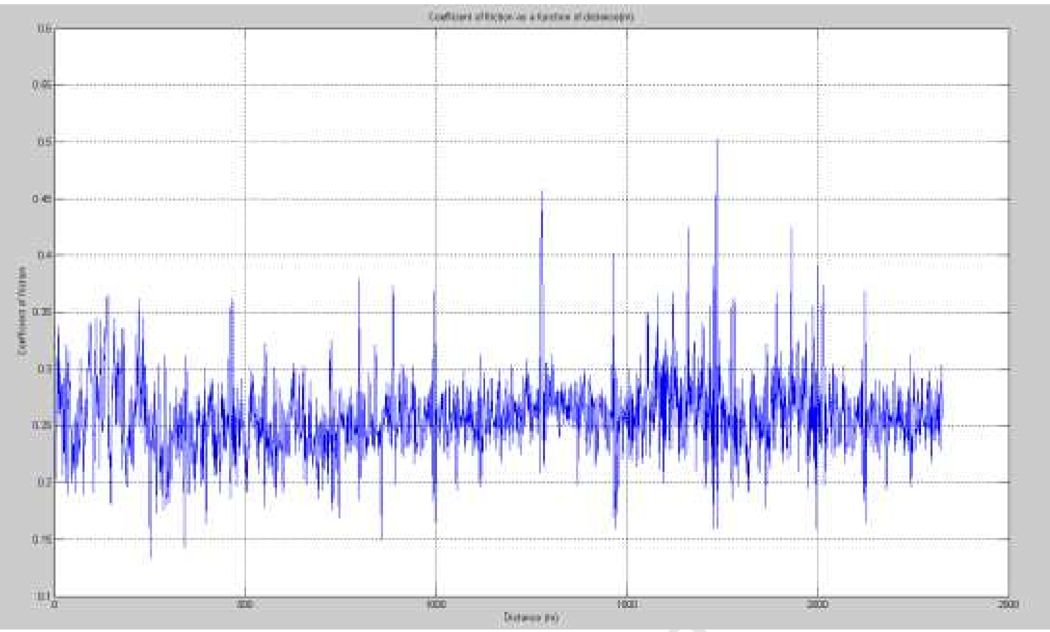

(c)

Figure 84: (a), (b) and (c) are the reciprocating tests performed for 2400m for the As-received Ti64 samples. The plots show the change in the coefficient of friction as a function of distance.

The initial run-in phase for the sample of Figure 84 (c) was not recorded. This was due to a problem in the link between the load cell and the DAQ (Data Aquisition) card.

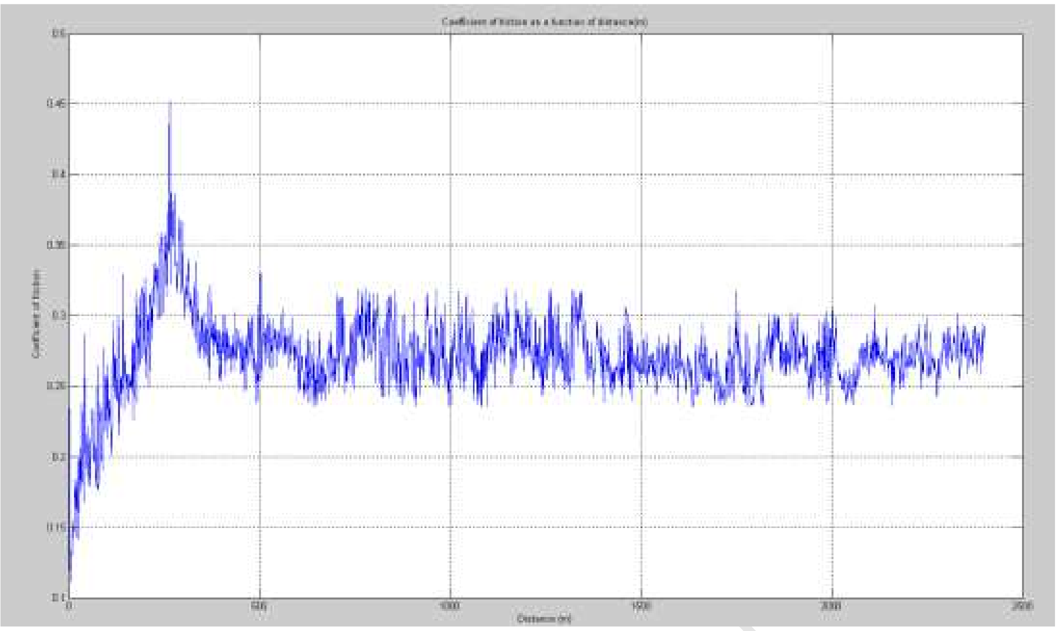
Coefficient of friction as a function of distance(m)
Coefficient of friction
Distance (m)
0.5
0.45
0.4
0.35
0.3
0.25
0.2
0.15
0.1
0
500
1000
1500
2000
2500

(a)

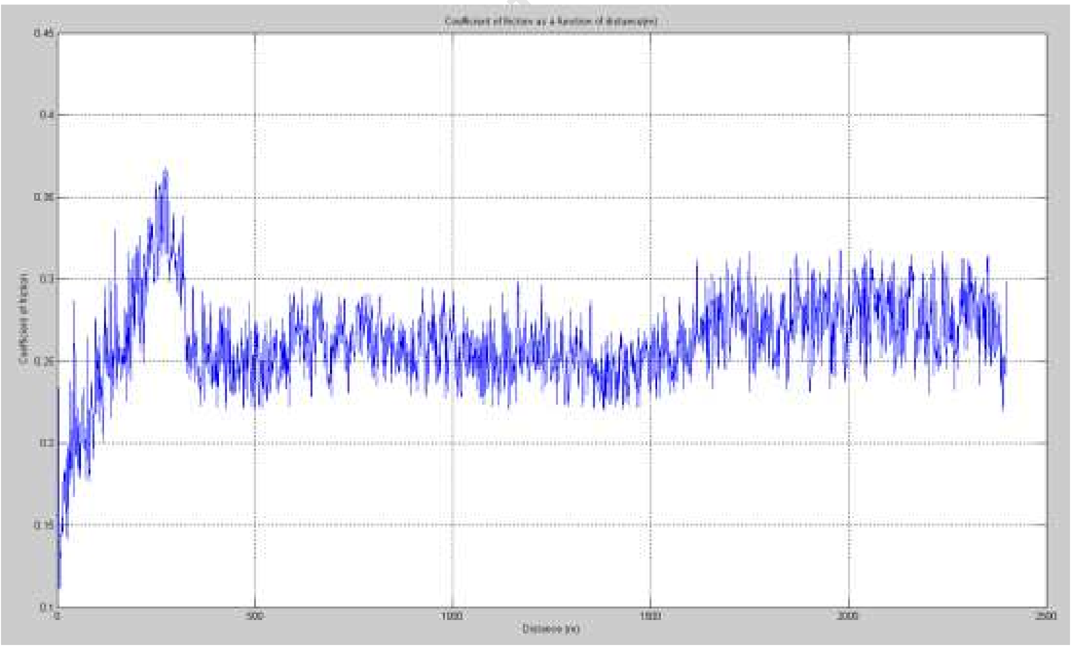
Coefficient of friction as a function of distance(m)
Coefficient of friction
Distance (m)
0.45
0.4
0.35
0.3
0.25
0.2
0.15
0.1
0
500
1000
1500
2000
2500

(b)

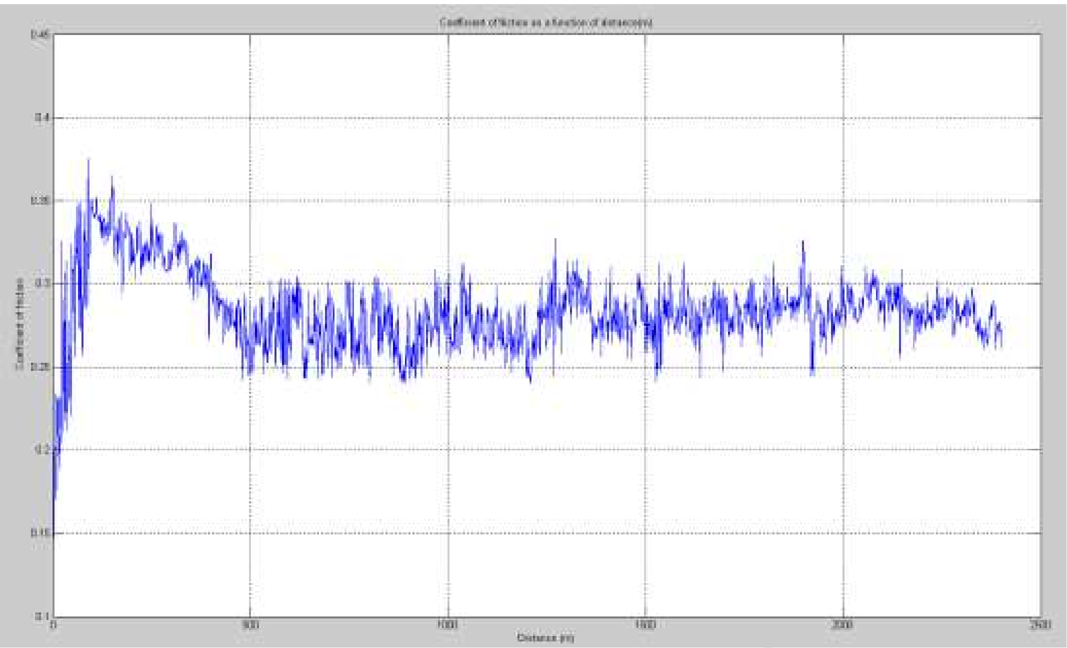

(c)

Figure 85: (a), (b) and (c) are the reciprocating tests performed for 2400m for the OBDH treated Ti64 samples. The plots show the change in the coefficient of friction as a function of distance.

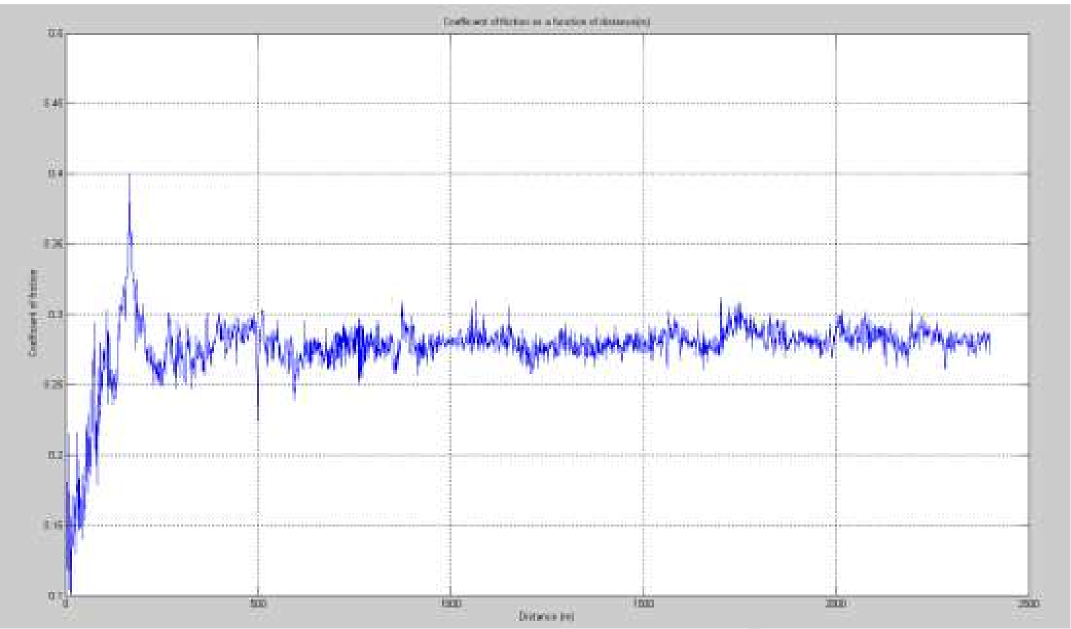
Coefficient of friction as a function of distance(m)
Coefficient of friction
Distance (m)
0.5
0.45
0.4
0.35
0.3
0.25
0.2
0.15
0.1
0
500
1000
1500
2000
2500

(a)

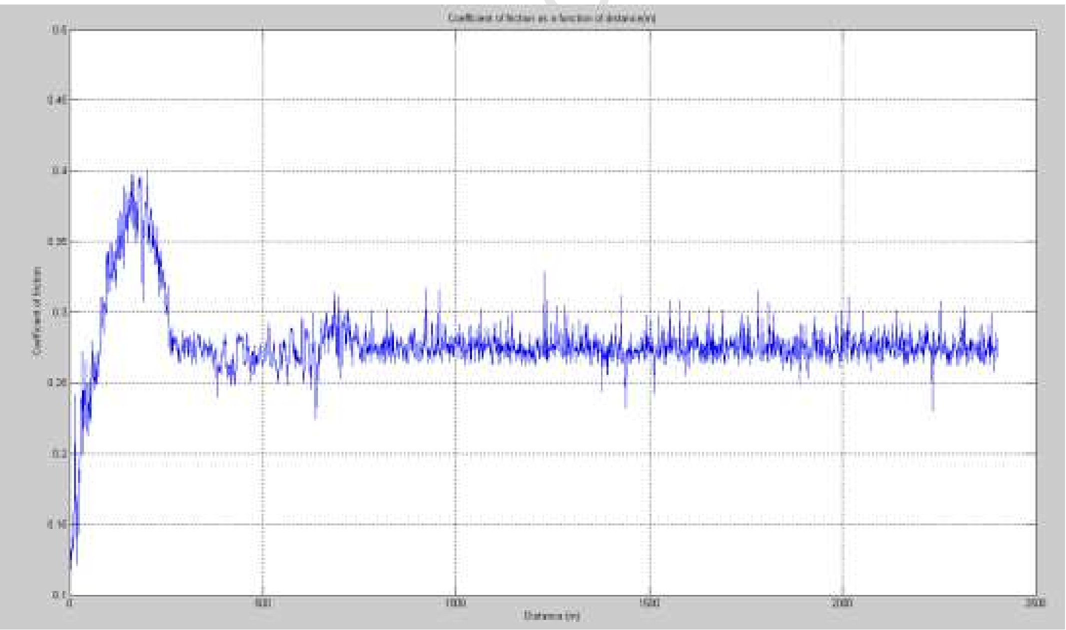
Coefficient of friction as a function of distance(m)
Coefficient of friction
Distance (m)
0.5
0.45
0.4
0.35
0.3
0.25
0.2
0.15
0.1
0
500
1000
1500
2000
2500

(b)

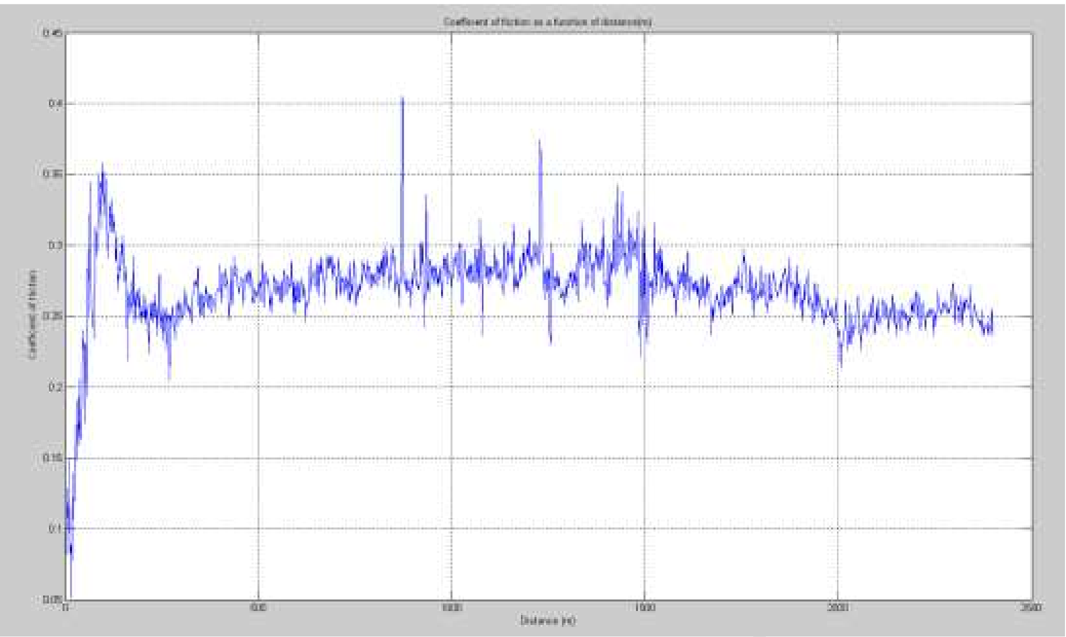

(c)

Figure 86: (a), (b) and (c) are the reciprocating tests performed for 2400m for the 850ºC oxide treated Ti64 samples. The plots show the change in the coefficient of friction as a function of distance.

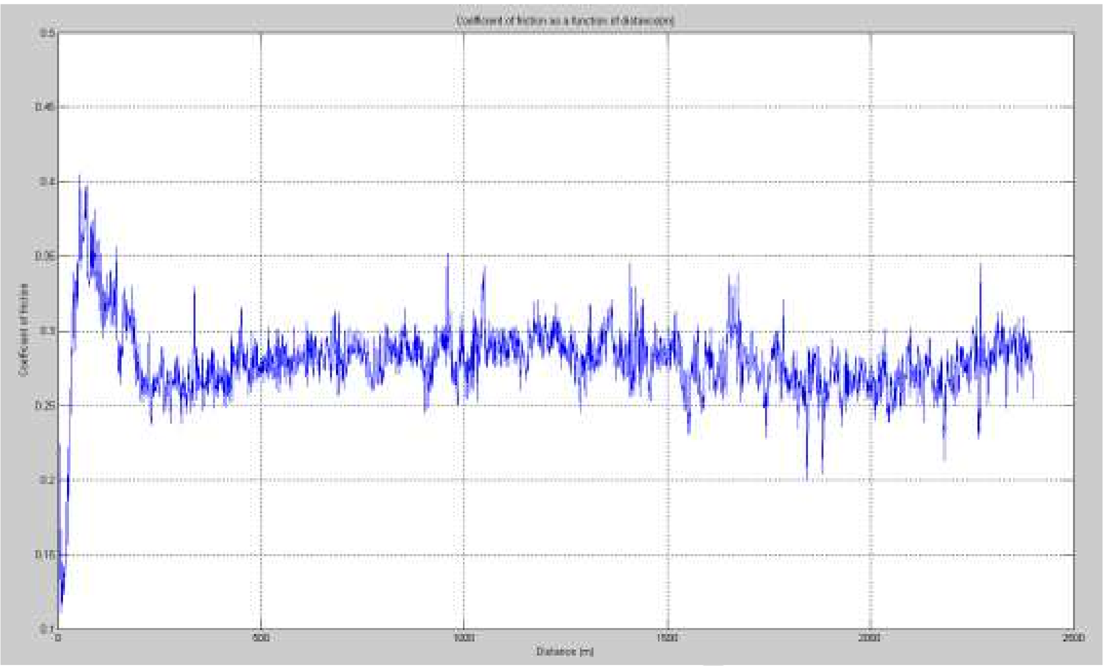
Coefficient of friction as a function of distance(m)
Coefficient of friction
Distance (m)
0.5
0.45
0.4
0.35
0.3
0.25
0.2
0.15
0.1
0
500
1000
1500
2000
2500

(a)

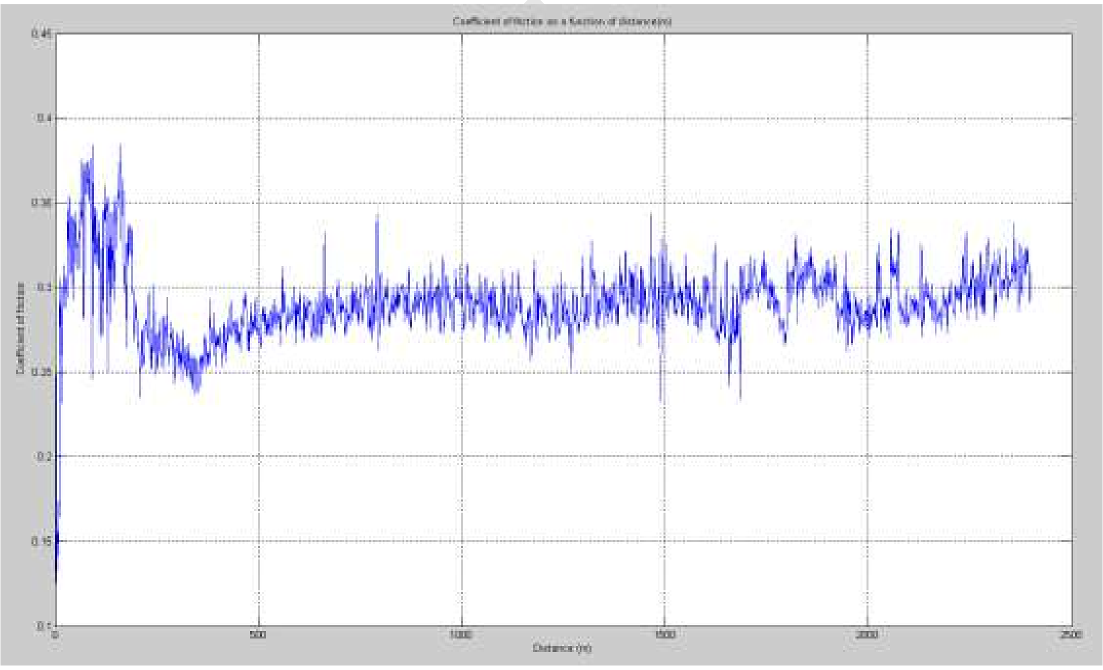
Coefficient of friction as a function of distance(m)
Coefficient of friction
Distance (m)
0.45
0.4
0.35
0.3
0.25
0.2
0.15
0.1
0
500
1000
1500
2000
2500

(b)

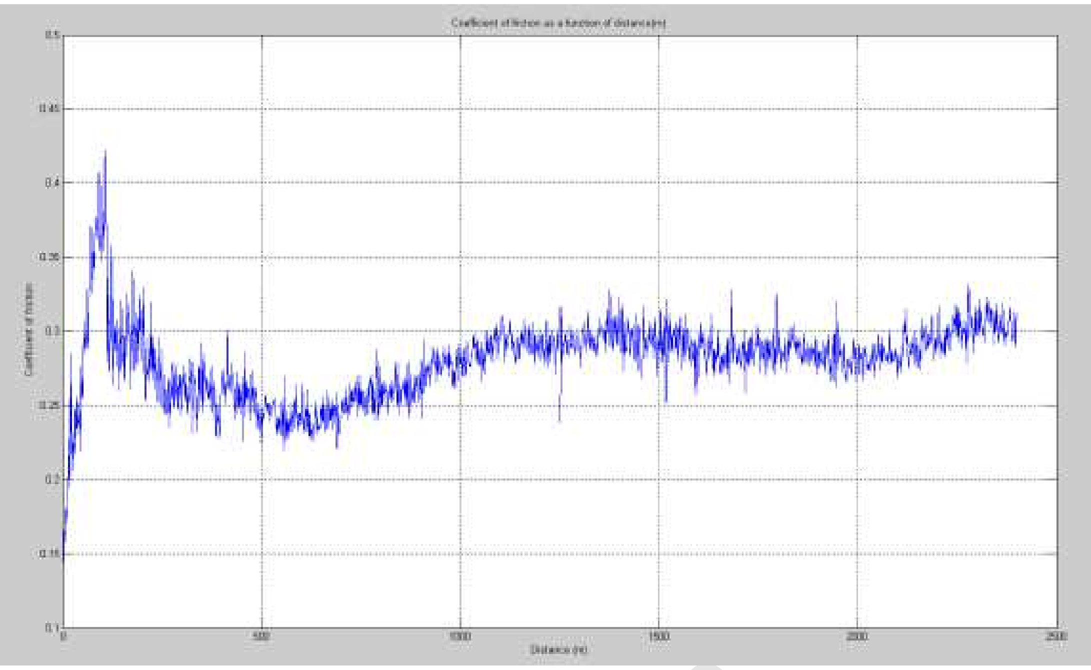

(c)

Figure 87: (a), (b) and (c) are the reciprocating tests performed for 2400m for the 600ºC oxide treated Ti64 samples. The plots show the change in the coefficient of friction as a function of distance.

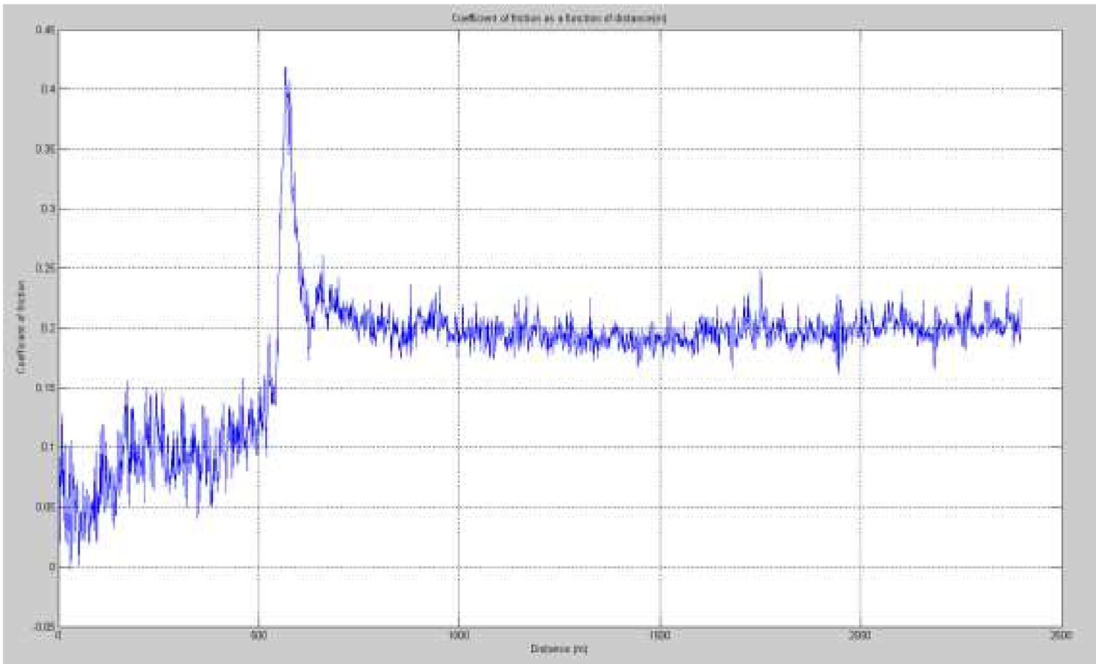
Coefficient of friction as a function of distance(m)
Coefficient of friction
Distance (m)
0.45
0.4
0.35
0.3
0.25
0.2
0.15
0.1
0.05
0
-0.05
0
500
1000
1500
2000
2500

(a)

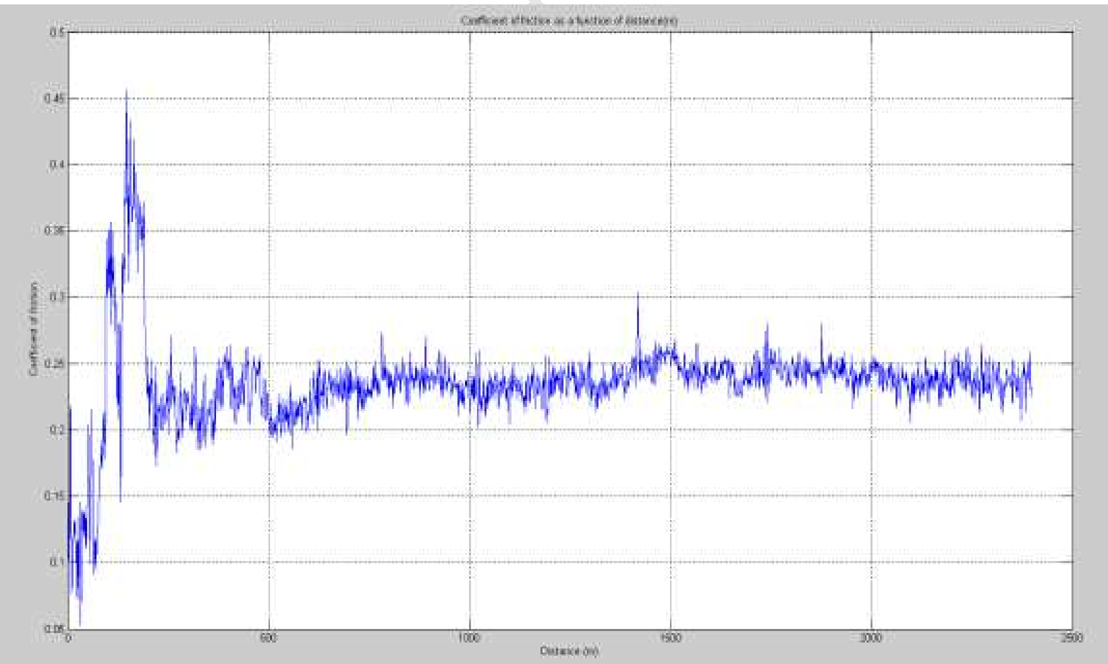
Coefficient of friction as a function of distance(m)
Coefficient of friction
Distance (m)
0.5
0.45
0.4
0.35
0.3
0.25
0.2
0.15
0.1
0.05
0
500
1000
1500
2000
2500

(b)

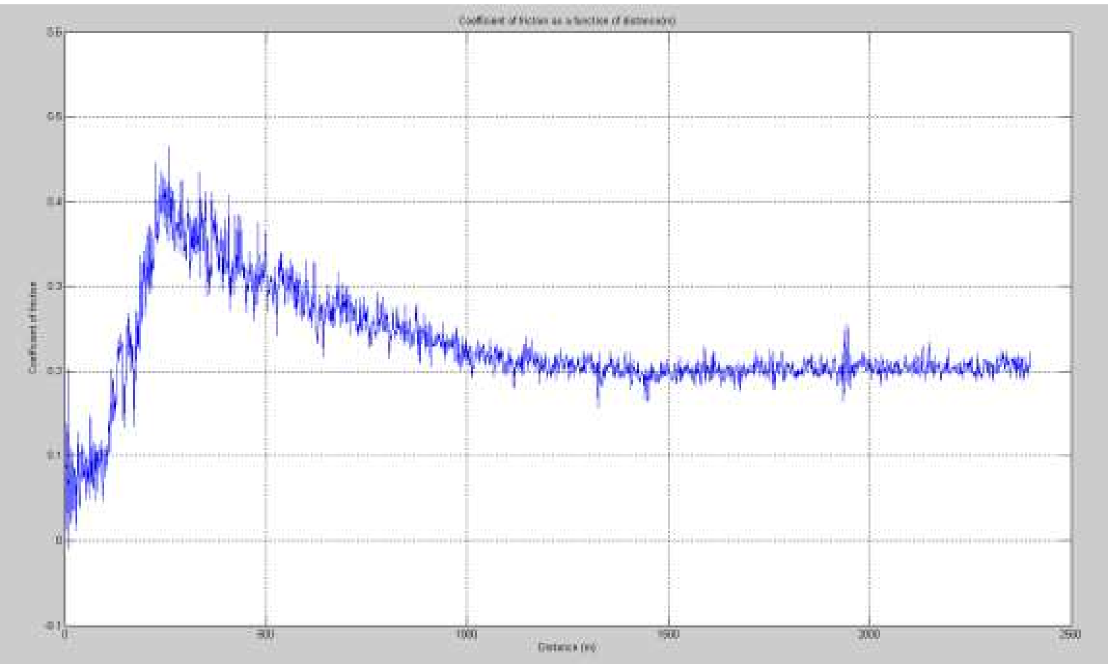

(c)

Figure 88: (a), (b) and (c) are the reciprocating tests performed for 2400m for the 600ºC oxide treated Ti64 samples polished to a metallic finish. The plots show the change in the coefficient of friction as a function of distance.

11 APPENDIX B

11.1 Calibration of the load cell and Hz/Speed conversion for the Renold Crofts drive controller

11.1.1 Calibration of the load cells

Before wear testing could commence on the linear reciprocating rig the load cells had to be calibrated for the voltage to load conversion. Both load cells used were unequipped with their own power source and the small voltage changes produced during strain on the cell were amplified before being used. Horizontal loads were applied to the load cell during calibration to determine the relationship between the amplified voltage output and the actual load experienced by the load cell. These relationships are directly incorporated into the software used during the wear tests namely “UCTFriction.exe”

11.1.2 Hz/Speed conversion for the Renold Crofts drive controller

The Renold crofts drive controller inputs speed in the units of Hz, however it was necessary to convert this speed into m.s^{-1}. To do this the controller was set to a specific speed on the controller and the time it took for the shuttle to traverse the full 100mm track was monitored. This was performed a total of 10 times each for different Hz speeds and the following relationship between Hz and speed (m.s^{-1}) was determined:

$$S = 0.0047(Hz) - 0.007$$

Where:
S = Speed in m.s^{-1},
Hz = The corresponding speed (Hz) inputted into the Renold Crofts Drive Controller.

11.2 Conversion of the raw data produced from the Surtronic 3-P/Computer interface link

11.2.1 Calculation of the sample number to distance ratio for a given cutoff length

When performing profile plots across the wear track it was required to determine what the distance was between successive samples captured that made up the entire profile plot. A cutoff of 0.8mm was used with the Surtronic 3-P, however the actual distance over which samples were captured was experimentally determined as 6.46±0.23mm. This was found by scale measurement of the profile taken by the surtronic on an optical micrograph. Ten profiles were averaged off to provide the assessment length of

6.46±0.23mm for the cutoff of 0.8mm. This value was taken to be constant as the profilometer does not vary the assessment length unless a new cutoff is specified. The amount of data points acquired and saved into an excel spreadsheet is then monitored and recorded, due to varying conditions which affect the acquisition of data from the computer, this number will vary constantly. To calculate the sample number per distance ratio used to plot one axis of the 3-D plots the following relationship is used:

$$SR = \frac{AL}{SC}$$

Where:
SR = Ratio of samples to distance,
AL = Assessment length in mm, experimentally determined to be 6.46±0.23mm for a 0.8mm cutoff,
SC = Samples captured for that given assessment length

The SR value determination is performed before new profile plots for different samples are taken to minimise error introduced by varying computer acquisition speeds. Averages of ten SR values were taken prior to each 3-D plot.

11.2.2 Converting Surtronic-Computer output to µm depth

As discussed earlier the R_{ymax} value taken during a profile is the distance from the largest peak to the deepest valley for that particular surface during that assessment length. The Surtronic 3P-Computer link outputs unknown values which correlate to the depths and heights of the surface topography during profile runs. The following process draws valuable information regarding the distances plotted from that valuable data.
The surtronic 3P is set to retrieve R_{ymax} data and the surtronic-computer link is activated to acquire the relative data. Ten profile readings are taken and the R_{ymax} recorded from the surtronic display as well as the corresponding saved excel spreadsheet for each profile. The saved excel spreadsheet is used to plot a graph showing the actual profile in 2D, this is shown in Figure 89. The reference sample used was that supplied with the profilometer and had a predetermined R_a value of 6.07µm.

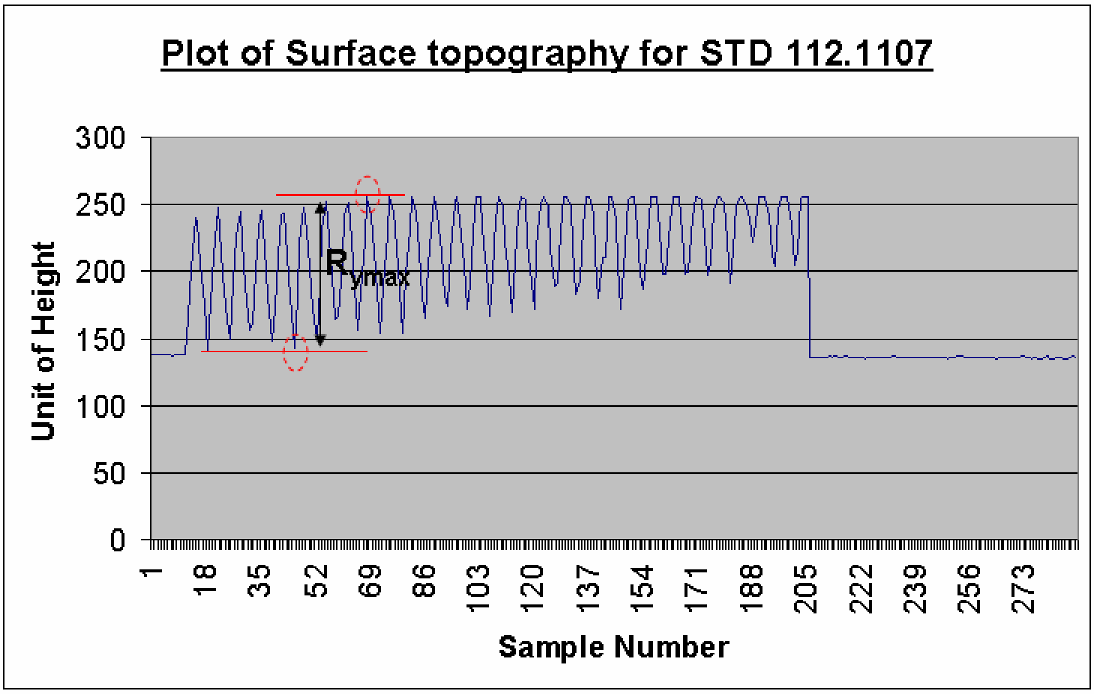

Figure 89: R_{ymax} determined for a given profile from the raw data generated from the Surtronic 3P-Computer link

The above figure shows a plot of the surface used to determine R_{ymax} in terms of the unknown units of height, y-axis. This is repeated ten times to produce an average of R_{ymax} determined from the graphs. The R_{ymax} values taken directly from the profilometer display are also averaged. To determine the relationship between the unknown units for height produced in the spreadsheets to the actual height in µm, the following relationship is used:

$$H = \frac{SD}{UH}$$

Where:

H = Ratio of µm to unknown units i.e. the ratio determined was 0.379µm per 1 excel unit,
SD = R_{ymax} average taken from the Surtronic Display (SD) in µm units,
UH = R_{ymax} average taken from the profile plots in excel in unknown height units.

11.3 Matlab script files compiled

11.3.1 Friction Force (N) vs. Sample No. to μ_s vs. Sliding Distance (m)

The following code was used to convert the raw data of Friction force vs. Sample number to μ_s vs. Distance (m) for a given wear test on the linear reciprocating rig:

```
clc
clear
%Required Data
File=input('Specify the data for analysis. Include the extention,
.xlsx: ','s');
data=xlsread(File);
s=input('Specify sampling rate (Hz) provided in the .csv raw data file:
');
v=input('Specify the speed of the test (m/s): ');
N1=input('Specify the Normal load used (kg): ');
N=9.81*N1;
%Add weight of ball bearing holder setup ie 0.326kg
weight=0.326*9.18;
weight=N+weight;
N=weight;
%Data extraction
y=data(:,2);
x=data(:,1);
d=(x*v)/s;
%Plot of frictional coefficient versus sample number
plot(x,y)
xlabel('Sample number');
ylabel('Frictional Force (N)');
grid on;
set(gca,'Layer','top');
%Need to specify if manual or automatic analyses will be performed
method=input('Specify the type of analysis. If automatic input "auto",
for manual leave blank: ','s');
if method=='auto'
%Request distance parameters for data analyses of the curve
enddist=input('Specify the total distance of the curve: ');
increment=input('Specify the incremental distance where analyses is
performed e.g every 20m: ');
startdist=input('Specify the starting distance where analyses should
begin: ');
totalanaldist=enddist-startdist;%Total distance of analyses
%Check to see if the total distance specified is viable with regards to
the
%incremental distance i.e. quotient must be an integer and not
irrational
datpoints=totalanaldist/increment;
datpoints=ceil(datpoints);%Rounds up to the nearest integer
incrementcheck=totalanaldist/datpoints;
incrementcheck=ceil(incrementcheck);
if incrementcheck==increment %This means that the distance specified is
perfectly divisble by the chosen increment
    disp('Increment will be used.');
```

```
    increment=increment;
else
    disp('The chosen incremental distance is not perfectly divisable by
the total distance.');
    fprintf('The new incremental distance will be set to
%gm.\n',incrementcheck);
    increment=incrementcheck;
end
%Specify cutoff frictional force Trigger limits
disp('Inspect overall graph to provide following data.');
Cutoff1=input('Specify the maximum allowed frictional measurement: ');
Cutoff2=input('Specify the lowest allowed positive frictional force:
');
Cutoff3=input('Specify the maximum negative(highest numerical negative
i.e. -5>-2) allowed frictional measurement: ');
Cutoff4=input('Specify the lowest allowed negative frictional force:
');
for o=startdist:increment:enddist
update=(o+increment-startdist)/increment;%Equation derived from
arithmetic series equation i.e. Tn=a+(n-1)d
%Interval boundaries
low=o-1;
high=o+1;
%Find interval in data set
Intervaldist=find(low<=d & d<=high);%Returns the positions in the "d"
data set that satisfies the find parameters
Intervaldist2=d(Intervaldist);%Data set used in "d" returns the
corresponding "d" values
IntervalFric=y(Intervaldist);%Data set used in "y" returns the
corresponding "y" values
    %CHECK that the interval extracted is correct
    check=[Intervaldist2 IntervalFric];%Shows the distance and
corresponding Force reading for the interval chosen
    subplot(2,1,1)
    plot(d,y)
    xlabel('Distance (m)');
    ylabel('Frictional Force (N)');
    grid on;
    set(gca,'Layer','top');
    subplot(2,1,2)% "2,1,2" => 2 Graphs, 1 Figure, 2 = Position 2
    plot(Intervaldist2,IntervalFric)
    xlabel('Distance (m)');
    ylabel('Frictional Force (N)');
    grid on;
    set(gca,'Layer','top');
%Calculating zero points for the interval to create subintervals
yvec1=IntervalFric(1:end-1);
yvec2=IntervalFric(2:end);
turning=yvec1.*yvec2;
check2=find(IntervalFric==0);%Finds the places where the "y" crosses
the "x" axis, this is interval boundaries
check3=find(turning<0);%Finds the places where the "y" crosses the "x"
axis, this is interval boundaries
lc2=length(check2);
lc3=length(check3);
lc4=lc2+lc3;
```

```
check4=zeros(lc4,1);%Creates check4, a vector of length(lc2 and lc3) made of zeros
check4(1:lc2)=check2;
check4(lc2+1:end)=check3;%These two lines puts the values of check2 and check3 into check4
check4=sort(check4);%Sorts check4 data in ascending order
%Now the intervals of interest are found and need to be analysed.
for j=2:length(check4)
    is=check4(j-1);%interval start
    ie=check4(j);%interval end
    high(j)=max(IntervalFric(is:ie));
    low(j)=min(IntervalFric(is:ie));
end
%Take out values that are not consistent with cutoff trigger limits
highend=high(high<Cutoff1 & high>Cutoff2);
lowend=low(low>Cutoff3 & low<Cutoff4);
%Getting average of highend
l1=length(highend);
sum=0;
for i=1:l1
    sum=sum+highend(i);
end
avghigh=sum/l1;
%Getting average of lowend
l2=length(lowend);
sum2=0;
for i=1:l2
    sum2=sum2+lowend(i);
end
avglow=sum2/l2;
Fric=avghigh+abs(avglow);
Fric=Fric/2;
FricCoeff(update)=(Fric-1.86)/N;
end
Distance=startdist:increment:enddist;
Distance=Distance.';
plot(Distance,FricCoeff)
xlabel('Distance (m)');
ylabel('Frictional Coeffiecient');
grid on;
set(gca,'Layer','top');
else
%Need to specify if an entire curve needs to be analysed or just a section
disp('Following is the input for either a full data set analyses or a precise distance measurement analyses.');
ques=input('Would you like to analyse the entire curve, please respond with a "y" for yes or "n" for no: ','s');
if ques=='y'
%Request distance parameters for data analyses of the curve
enddist=input('Specify the total distance of the curve: ');
increment=input('Specify the incremental distance where analyses is performed e.g every 20m: ');
startdist=input('Specify the starting distance where analyses should begin: ');
totalanaldist=enddist-startdist;%Total distance of analyses
```

```
%Check to see if the total distance specified is viable with regards to
the
%incremental distance i.e. quotient must be an integer and not
irrational
datpoints=totalanaldist/increment;
datpoints=ceil(datpoints);%Rounds up to the nearest integer
incrementcheck=totalanaldist/datpoints;
incrementcheck=ceil(incrementcheck);
if incrementcheck==increment %This means that the distance specified is
perfectly divisble by the chosen increment
    disp('Increment will be used.');
    increment=increment;
else
    disp('The chosen incremental distance is not perfectly divisable by
the total distance.');
    fprintf('The new incremental distance will be set to
%gm.\n',incrementcheck);
    increment=incrementcheck;
end
for o=startdist:increment:enddist
update=(o+increment-startdist)/increment;%Equation derived from
arithmetic series equation i.e. Tn=a+(n-1)d
%Interval boundaries
low=o-1;
high=o+1;
%Find interval in data set
Intervaldist=find(low<=d & d<=high);%Returns the positions in the "d"
data set that satisfies the find parameters
Intervaldist2=d(Intervaldist);%Data set used in "d" returns the
corresponding "d" values
IntervalFric=y(Intervaldist);%Data set used in "y" returns the
corresponding "y" values
    %CHECK that the interval extracted is correct
    check=[Intervaldist2 IntervalFric];%Shows the distance and
corresponding Force reading for the interval chosen
    subplot(2,1,1)
    plot(d,y)
    xlabel('Distance (m)');
    ylabel('Frictional Force (N)');
    grid on;
    set(gca,'Layer','top');
    subplot(2,1,2)% "2,1,2" => 2 Graphs, 1 Figure, 2 = Position 2
    plot(Intervaldist2,IntervalFric)
    xlabel('Distance (m)');
    ylabel('Frictional Force (N)');
    grid on;
    set(gca,'Layer','top');
%Specify cutoff frictional force regions
fprintf('This section deals with trigger limits for the distance
%gm.\n',o);
disp('Inspect peaks to complete the following');
Cutoff1=input('Specify the max Frictional force as a trigger limit: ');
Cutoff2=input('Specify the min Frictional force as a trigger limit: ');
disp('Inspect troughs to complete the following.');
Cutoff3=input('Specify the max(highest negative) Frictional force as a
trigger limit: ');
```

```
Cutoff4=input('Specify the min(lowest negative) Frictional force as a
trigger limit: ');
fprintf('Trigger limits completed for the distance %gm.\n',o);
%Calculating zero points for the interval to create subintervals
yvec1=IntervalFric(1:end-1);
yvec2=IntervalFric(2:end);
turning=yvec1.*yvec2;
check2=find(IntervalFric==0);%Finds the places where the "y" crosses
the "x" axis, this is interval boundaries
check3=find(turning<0);%Finds the places where the "y" crosses the "x"
axis, this is interval boundaries
lc2=length(check2);
lc3=length(check3);
lc4=lc2+lc3;
check4=zeros(lc4,1);%Creates check4, a vector of length(lc2 and lc3)
made of zeros
check4(1:lc2)=check2;
check4(lc2+1:end)=check3;%These two lines puts the values of check2 and
check3 into check4
check4=sort(check4);%Sorts check4 data in ascending order
%Now the intervals of interest are found and need to be analysed.
for j=2:length(check4)
    is=check4(j-1);%interval start
    ie=check4(j);%interval end
    high(j)=max(IntervalFric(is:ie));
    low(j)=min(IntervalFric(is:ie));
end
%Take out values that are not consistent with cutoff trigger limits
highend=high(high<Cutoff1 & high>Cutoff2);
lowend=low(low>Cutoff3 & low<Cutoff4);
%Getting average of highend
l1=length(highend);
sum=0;
for i=1:l1
    sum=sum+highend(i);
end
avghigh=sum/l1;
%Getting average of lowend
l2=length(lowend);
sum2=0;
for i=1:l2
    sum2=sum2+lowend(i);
end
avglow=sum2/l2;
Fric=avghigh+abs(avglow);
Fric=Fric/2;
FricCoeff(update)=(Fric-1.86)/N;
end
Distance=4:20:580;
Diatance=Distance.';
plot(Distance,FricCoeff)
xlabel('Distance (m)');
ylabel('Frictional Coeffiecient');
grid on;
set(gca,'Layer','top');
else
point=input('Specify the distance(m) that is to be analysed: ');
```

```
%Interval boundaries
low=point-1;
high=point+1;
%Find interval in data set
Intervaldist=find(low<=d & d<=high);%Returns the positions in the "d"
data set that satisfies the find parameters
Intervaldist2=d(Intervaldist);%Data set used in "d" returns the
corresponding "d" values
IntervalFric=y(Intervaldist);%Data set used in "y" returns the
corresponding "y" values
    %CHECK that the interval extracted is correct
    check=[Intervaldist2 IntervalFric];%Shows the distance and
corresponding Force reading for the interval chosen
    subplot(2,1,1)
    plot(d,y)
    xlabel('Distance (m)');
    ylabel('Frictional Force (N)');
    grid on;
    set(gca,'Layer','top');
    subplot(2,1,2)% "2,1,2" => 2 Graphs, 1 Figure, 2 = Position 2
    plot(Intervaldist2,IntervalFric)
    xlabel('Distance (m)');
    ylabel('Frictional Force (N)');
    grid on;
    set(gca,'Layer','top');
%Specify cutoff frictional force regions
fprintf('This section deals with trigger limits for the distance
%gm.\n',point);
disp('Inspect peaks to complete the following.');
Cutoff1=input('Specify the max Frictional force as a trigger limit: ');
Cutoff2=input('Specify the min Frictional force as a trigger limit: ');
disp('Inspect troughs to complete the following.');
Cutoff3=input('Specify the max(highest negative) Frictional force as a
trigger limit: ');
Cutoff4=input('Specify the min(lowest negative) Frictional force as a
trigger limit: ');
fprintf('Trigger limits completed for the distance %gm.\n',point);
%Calculating zero points for the interval to create subintervals
yvec1=IntervalFric(1:end-1);
yvec2=IntervalFric(2:end);
turning=yvec1.*yvec2;
check2=find(IntervalFric==0);%Finds the places where the "y" crosses
the "x" axis, this is interval boundaries
check3=find(turning<0);%Finds the places where the "y" crosses the "x"
axis, this is interval boundaries
lc2=length(check2);
lc3=length(check3);
lc4=lc2+lc3;
check4=zeros(lc4,1);%Creates check4, a vector of length(lc2 and lc3)
made of zeros
check4(1:lc2)=check2;
check4(lc2+1:end)=check3;%These two lines puts the values of check2 and
check3 into check4
check4=sort(check4);%Sorts check4 data in ascending order
%Now the intervals of interest are found and need to be analysed.
for j=2:length(check4)
    is=check4(j-1);%interval start
```

```
    ie=check4(j);%interval end
    high(j)=max(IntervalFric(is:ie));
    low(j)=min(IntervalFric(is:ie));
end
%Take out values that are not consistent with cutoff trigger limits
highend=high(high<Cutoff1 & high>Cutoff2);
lowend=low(low>Cutoff3 & low<Cutoff4);
%Getting average of highend
l1=length(highend);
sum=0;
for i=1:l1
    sum=sum+highend(i);
end
avghigh=sum/l1;
%Getting average of lowend
l2=length(lowend);
sum2=0;
for i=1:l2
    sum2=sum2+lowend(i);
end
avglow=sum2/l2;
Fric=avghigh+abs(avglow);
Fric=Fric/2;
FricCoeff=(Fric-1.86)/N
end
end
```

11.3.2 Determination of the wear track width using profilometer raw data

The following code was compiled to generate a 2D plot of the profile across a given wear track, to determine the actual wear track width (mm) and relative height of the wear track (µm):

```
%Analysed tests need to be in .xlsx format and have the sample number
in
%coloumn 1 and profilometer readings in coloumn 2
clear;
clc;
check=input('Specify the file to check track width: ','s');
check2=xlsread(check);
xvalues=check2(:,1);
zvalues=check2(:,2);
plot(xvalues, zvalues);
xlabel('Sample number');
ylabel('Profile point');
title('Raw data profile plot.');
grid on;
linezero=input('Enter the zero line value ie. normally about 140: ');
SamplRate=input('Enter the distance(mm) between samples ie.0.8mm
cutoff=0.0312mm: ');
heights=zvalues-linezero;
heights=heights.*0.379;
distance=xvalues.*SamplRate;
```

```
plot(distance, heights);
xlabel('Distance (mm)');
ylabel('Height (um)');
title('Converted Data ie Heights vs distance.');
grid on;
combine=[distance heights];
xlswrite('1.xlsx',combine) %Change file name after export
clear
clc
```

11.3.3 Program to average off the coefficient of friction output for the Pin on disk tribometer

To reduce the level of fluctuation seen in the raw data for the pin on disk tribometer the following code was constructed to average off a predetermined number of points:

```
disp('Note that when using the program the excel spreadsheet to be
analysed must be in the same folder. ');
data=input('Specify the excel spreadsheet, include extension (e.g
.xls): ','s');
div=input('Specify the number whereby averages should be taken eg.
every 5,10 or 100 points: ');
dis=input('Specify the distance of the test (m): ');
y=xlsread(data);
f=length(y);
fprintf('There are %g data points in your excel file. This value is
your data point max.  \n',f);
limit=input('Specify the closest number below the data point max that
is divisible by your average set: ');
newy=y(1:limit);
g=length(newy);
inc=g/div;
for i=1:inc
    k=1+((i-1)*div);
    yavg(i)=(sum(newy(k:k+div-1)))/div;
end
yavg2=yavg.';
displot=dis/inc;
newdis=0:displot:dis;
newdis2=newdis';
if length(newdis2)>length(yavg2)
    sub=length(newdis2)-length(yavg2);
    newdis3=newdis2(1:end-sub);
    combine=[newdis3 yavg2];
    xlswrite('output_average.xls',combine);
elseif length(yavg2)>length(newdis2)
    sub=length(yavg2)-length(newdis2);
    yavg3=yavg2(1:end-sub);
    combine=[newdis2 yavg3];
    xlswrite('output_average.xls',combine);
else
    combine=[newdis2 yavg2];
    xlswrite('output_average.xls',combine);
end
```